POLITECNICO DI TORINO

Master of Science
in Automotive Engineering

Master's Thesis

Development of a 3D-CFD Model for the Analysis of Combustion and Emissions in a Light-Duty Diesel Engine

Supervisors
Prof. Ezio Spessa
Prof. Mirko Baratta
Prof. Roberto Finesso

Candidate
Gvidas Šamelis

October 2019

Acknowledgments

The author wishes to thank professors Ezio Spessa, Mirko Baratta, Roberto Finesso, and Daniela Anna Misul of the Energy Department of Politecnico di Torino for the possibility to work on the present thesis, support, and valuable advices. The author is especially indebted to his colleagues at Politecnico di Torino Engine Research Centre (PT-ERC), PhD student Prashant Goel and research assistant Silvestru Chiriches, for supervision, discussions, and humorous moments during the period of 6 months when this thesis was done. Lastly, but most importantly, the author thanks his family, mom Jūratė, dad Ričardas, and Viktorija, for their continuing support in all endeavors the author makes, and decisions he takes.

Abstract

In order to reduce emissions of carbon dioxide from engines, a shift to carbon-neutral fuels is one of the promising alternatives. Hydrotreated vegetable oils (HVOs) are very high-quality bio-based diesel fuels, which do not have negative effects on engines, exhaust aftertreatment devices, or exhaust emissions. A research activity has been started at the Energy Department of Politecnico di Torino to investigate effects of using HVO instead of a conventional diesel fuel in a production engine. As a first step, a light duty commercial compression-ignition engine fueled with the conventional diesel fuel has been tested. In the present thesis, as the next step of the activity, a validation and sensitivity analysis of 3D-CFD (three-dimensional computational fluid dynamics) model is presented. It enables the assessment of the impact of mesh size, swirl number, and turbulent Schmidt number variations on simulated diesel combustion and pollutant emissions. The 3D-CFD analysis is carried out using the CONVERGE CFD software on a 45-degree sector of the symmetrical combustion chamber from IVC (intake valve closing) to EVO (exhaust valve opening). Engine performance is simulated at 2000 rev/min and two different loads: full load (18 bar BMEP) and part load (9 bar BMEP). The model is validated against the experimental data in terms of in-cylinder pressure, heat release rate, NOx and soot emissions. The same parameters are used to quantify the influence of the mesh size on the accuracy of numerical results, taking into account the computational cost involved when improving mesh refinement. As the initial flow field within the cylinder at IVC in this work is defined using data available from experiments and GT-POWER 1D simulations, the sensitivity of diesel combustion simulations on the initial swirl number is investigated. Also, additional sensitivity analysis is performed by changing the turbulent Schmidt number, which is an important parameter influencing the transport of species during 3D-CFD simulation. Results of the sensitivity analysis yield useful indications on definition of initial conditions for 3D-CFD simulations, as well as on further model calibration possibilities. In the first part of this thesis, a theoretical background on flow and combustion in diesel engines, CFD fundamentals, and the CONVERGE CFD software is provided. The second part deals with preparation and calibration of the CFD model. Finally, in the third part, results of the sensitivity analysis are provided and explained. In the future, the following step of the research activity will include using HVO instead of the conventional diesel in the CFD model developed during the present thesis. The aim will be to investigate the influence of HVO on the combustion process and formation of pollutants.

Contents

List of Figures

List of Tables

1 Introduction

Growing attention for the ecology and the climate change imposes a burden on the automotive society to reach for ever greener and more efficient vehicles, especially as far as powertrains are concerned. Many alternatives have been considered and tried, however conventional spark-ignition and compression-ignition internal combustion engines still remain the main choice when the maturity of technology, existing infrastructure, and some inborn technical advantages are taken into account. Thus, a lot of attention is dedicated to develop these engines further.

One of the possible methods for tackling the carbon dioxide emissions problem is to fuel conventional IC engines with carbon-neutral fuels, such as biofuel. Hydrotreating of vegetable oils or animal fats is an alternative process to esterification for producing bio-based diesel fuels. Hydrotreated products are also called renewable diesel fuels [1].

Hydrotreated vegetable oils (HVOs) do not have the detrimental effects of ester-type biodiesel fuels, like increased NOx emission, deposit formation, storage stability problems, more rapid aging of engine oil or poor cold properties. They are free of aromatics, oxygen and sulfur and have high cetane numbers [1]. As a result, HVO seem like a good alternative for normal diesel fuel without compromising fuel logistics, engines, exhaust aftertreatment devices, or exhaust emissions.

A research activity has been started at the Energy Department of Politecnico di Torino to investigate effects of using HVO instead of a conventional diesel fuel in a production engine. Both experimental tests and numerical analysis (using computational fluid dynamics, CFD) have been planned to be done in order to obtain a comprehesive understanding of the combustion process, how it is impacted by different fuels, especially considering the production of pollutants.

As a first step, a light duty commercial compression-ignition engine fueled with the conventional diesel fuel has been tested. In the present thesis, as the next step of the activity, development, validation, and sensitivity analysis of 3D-CFD model is presented. The analysis is carried out using the CONVERGE CFD software on a 45-degree sector of the symmetrical combustion chamber from IVC (intake valve closing) to EVO (exhaust valve opening). Engine performance is simulated at two different operating points, and validated against the experimental data in terms of in-cylinder pressure, heat release rate, NOx and soot emissions.

The sensitivity analysis enables the assessment of the impact of mesh size, swirl ratio, and turbulent Schmidt number on simulated diesel combustion and pollutant emissions. Collected knowledge is thought to be useful not only for better understanding of the CFD analysis and diesel combustion process, but also for the future work regarding application of HVO on the same engine.

The thesis is arranged in three major parts. The first (Chapters 2 to 4) provides an introduction to the charge flow and combustion process in compression-ignition engines, including diesel spray fundamentals and thorough discussion on pollutant formation. Chapter 3 then focuses on the fundamentals of CFD in general, and Chapter 4 gives an overview of the CONVERGE CFD software and various models available as part of this tool. The second part (Chapter 5) analyzes the experimental data provided by the testing activity of a given diesel engine, and deals with development and validation of the CFD model. Finally, the third part (Chapter 6) focuses on results of the sensitivity analysis. Section 6.1 presents discussion on the impact of the mesh size on computation, simulated injection and combustion processes, and predicted pollutant emissions. Then, Section 6.2 and Section 6.3 provide results of sensitivity analyses of swirl ratio and Schmidt number, respectively.

2 Flow and Combustion in Compression-Ignition Engines

Conventional compression-ignition engines, fueled by diesel, are commonly used in automotive field. Advantages of diesel engines include usually higher fuel conversion efficiency (in part due to high compression ratios which range from 12 to 24 [2]) and higher volumetric efficiency, as no throttle is necessary for load control. Instead, the load control is achieved by varying the amount of fuel injected each cycle.

Diesel is injected as a high pressure liquid spray into the compressed air, immediately before the desiderated start of combustion. This is necessary, as fuels such as diesel are characterized by high reactivity, thus cannot be premixed with air and compressed inside the cylinder: the combustion process would start spontaneously during the compression stroke.

As a result, it is important to control the charge motion within the cylinder and the injection process to achieve a sufficiently quick atomization, vaporization, and mixing with air of the injected liquid. This way it is possible to achieve targets in terms of fuel consumption and pollutant emissions, most important of whom for diesel engines are nitric oxides (NOx) and soot.

2.1 Charge Motion within the Cylinder

Gas motion within the engine cylinder is one of the major factors that controls the air-fuel mixing and combustion processes in diesel engines. It also has a significant impact on heat transfer. Both the bulk gas motion and the turbulence characteristics of the flow are important [2].

The flow into the cylinder through the inlet valves (forming a jet) does two things: first, the geometrical configuration of the inlet ports and the valves, and their opening schedule create organized motions in the cylinder, known as swirl (about the cylinder axis) and tumble (orthogonal to the cylinder axis); second, the jet itself is turbulent, and much of the directed (non-turbulent) energy in the jet is converted to turbulence, resulting in a very high turbulence level during the inlet stroke. During the second half of the inlet stroke much of this turbulence decays, both because the jet is coming to an end, and due to the effects of viscosity. During the compression stroke, the increase of density and the changes in length scales have the effect of amplifying the turbulence which remained from the inlet jet, although the viscous decay continues [3].

Near the top dead center (TDC), some of the organized motions break up into turbulence, increasing the turbulence level. During combustion the turbulence level rises. Then, during the power stroke, geometrical changes result in a strong attenuation of the turbulence and any organized motion that has survived. This, combined with the viscous decay, results in the turbulence being sharply suppressed. Little turbulence is generated during the exhaust stroke [3].

2.1.1 Organized Motions in the Cylinder

Swirl

Swirl is defined as organized rotation of the charge about the cylinder axis, as shown in Figure 2-1. Swirl is created by bringing the intake flow into the cylinder with an initial angular momentum. While some decay in swirl due to friction occurs during the engine cycle, intake generated swirl usually persists through the compression, combustion, and expansion processes. In diesel engine designs with bowl-in-piston combustion chambers, the rotational motion set up during intake is substantially modified during compression. Swirl is used in diesels to promote more rapid mixing between the inducted air charge and the injected fuel [2].

Tumble

Tumble is defined as organized rotation of the charge orthogonal to the cylinder axis, as shown in Figure 2-1. Tumble is induced by the inlet poppet valve, and always breaks down to turbulence as the piston approaches TDC. There is no room between the piston crown and the cylinder head for a big vortex; only motions with scales of the order of the clearance height can survive, so the vortex (tumble) breaks up into turbulence of smaller scale [3]. Tumble, together with swirl, is one of the principal means to ensure rapid mixing between fuel and air in diesel engines.

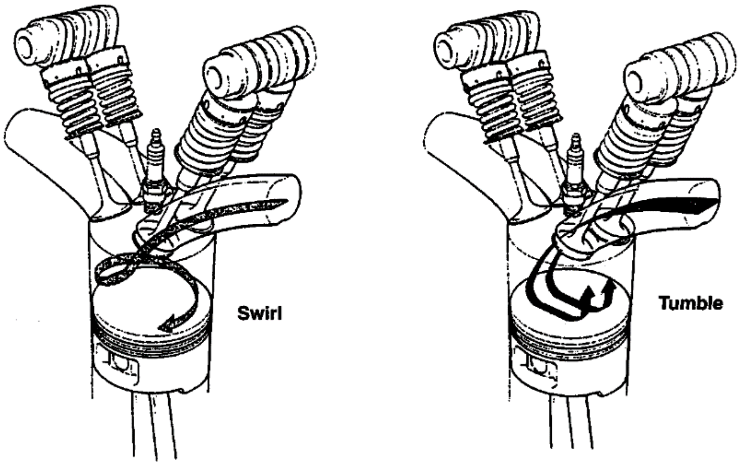

Figure 2-1 Schematic of swirl and tumble motions [4]

Squish

Squish is the name given to the radially inward or transverse gas motion that occurs toward the end of the compression stroke when a portion of the piston face and cylinder head approach each other closely. Figure 2-2 shows how gas is displaced into the bowl-in-piston diesel combustion chamber [2].

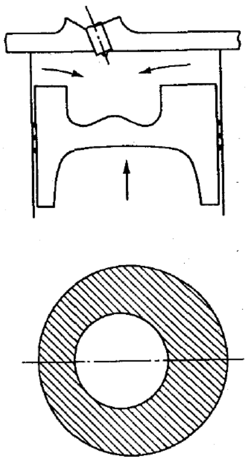

Figure 2-2 Schematic of how piston motion generates squish [2]

Squish-generated gas motion results from using a compact combustion chamber geometry. Squish can intensify swirl toward TDC, which helps mixing between the inducted air charge and the injected fuel. Also, as the piston approaches TDC, the charge trapped between the piston crown and the squish area is forced out in a turbulent jet into the center of the cylinder [3].

2.1.2 In-Cylinder Turbulence

The flow processes in the engine cylinder are turbulent. In turbulent flows, the rates of transfer and mixing are several times greater than the rates due to molecular diffusion. This turbulent “diffusion” results from the local fluctuations in the flow field. It leads to increased rates of momentum, heat and mass transfer, and is essential to the satisfactory operation of spark-ignition and diesel engines [2].

Turbulent flows are always dissipative. Viscous shear stresses perform deformation work on the fluid which increases its internal energy at the expense of its turbulence kinetic energy (TKE). Thus, energy is required to generate turbulence: if no energy is supplied, turbulence decays (a common source of energy for turbulent velocity fluctuations is shear in the mean flow). Turbulence is rotational and characterized by high fluctuating vorticity. In the engine cylinder, the flow is unsteady and may exhibit substantial cycle-to-cycle fluctuations. Both large-scale and small-scale turbulent motions are important factors governing the overall behavior of the flow [2].

An important characteristic of a turbulent flow is its irregularity or randomness. Statistical methods are therefore used to define such a flow field. The quantities normally used are: the mean velocity, the fluctuating velocity about the mean, and several length and time scales.

In engines, the flow pattern changes during the engine cycle, so it is not a steady turbulent flow situation. Also, while the overall features of the flow repeat each cycle, the details do not because the mean flow can vary significantly from one engine cycle to the next. There are both cycle-to-cycle variations in the mean or bulk flow at any point in the cycle, as well as turbulent fluctuations about that specific cycle's mean flow [2]. Approaches used in quasi-periodic flows, such as that which occurs in the engine cylinder, are ensemble-averaging and cycle-resolved-averaging. These approaches are not discussed in this thesis; detailed descriptions of ensemble-averaging and cycle-resolved-averaging can be found in [2] and [5], respectively.

In turbulent flows, a number of length scales exist that characterize different aspects of the flow behavior. The largest eddies in the flow are limited in size by the system boundaries, while the smallest scales of the turbulent motion are limited by molecular diffusion [2]. Also, an important characteristic is turbulence kinetic energy, which is defined as the mean kinetic energy per unit mass associated with eddies in turbulent flow. Turbulence kinetic energy is proportional to u'^2 (the square of turbulence intensity).

2.2 Diesel Spray Fundamentals

The fuel is introduced into the cylinder of a diesel engine through a nozzle with a large pressure difference across the nozzle orifice. The large pressure difference is required for the fuel entering the combustion chamber to achieve a sufficiently high velocity to atomize into small droplets (to enable rapid evaporation) and to travel across the combustion chamber in available time (to fully utilize the air charge within the cylinder).

Figure 2-3 illustrates the structure of a typical direct-injection (DI) diesel engine fuel spray. Also, it shows the lower part of an injection nozzle with needle, sac hole, and injection hole.

Modern injectors have hole diameters of about 180 μm and less, while the length of these holes is about 1 mm. The liquid enters the combustion chamber with velocities of 500 m/s and more [6].

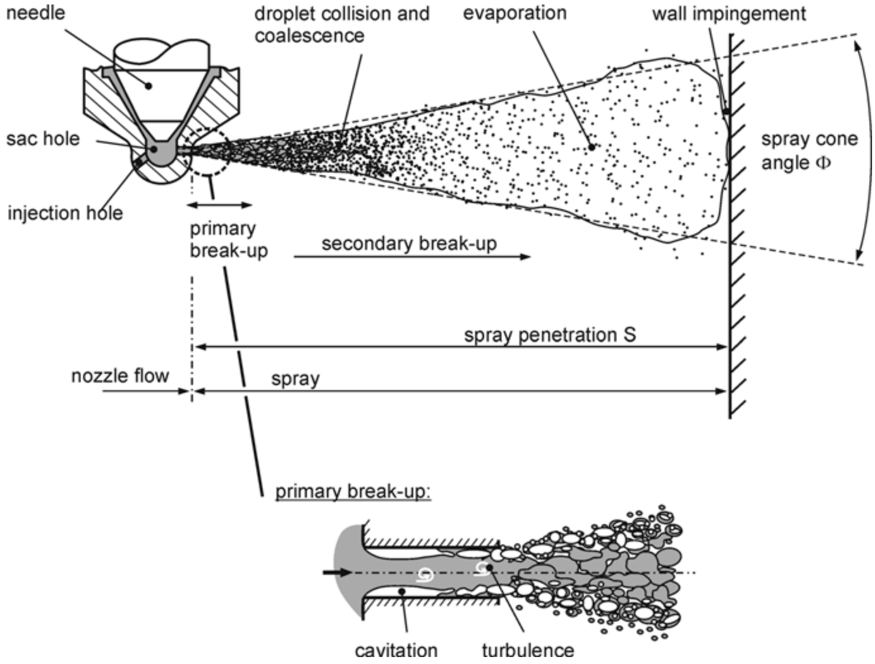

Figure 2-3 Schematic of diesel fuel spray defining its major parameters [6]

Immediately after leaving the nozzle hole, the jet starts to break up into a conical spray. This first break-up of the liquid is called primary break-up and results in large ligaments and droplets that form the dense spray near the nozzle. In case of high-pressure injection, cavitation and turbulence, which are generated inside the injection holes, are the main break-up mechanisms. The subsequent break-up processes of already existing droplets into smaller ones are called secondary break-up and are due to aerodynamic forces (caused by the relative velocity between droplets and surrounding gas), which decelerate the droplets. The drops at the spray tip experience the strongest drag force and are much more decelerated than droplets that follow in their wake. Thus, the droplets at the spray tip are continuously replaced by new ones, and the spray penetration increases. The droplets with low kinetic energy are pushed aside and form the outer spray region [6].

A conical full-cone spray is formed that is more and more diluted downstream the nozzle by the entrainment of air. Most of the liquid mass is concentrated near the spray axis, while the outer spray regions contain less liquid mass and more fuel vapor. Droplet velocities are maximal at the spray axis and decrease in the radial direction due to interaction with the entrained gas. In the dense spray, the probability of droplet collisions is high. These collisions can result in a change of droplet velocity and size. Droplets can break up into smaller ones, but they can also combine to form larger drops, which is called droplet coalescence [6].

In the dilute spray further downstream the main factors of influence on further spray disintegration and evaporation are the boundary conditions imposed by the combustion chamber such as gas temperature and density as well as gas flow (tumble, swirl). The penetration length is limited by the distance between the nozzle and the piston bowl. In the case of high injection pressure and long injection duration (full load) or low gas densities (early injection) the spray may impinge on the wall, and the formation of a liquid wall film is possible [6].

The extent to which the fuel spray penetrates across the combustion chamber has an important influence on air utilization and air-fuel mixing rates. In multi-spray DI diesel combustion systems, overpenetration gives impingement of liquid fuel on cool surfaces which, especially with little or no air swirl, lowers mixing rates and increases emissions of unburned and partially burned species. Yet underpenetration results in poor air utilization since the air on the periphery of the chamber does not then contact the fuel [2].

Finally, to understand the impact of the injected diesel spray behavior on the combustion process it is necessary to take a deeper look at processes that influence the air-fuel mixing, and so the time required to achieve the point of autoignition. These processes are atomization and evaporation.

2.2.1 Atomization

The atomization process is one in which bulk liquid is converted into small drops. Basically, it can be considered as a disruption of the consolidating influence of surface tension by the action of internal and external forces. In the absence of such disruptive forces, surface tension tends to pull the liquid into the form of a sphere, since this has the minimum surface energy. Liquid viscosity exerts a stabilizing influence by opposing any change in system geometry. On the other hand, aerodynamic forces acting on the liquid surface may promote the disruption process by applying an external distorting force to the bulk liquid. Breakup occurs when the magnitude of the disruptive force just exceeds the consolidating surface tension force. Many of the larger drops produced in the initial disintegration process are unstable and undergo further disruption into smaller drops. Thus, the final range of drop sizes produced in a spray depends not only on the drop sizes produced in primary atomization (primary break-up), but also on the extent to which these drops are further disintegrated during secondary atomization (secondary break-up) [7].

The mode of drop disintegration depends on whether the drop is subjected to steady acceleration or is suddenly exposed to a high velocity gas stream. With steady acceleration the drop becomes increasingly flattened, and at a critical relative velocity it is blown out into the form of a hollow bag attached to a roughly circular rim, as shown in Figure 2-4. On disintegration the bag produces a shower of very fine drops, while the rim, which contains at least 70 % of the mass of the original drop, breaks up into larger drops [7].

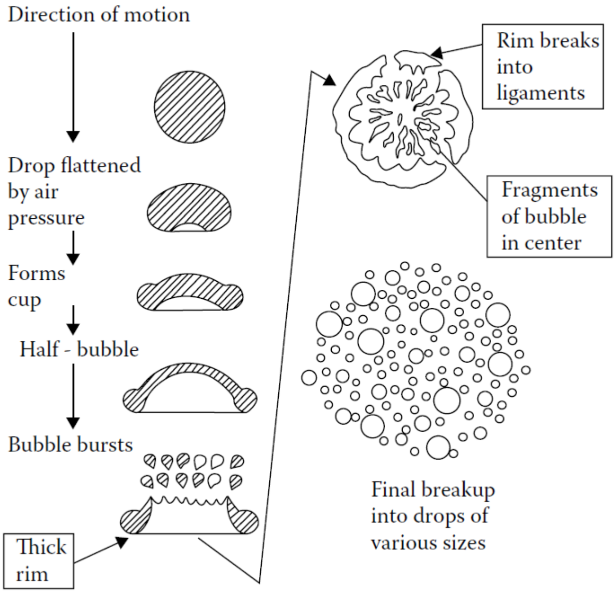

Figure 2-4 Breakup of a spherical drop by interaction with ambient air [7]

Under diesel engine injection conditions, the fuel jet forms a cone-shaped spray at the nozzle exit, as previously explained. This type of behavior is classified as the atomization breakup regime, and it produces droplets with sizes very much less than the nozzle exit diameter.

At low jet velocity, in the Rayleigh regime, breakup is due to the unstable growth of surface waves caused by surface tension and results in drops larger than the jet diameter. As jet velocity is increased, forces due to the relative motion of the jet and the surrounding air augment the surface tension force, lead to drop sizes of the order of the jet diameter. This is called the first wind-induced breakup regime. A further increase in jet velocity results in breakup characterized by divergence of the jet spray after an intact or undisturbed length downstream of the nozzle. In this second wind-induced breakup regime, unstable growth of short-wavelength waves induced by the relative motion between the liquid and surrounding air produces droplets whose average size is much less than the jet diameter. Further increases in jet velocity lead to breakup in the atomization regime, where the breakup of the outer surface of the jet occurs at, or before, the nozzle exit plane and results in droplets whose average diameter is much smaller than the nozzle diameter. Aerodynamic interactions at the liquid/gas interface appear to be one major component of the atomization mechanism in this regime [2].

During the injection period, the injection conditions such as injection pressure, nozzle orifice area, and injection rate may vary. Consequently, the droplet size distribution at a given location in the spray may also change with time during the injection period. In addition, since the details of the atomization process are different in the spray core and at the spray edge, and the trajectories of individual drops depend on their size, initial velocity, and location within the spray, the drop size distribution will vary with position within the spray. To characterize the spray, expressions for drop size distribution and mean diameter are desirable. An appropriate and commonly used mean diameter is the Sauter mean diameter (SMD), which is the diameter of the droplet that has the same surface/volume ratio as that of the total spray. Injection pressure, nozzle geometry and size, air conditions, and fuel properties all affect SMD in sprays [2].

2.2.2 Spray Evaporation

The injected liquid fuel, atomized into small drops near the nozzle exit to form a spray, must evaporate before it can mix with air and burn. Figure 2-3 showed the basic structure of a diesel spray under conditions typical of a typical DI engine: a core exists along the axis of the spray where the liquid fuel ligaments or drops are sufficiently dense. Once the initial phase of the injection process is over, the length of this core remains essentially constant until injection ends. The core is surrounded by a much larger vapor-containing spray region which continues to penetrate deeper into the combustion chamber: the core extends only partway to the spray tip. The process of droplet evaporation under normal engine operating conditions appears to be rapid relative to the total combustion period [2].

If a liquid drop at close to ambient temperature injected into air at typical end-of-compression engine conditions. Three phenomena will determine the history of the drop under these conditions:

1. Deceleration of the drop due to aerodynamic drag.
2. Heat transfer to the drop from the air.
3. Mass transfer of fuel away from the drop.

As the drop velocity decreases, the convective heat-transfer coefficient between the air and the drop decreases. As the droplet temperature increases due to heat transfer, the fuel vapor pressure increases and the evaporation rate increases. As the mass transfer rate of vapor away from the drop increases, the fraction of the heat transferred to the drop surface decreases. The combination of these factors define the evaporation rate of a drop as a function of time. Analysis of individual fuel drops 25 μm in diameter, injected into air at typical diesel conditions, indicates that evaporation times are usually less than 1 ms [2].

Such an analysis is relevant to drops that are widely separated (e.g., at the edge of the spray). In the spray core, where drop number densities are high, the evaporation process has a significant effect on the temperature and fuel-vapor concentration in the air within the spray. As fuel vaporizes, the local air temperature will decrease and the local fuel vapor pressure will increase. Eventually, thermodynamic equilibrium would be reached. Studies indicate that, under normal diesel engine conditions, 70 to 95 percent of the injected fuel is in the vapor phase at the start of combustion, and evaporation is more than 90 percent complete after 1 ms. However, only 10 to 35 percent of the vaporized fuel has mixed to within flammability limits in a typical medium-speed DI diesel engine. Thus, combustion is largely mixing-limited, rather than evaporation-limited. Just under cold-starting conditions evaporation becomes a major constraint [2].

2.3 Overview of Diesel Combustion

In compression-ignition engines, air alone is inducted into the cylinder. The fuel is injected directly into the engine cylinder just before the combustion process is required to start. Load control is achieved by varying the amount of fuel injected each cycle; the air flow at a given engine speed is essentially unchanged [2]. In opposite to spark-ignition engines, an ignition system is not required to start the combustion, as fuel of higher reactivity – diesel – is used.

Compression-ignition engines are divided into two categories according to their combustion chamber design:

1. Direct-injection (DI) engines, which have a single open combustion chamber in which fuel is injected directly;
2. Indirect injection (IDI) engines, where the chamber is divided into two regions and the fuel is injected into the prechamber which is connected to the main chamber.

The proportion of DI engines is increasing due to their more economical fuel consumption. The harsher combustion noise (particularly under acceleration) can be reduced to the level of IDI engines by pre-injection. Engines with divided combustion chambers now hardly figure at all among new developments [8].

In DI diesel engines, the fuel is usually injected at high pressure (up to 2200 bar [8]) through small orifices in the injector tip, thus achieving high velocity, as mentioned in Section 2.2. The liquid fuel atomizes into small drops and penetrates into the combustion chamber. The fuel vaporizes and mixes with the high-temperature high-pressure cylinder air. Since the air temperature and pressure are above the fuel's ignition point, spontaneous ignition of portions of the already-mixed fuel and air occurs after a short delay period. The cylinder pressure increases as combustion of the air-fuel mixture occurs. The consequent compression of the unburned portion of the charge shortens the delay before ignition for the fuel and air which has mixed to within combustible limits, which then burns rapidly. It also reduces the evaporation time of the remaining liquid fuel. Injection continues until the desired amount of fuel has entered the cylinder. Atomization, vaporization, air-fuel mixing, and combustion continue until essentially all the fuel has passed through each process. Mixing of the air remaining in the cylinder with burning and already burned gases continues throughout the combustion and expansion processes [2].

Figure 2-5 shows typical data for cylinder pressure, heat release rate (HRR, the rate at which the chemical energy of the fuel is released by the combustion process), and rate of fuel injection of a small DI diesel engine. There is a delay between the start of injection and start of combustion [identified by the change in slope of the $p(\theta)$ curve]. The pressure rises rapidly for a few crank angle degrees, then more slowly to a peak value. The HRR diagram shows negligible heat release until toward the end of compression when a slight loss of heat during the delay period (which is due to heat transfer to the walls and to fuel vaporization and heating) is evident. During the combustion process the burning proceeds in three distinguishable stages. In the first stage, the rate of burning is generally very high and lasts for only a few crank angle degrees. It corresponds to the period of rapid cylinder pressure rise. The second stage corresponds to a period of decreasing heat-release rate (though it initially may rise to a second, lower, peak as in Figure 2-5). This is the main heat-release period. Normally about 80 percent of the total fuel energy is released in the first two periods. The third stage corresponds to the "tail" of the heat-release diagram in which a small but distinguishable rate of heat release persists throughout much of the expansion stroke [2].

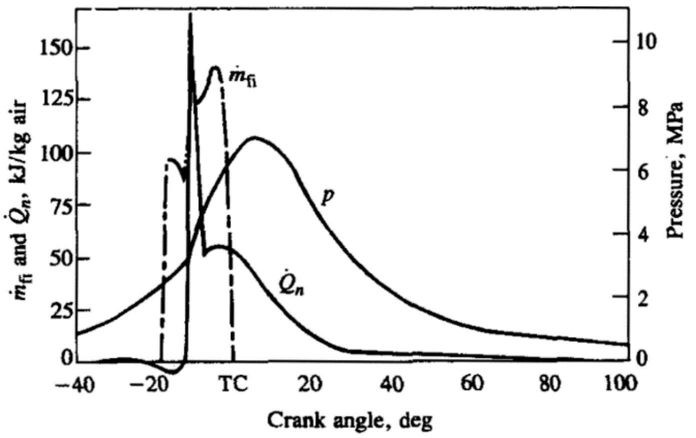

Figure 2-5 Cylinder pressure, net HRR, and rate of fuel injection for small DI diesel engine [2]

To summarize, the following stages of the overall compression-ignition diesel combustion process can be defined. They are identified on the typical heat release rate diagram for a DI engine in Figure 2-6 [2].

1. Ignition delay (ab). The period between the start of fuel injection into the combustion chamber and the start of combustion.
2. Premixed or rapid combustion phase (bc). In this phase, combustion of the fuel which has mixed with air to within the flammability limits during the ignition delay period occurs rapidly in a few crank angle degrees. When this burning mixture is added to the fuel which becomes ready for burning and burns during this phase, the high heat release rates characteristic of this phase result.
3. Mixing-controlled combustion phase (cd). Once the fuel and air which premixed during the ignition delay have been consumed, the burning rate (or heat release rate) is controlled by the rate at which mixture becomes available for burning. While several processes are involved – liquid fuel atomization, vaporization, mixing of fuel vapor with air, preflame

chemical reactions – the rate of burning is controlled primarily by the fuel vapor-air mixing process. The heat release rate may reach a second (usually lower) peak in this phase.

4. Late combustion phase (de). Heat release continues at a lower rate well into the expansion stroke. There are several reasons for this. A small fraction of the fuel may not yet have burned. A fraction of the fuel energy is present in soot and fuel-rich combustion products, and can still be released. The cylinder charge is nonuniform and mixing during this period promotes more complete combustion. The kinetics of the final burnout processes become slower as the temperature of the cylinder gases fall during expansion.

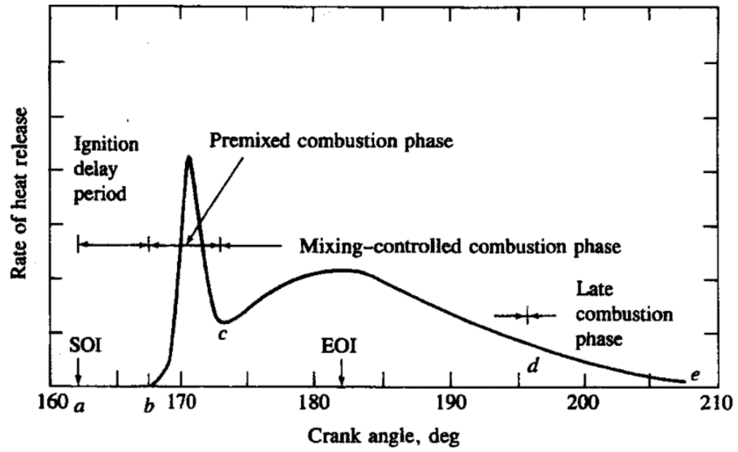

Figure 2-6 Heat release rate diagram identifying different DI diesel combustion phases [2]

2.4 Conceptual Model of Direct-Injection Diesel Combustion

A phenomenological description, or conceptual model, of how direct-injection diesel combustion occurs has been derived from laser-sheet imaging and other optical data by John E. Dec at Sandia National Laboratories [9].

Diesel combustion is a complex, turbulent, three-dimensional, multiphase process that occurs in a high-temperature and high-pressure environment. As a result, prior to the advent of advanced laser diagnostics, detailed measurements of the events occurring within a reacting diesel fuel jet were not possible. The development of advanced laser-based diagnostics has provided a means for making detailed in-situ measurements of the processes occurring inside of a reacting diesel fuel jet. These diagnostics allow specific species within the reacting jet to be measured at multiple points simultaneously (planar imaging) with high spatial and temporal resolution.

The optical-access engine used in the studies described in [9] was a single-cylinder, direct-injection, 4-stroke diesel engine. The design of this engine utilizes a classic extended piston with piston-crown window. Additional windows located around the top of the cylinder wall provide the orthogonal optical access required for the two-dimensional (planar) laser imaging diagnostics. These windows allow the laser sheet to enter the cylinder along the axis of the fuel jet or horizontally. A window in the cylinder head replaces one of the two exhaust valves to obtain a view of the squish region and the outer portion of the combustion bowl. For more details on this engine, operating conditions, and fuels used for experiments, see [9].

Figure 2-7 shows a series of schematics that present a comprehensive picture of DI diesel combustion, showing the development of a diesel fuel jet from the start of injection, through the premixed burn, and into the first part of the mixing-controlled burn. These composite schematics represent idealized cross-sectional slices through the mid-plane of the jet, and they show conceptually how DI diesel combustion occurs in the absence of wall interactions and swirl. These schematic images depict the base operating condition in the research diesel engine, which is a typical operating condition for DI diesel combustion; however, for production engines the amount of turbocharger boost and intercooling and the injector characteristics can vary greatly, affecting both the temporal and spatial scaling [9].

In Figure 2-7, the crank angle degree after the start of injection (ASI) is given at the side of each image (1°=139 μs), and the color scheme is shown in the legend at the bottom.

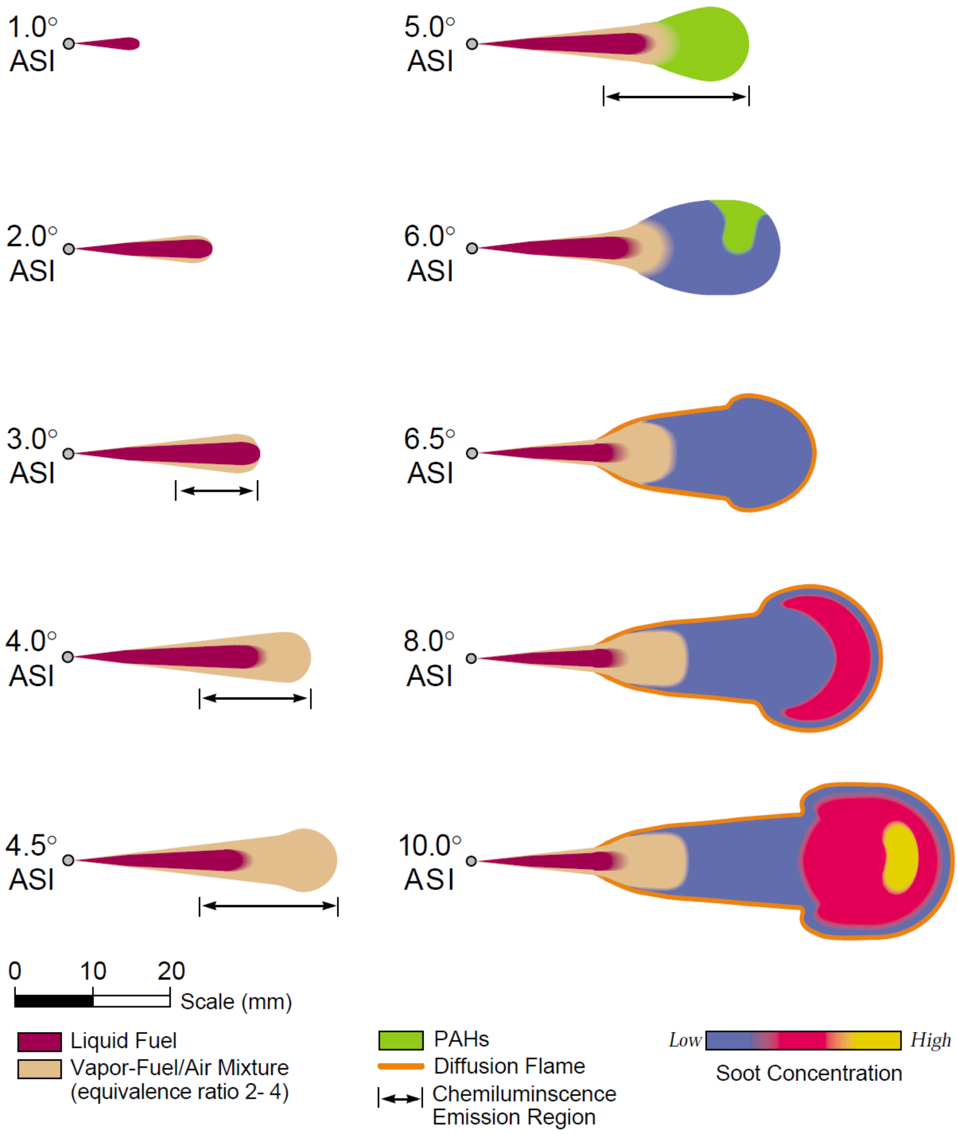

Figure 2-7 Temporal sequence of schematics showing how DI diesel combustion evolves [9]

Initial Jet Development (0.0°-4.5° ASI)

The first three images in Figure 2-7 show the jet penetration out to the point where all the liquid is vaporized. The dark brown region labeled as liquid fuel shows the maximum extent of the liquid fuel droplets. At the injector, this region contains only liquid fuel, but downstream, air is entrained and fuel vaporizes so these gases are present along with the liquid-fuel droplets.

Initially, liquid fuel covers the cross section, as shown in the 1.0° ASI schematic. Then a vapor-fuel region begins to develop along the sides of the jet beyond the extent of the liquid droplets (2.0° ASI schematic). At 3.0° ASI the liquid reaches its maximum penetration of about 23 mm. The entrainment of hot air into the jet has been sufficient to vaporize all the fuel by this point. As can be seen in the subsequent images, the gas phase continues to penetrate across the chamber, and a head vortex eventually develops. By 4.5° ASI, the jet has penetrated to about 34 mm, and the leading portion contains a relatively uniform fuel/air mixture with equivalence ratios ranging from about 2 to 4 [9].

Autoignition (3.0°-5.0° ASI)

The exact point of ignition is not well defined either temporally or spatially. Chemiluminescence (it arises from combustion radicals that are raised to an excited state by energetic chemical reactions and then subsequently decay back to equilibrium energy levels by emitting a photon; because energetic chemical reactions are required to produce this chemiluminescence, it closely marks the occurrence of combustion heat release both temporally and spatially [10]) occurs over the downstream portion of all the jets as early as 3.0° ASI. At this time the vapor has barely penetrated beyond the liquid, so this natural emission must be occurring in the vapor region along the sides of the jet. The chemiluminescent region of the jet is indicated in Figure 2-7 by the arrows under the schematics.

Initially (3.0° and 3.5° ASI) the vapor layer is not very thick, but by 4.5° ASI most of the chemiluminescence is coming from the large region of vapor-fuel/air mixture in the leading portion of the jet. In this region, it is very likely that the autoignition as marked by chemiluminescence occurs volumetrically since fuel breakdown and PAH (polycyclic aromatic hydrocarbon) formation occur volumetrically (to help determine whether the early combustion is volumetric or confined to the surface, planar laser-induced fluorescence images of the PAH emission were obtained; for more details see [9]) throughout this region between 4.5° to 5.0° ASI, followed by volumetric soot formation between 5.0° and 6.0° ASI.

First Part of Premixed Burn Spike (4.0°-6.5° ASI)

The heat release rate curve (see Figure 2-8) starts to head up at 4.0° ASI and then increases very sharply after 4.5° ASI. By 4.5° ASI the leading portion of the jet is highly chemiluminescent as indicated in the schematics, but there is little indication of significant fuel breakdown. Then by 5.0° ASI, the fuel breaks down and large PAHs form almost uniformly across the entire cross section of the leading portion of the jet, where the equivalence ratio ranges from 2 to 4. This timing coincides with the rapid rise in the heat release rate indicating that the premixed burn spike consists of the combustion of this fuel-rich mixture. By 6.0° ASI, soot occurs as very small particles throughout large portions of the cross section of the downstream portion of the fuel jet at locations that vary from cycle to cycle. These small soot particles that form up throughout the cross section are arising from the fuel-rich premixed burn. By 6.5° ASI, soot is found throughout the cross-section of the downstream region of the jet [9].

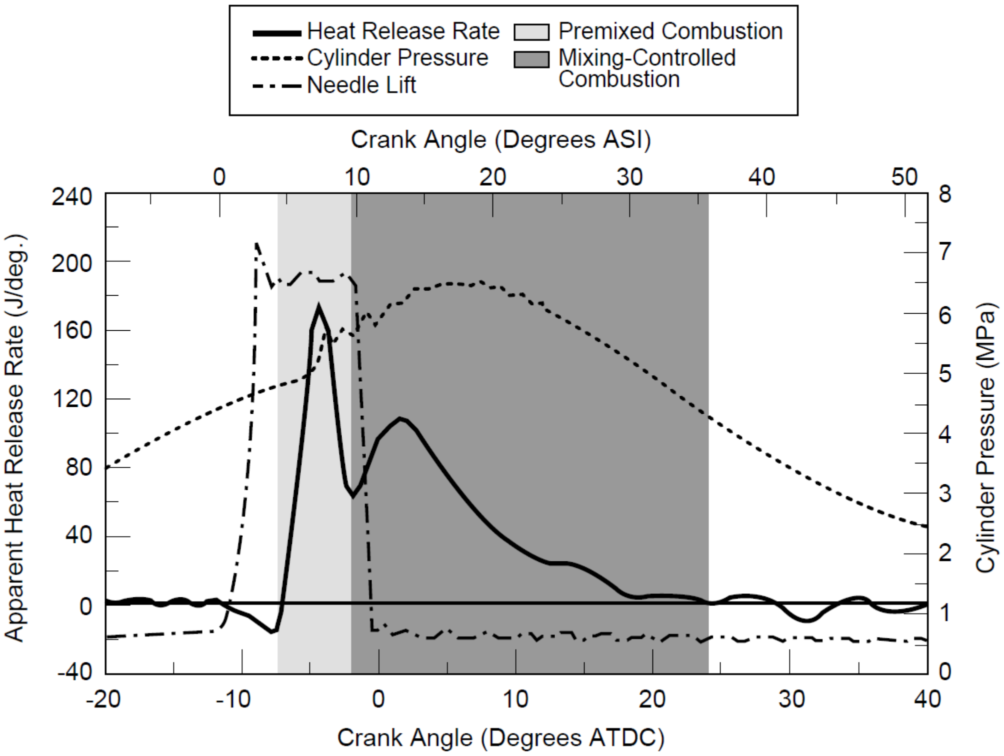

Figure 2-8 Cylinder pressure, apparent HRR, and injector needle lift for studies of conceptual model of diesel combustion [9]

Onset of the Diffusion Flame (5.5°-6.5° ASI)

Between 5.5° and 6.5° ASI, a diffusion flame forms at the jet periphery between the products of the fuel-rich premixed burn (which contain a significant quantity of unconsumed fuel) and the surrounding air. By 6.5° ASI (just prior to the midpoint of the premixed burn spike in the apparent heat release rate), this thin diffusion flame completely encircles the downstream portion of the jet as indicated by the orange color in Figure 2-7. It extends back toward the injector to a point just upstream of the tip of the liquid fuel penetration. The liquid-fuel length becomes about 2 to 3 mm shorter as the diffusion flame forms, presumably due to local heating by the flame. Also at 6.5° ASI, the soot particles become larger in a thin layer around the jet periphery, due to some effect of the diffusion flame. However, there is no indication of a corresponding increase in soot concentration (volume fraction) at the jet periphery with the formation of the diffusion flame [9].

Last Part of Premixed Burn Spike (7.0°-9.0° ASI)

Through the remainder of the premixed burn, the jet continues to grow and penetrate across the chamber. The soot concentration continues to increase throughout the cross section of the sooting region, with the greatest increase in concentration being toward the leading edge where the head vortex is forming (indicated in the 8.0° ASI schematic by the red zone near the leading edge).

The diffusion flame remains as a thin reaction zone at the jet periphery, and the larger soot particles produced by this flame become distributed inward from the periphery for a few millimeters (not shown), presumably due to turbulent mixing. However, they do not spread into the central region of the jet which is filled only with small soot particles. Although the soot particles all around the jet periphery are larger than those in the central region, the particles toward the leading edge (head-vortex region) are even larger than those along the sides of the jet. Thus, a region of even larger soot particles starts to form near the leading edge with a distribution similar to the red, high-soot-concentration region shown in the 8.0° ASI schematic. Toward the end of the premixed burn as the last of the premixed air is consumed, small soot particles present throughout the cross section extend upstream to approximately 27 mm from the injector. Going from the vapor-fuel region downstream, the soot particles appear rather abruptly across the entire cross section of the jet at this 27 mm location as shown in the 8.0° ASI schematic [9].

First Part of the Mixing-Controlled Burn (9.0° ASI to end of injection)

As the combustion transitions to being purely mixing-controlled, the overall appearance of the jet shows only moderate changes. This is probably because the jet was already almost in a mixing-controlled-burn mode as the last of the premixed fuel was burning out. As shown in the 10° ASI schematic, the jet has penetrated further, and the head vortex is becoming well formed. In addition, the soot concentration is higher throughout the head vortex, and the soot particles in the head vortex have grown much larger. However, the soot still appears quite abruptly across the entire cross section of the jet about 27 mm downstream of the injector. These soot particles are small when they first appear at the upstream edge of the sooting region, and they remain small throughout the central part of the jet, except for the head vortex region. The data also suggest that soot particles caused by the diffusion flame, that are larger than those in the central part of the jet but smaller than those in the head vortex, are still present along the sides of the jet upstream of the head vortex, like they were during the latter part of the premixed burn. The same overall jet appearance and soot distribution pattern continue up through the end of fuel injection (for the condition studied), although soot concentrations and particle sizes increase in the head vortex region [9].

Mixing-Controlled Combustion

Figure 2-9 presents a typical schematic of the conceptual model of DI diesel combustion during the mixing-controlled burn, prior to the end of fuel injection.

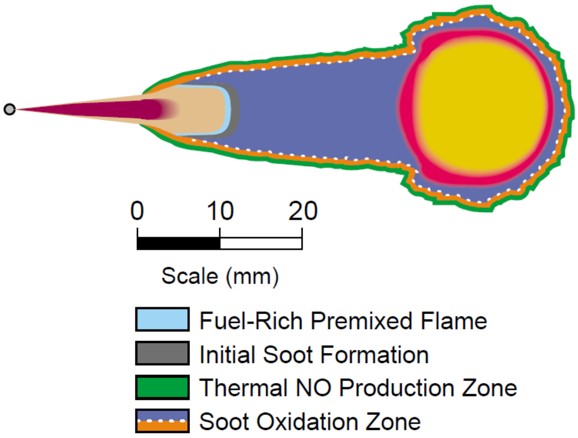

Figure 2-9 Schematic of the conceptual model of DI diesel combustion for the first part of the mixing controlled burn [9]

Temporally, the schematic in Figure 2-9 follows the last one in the sequence (10° ASI) in Figure 2-7, and it is representative of the remainder of the mixing-controlled burn up until the end of injection. This schematic is similar in appearance to the 10° ASI schematic in Figure 2-7 except that the jet is somewhat larger, and the soot concentration in the head vortex is higher. The soot particles in the head vortex have also grown larger.

Going from the injector down the jet, Figure 2-9 shows that turbulent air entrainment is sufficient to vaporize all the fuel by the time it has traveled about 18-19 mm from the injector (for this operating condition). A short distance downstream of this point, the vapor fuel and entrained air have formed a relatively uniform mixture. Then, at about 27 mm from the injector, soot appears as small particles across the entire cross section of the jet. The soot concentration and particle size increase down the jet, with the highest soot concentrations and largest soot particles occurring in the head vortex. This soot distribution pattern, combined with the flow patterns in a penetrating jet, suggests that soot formation starts at the 27 mm location, and that formation and particle growth continue as the soot moves down the jet to the head vortex. The soot particles then accumulate in the recirculating head vortex where they have time to grow to a very large size. In addition, some of the soot particles eventually reach the diffusion flame at the periphery of the jet where they can be oxidized by OH radical attack [9].

A standing fuel-rich premixed flame, just upstream of where the soot first appears, is also depicted in Figure 2-9. Prior to combustion, the fuel and air are well mixed to a fuel-rich but combustible mixture (equivalence ratio of 2 to 4) just downstream of the maximum liquid penetration. Although the amount of air entrainment would be lower due to the shorter liquid length and presence of the diffusion flame, a significant quantity of air would still be mixed with the fuel by the time the last liquid has vaporized. This nearly uniform, fuel-rich mixture (perhaps an equivalence ratio of 3 to 5) would support a standing premixed flame across the jet just upstream of where the soot appears. A fuel-rich flame of this type would create an almost ideal environment for soot production because the products contain an abundance of excess fuel and are sufficiently hot for fuel pyrolysis and soot formation. This is believed to be the cause of the initial soot formation across the entire jet cross-section at about 27 mm [9].

This standing premixed flame is thought to be established during the later stages of the initial premixed burn, from about 6.0° to 8.0° ASI as the fuel-rich mixture flows into the zone undergoing the initial premixed burn. The presence of this standing premixed flame throughout the mixing controlled burn, combined with the description of the premixed-burn-spike combustion shown in Figure 2-7, would mean that all of the fuel (both for the premixed and mixing-controlled burn) first undergoes fuel-rich premixed combustion and later diffusion-flame combustion. Furthermore, the diffusion-flame combustion would occur as a flame between the products of the fuel-rich premixed combustion and air rather than being a more classical pure-fuel/air diffusion flame [9].

2.5 Pollutant Emissions from Compression-Ignition Engines

In the diesel engine, the fuel is injected into the cylinder just before combustion starts, so throughout most of the critical parts of the cycle the fuel distribution is nonuniform. The pollutant formation processes are strongly dependent on the fuel distribution and how that distribution changes with time due to mixing [2]. Figure 2-10 illustrates how various parts of the fuel jet and the flame affect the formation of nitric oxide (NO), unburned hydrocarbons (HC), and soot (or particulates) during the premixed and mixing-controlled phases of diesel combustion in a direct-injection engine with swirl. Note, that in the conventional diesel combustion the formation of carbon monoxide (CO) is not significant as the environment is overall lean.

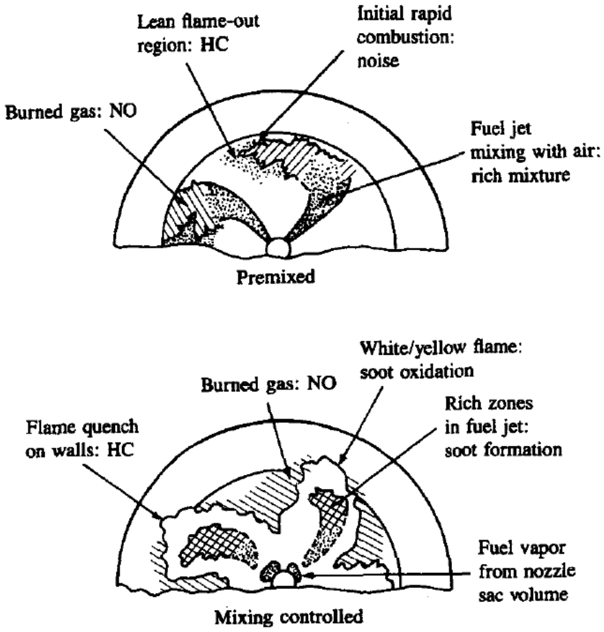

Figure 2-10 Summary of pollutant formation mechanisms in DI diesel engine [2]

Thermal NO forms at the diffusion flame and in the high-temperature burned gas regions, but temperature and fuel/air ratio distributions within the burned gases are nonuniform and formation rates are highest in the close-to-stoichiometric regions. Soot forms in the standing fuel-rich premixed flame, as explained in Section 2.4. Soot then oxidizes in the diffusive flame zone by OH radical attack and by the contact with unburned oxygen. Hydrocarbons (HC) and aldehydes originate in regions where the flame quenches both on the walls and where excessive dilution with air prevents the combustion process from either starting or going to completion. Fuel that vaporizes from the nozzle sac volume during the later stages of combustion is also a source of HC [2].

Going back to the conceptual model of DI diesel combustion, Figure 2-9 shows regions of soot formation, soot oxidation and NO production during the mixing controlled burn. As shown by the gray zone in the figure, the initial soot formation occurs just downstream of the standing fuel-rich premixed flame in the products of the rich combustion. By the time these rich-combustion products reach about 27 mm (in the analyzed case), small soot particles form throughout the mixture. Then, as discussed in Section 2.4, soot formation and particle growth continue as the soot moves down the jet to the head vortex and outward to the diffusion flame. The diffusion flame is the only source of high OH radical concentrations (for more details refer to the reference [9]), and OH radical attack is thought to be the primary method of soot oxidation. Oxygen attack may also play a role, but the diffusion flame is the only location where oxygen would be expected. Thus, soot oxidation is almost certainly occurring at the diffusion flame throughout this portion of the combustion event. This is indicated by the dashed white line in Figure 2-9 [9].

Figure 2-7 and Figure 2-9 show that for typical diesel conditions virtually all of the premixed combustion is fuel rich, in the range of an equivalence ratio of 4. This includes both the initial premixed burn just after autoignition and the standing premixed flame during the mixing-controlled burn. These conditions are not conducive to NO production either by the “thermal” or "prompt" mechanisms. Little oxygen is present and adiabatic flame temperatures (about 1600 K) are far below those required for significant thermal NO production. For prompt NO, calculations and experiments show little NO produced at equivalence ratios above 1.8 [9].

Subsequent to this fuel-rich premixed combustion, the remaining fuel burns as a diffusion flame at the jet periphery. At the diffusion flame temperatures will be high (combustion is nearly stoichiometric), and there is a source of oxygen. These conditions are nearly ideal for thermal NO production. Accordingly, up through the end of fuel injection high NO production rates by the thermal mechanism are expected only around the jet periphery on the lean side of the diffusion flame, as indicated by the green line in Figure 2-9. However, it is important to realize that this NO production zone may not be the location where most of the NO is produced during typical diesel combustion. Thermal NO production is a relatively slow process, and this could delay the onset of significant NO production until after the end of fuel injection. Hence, the bulk of the NO production might occur during the latter part of the mixing controlled burn or in hot-gas regions that remain after the end of combustion. Although peak temperatures may be lower in these regions than they are at the diffusion flame prior to the end of injection, there is considerably more time for the NO production reactions, and the volume of gas involved could be much larger [9].

In addition, some NO may be produced at the diffusion flame by the "prompt" mechanism and by conversion of "fixed nitrogen" from the rich premixed combustion. However, for combustion at diesel temperatures these mechanisms are less important than the "thermal" mechanism [9].

2.5.1 Effects of Engine Parameters on Diesel Pollutant Emissions

Effect of Swirl

Effects that swirl has on diesel pollutant emissions can be summarized as follows:

1. NOx and particulate levels are very sensitive to inlet swirl ratio [11].
2. NOx levels in the exhaust have a direct relation to the maximum dp/dθ and peak cylinder pressure which in the case of a DI diesel engine occurs during premixed phase of combustion under normal operating conditions. An increase in swirl ratio increased the rate of pressure rise resulting in higher NOx levels in the exhaust [11, 12].
3. Since swirl enhances mixing and probably produces a leaning effect, soot production is reduced and soot oxidation is increased, resulting in a reduction in soot emissions [12].
4. Although an increase in swirl improves the premixed combustion phase, an excess of swirl has been found to damage the diffusion-controlled combustion phase, increasing soot emissions and fuel consumption, but reducing NOx emissions. The optimum swirl value has been found for each engine operating mode [12].
5. There is no single optimum value of swirl ratio for the whole engine operating range, and matching the level of swirl with other parameters is a task that depends on the combustion chamber geometry and injection characteristics [12].

Effect of Injection Pressure

Increasing the injection pressure was found to reduce the ignition delay causing simultaneously a rapid rise in the heat release rate; this trend is enhanced for retarded injection timing. Increasing the injection pressure gives rise to the formation of smaller droplets which evaporate faster, thus improving the air-fuel mixing process and resulting in favorable conditions for autoignition. The shorter ignition delay period brings the start of combustion closer to TDC and a rapid rise in heat release which are both associated with higher temperatures and increased NOx emissions. Also, increased injection pressure results in reduced soot levels. Despite the fact that the ignition delay period becomes shorter with an increase in the injection pressure, which is believed to increase soot levels due to the reduced time for air-fuel mixing prior to combustion, the higher injection rate and the reduced droplet sizes seem to enhance evaporation to allow more fuel to be mixed with air prior to combustion [13].

On the other hand, under heavy-load conditions, soot increases significantly at very retarded injection timings since the later part of the mixing-controlled combustion phase is frozen as the cylinder pressure drops. At light load conditions, soot levels decrease since the mixing-controlled combustion phase finishes before the limit of soot oxidation freezing temperature is reached [13].

Effect of Nozzle Hole Size

Reducing the nozzle hole size results in a significant increase of the injection pressure, a small decrease in the peak injection rate, and a slight decrease in ignition delay (which is attributed to faster evaporation of the smaller droplets formed at higher injection pressure conditions). Thus, reducing nozzle hole size results in lower soot and higher NOx emissions, but the rate of decrease in smoke and the rate of increase in NOx was found to be greater than that in the case of increased injection pressure for the case of the same nozzle. It appears that the smaller nozzle hole is more effective in improving the soot-NOx trade-off curve than raising the injection pressure [13].

However, it is not the optimum solution since the injection duration increases excessively at higher loads when nozzle holes are reduced, although the injection pressure remains nearly the same. The end result is a significant increase in soot levels because the soot formed at the late period of combustion cannot be oxidized due to the low cylinder temperatures. Therefore, smaller nozzle holes should be employed in conjunction with higher injection pressures in order to maintain proper injection duration and injection rate [13].

Effect of Injection Timing

One of the most important parameters controlling diesel engine exhaust emissions is the injection timing. NOx emissions decrease and soot emissions increase with retarded injection timing but the trend starts reversing when the start of injection is retarded beyond TDC; this is due to the long ignition delay which causes a significant increase in the premixed burn fraction, leading to higher NOx levels and decreased soot emissions. Since the ignition delay period is shorter in the case of the increased injection pressure, the injection timing at the minimum soot-NOx trade-off point was found to be closer to TDC in the case of higher injection pressures [13].

3 Computational Fluid Dynamics Fundamentals

3.1 Overview

Flows and related phenomena can be described by partial differential (or integro-differential) equations, which cannot be solved analytically except in special cases. To obtain an approximate solution numerically, a discretization method has to be used which approximates the differential equations by a system of algebraic equations, which can then be solved on a computer. The approximations are applied to small domains in space and/or time so the numerical solution provides results at discrete locations in space and time [14]. This application of numerical methods to solve and analyze problems related to fluid flows is, in essence, what is called computational fluid dynamics (CFD).

CFD is the most sophisticated approach for detailed numerical investigations on thermo-fluid dynamical problems. In other words, it is a tool to carry out numerical experiments, as physical experiments are usually too complicated, or too expensive to be done.

CFD is playing an increasingly important role in the simulation of engine processes, as it makes possible the most detailed physical description of the relevant processes, like gas exchange during intake and exhaust strokes, in-cylinder flow, exhaust gas recirculation, secondary reactions in the exhaust tract, catalyst converter flow, turbine and compressor flow in the turbocharger, internal nozzle flow, or coolant flow [15].

To obtain results representative of real phenomena using CFD, several conditions have to be met: (1) appropriate discretization of the flow domain (mesh generation), able to properly capture relevant physical processes; (2) correct boundary and initial conditions, including pressures, temperatures, turbulence parameters, and other; (3) models used for simulation of various processes (spray, combustion, turbulence, etc.) have to be calibrated using experimental data, which is often not possible; thus experience available from past simulations, or provided in literature is applied, usually introducing some errors.

Finally, it has to be noted that CFD is typically a computationally expensive process, requiring high processing power to execute a simulation in a convenient time. Taking into consideration that during research and development of internal combustion engines many simulations have to be run in order to investigate effects of different parameters on the engine's performance, high computational cost results in longer development time, thus higher monetary expenses.

3.2 Governing Equations

Fundamental equations of fluid dynamics – continuity, momentum, and energy equations – are the base for computational fluid dynamics. These equations mathematically represent three fundamental physical principles upon which all of fluid dynamics is based [16]:

1. Mass is conserved.
2. Newton’s second law, $\vec{\mathrm{F}} = \mathrm{m}\vec{\mathrm{a}}$.
3. Energy is conserved.

Governing equations can be obtained in different forms (integral or partial differential, conservation or non-conservation), depending on what model of the flow they are applied. The roadmap for derivation of these equations is shown in Figure 3-1.

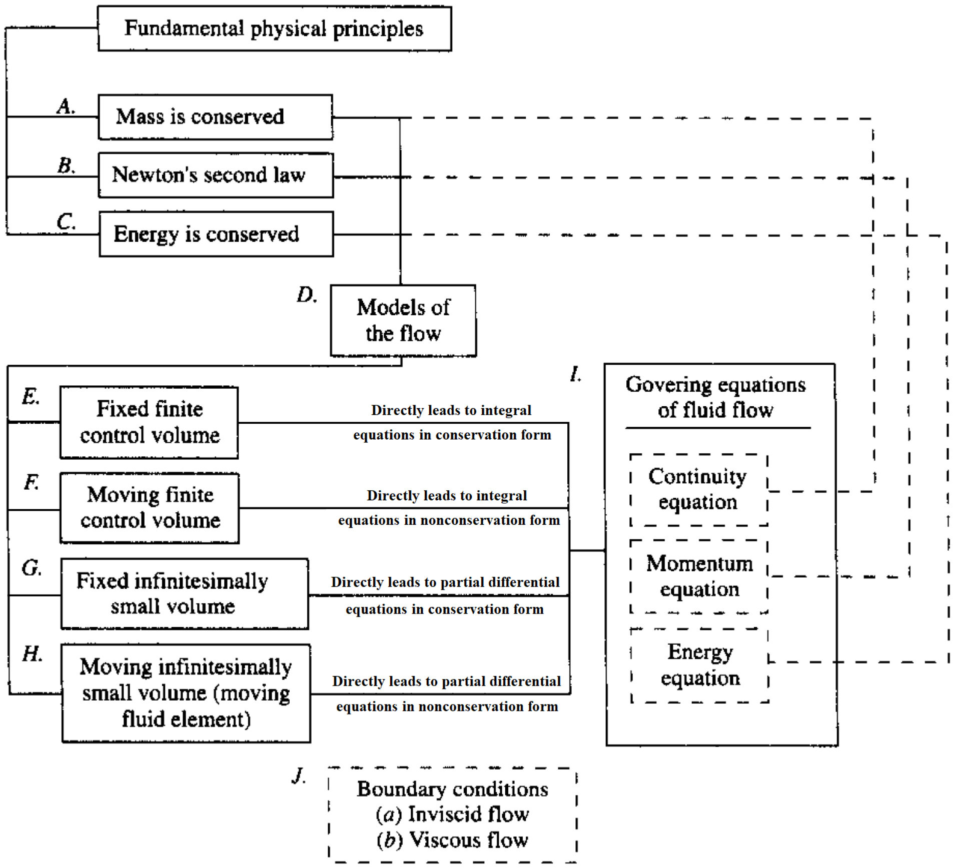

Figure 3-1 Road map for derivation of governing equations [16]

As can be seen in Figure 3-1, there are four different models of the flow, each of them producing a different mathematical statement of the governing equations:

1. Fixed finite control volume (Figure 3-2a, left), where the control volume V (reasonably large, finite region of the flow) is fixed in space with the fluid moving through it. Integral equations in conservation form are obtained.
2. Moving finite control volume (Figure 3-2a, right), where the control volume V is moving with the fluid such that the same fluid particles are always inside it. Integral equations in non-conservation form are obtained.
3. Fixed infinitesimally small volume (Figure 3-2b, left), where the differential volume dV (large enough to contain a huge number of molecules) is fixed in space with the fluid moving through it. Partial differential equations in conservation form are obtained.
4. Moving infinitesimally small volume (Figure 3-2b, right), where the differential volume dV moves along a streamline. Partial differential equations in non-conservation form are obtained.

In the limit of a very fine grid, all equation forms and numerical solution methods give the same solution; however, on coarse grids the non-conservative form introduces additional errors which may become important [14].

The governing equations must be solved subject to the physical boundary conditions. The physical aspects of the boundary conditions are fundamentally independent of the forms of the governing equations, and hence the box representing the boundary conditions stands by itself at the bottom of Figure 3-1, unconnected to any of the other boxes in the road map [16].

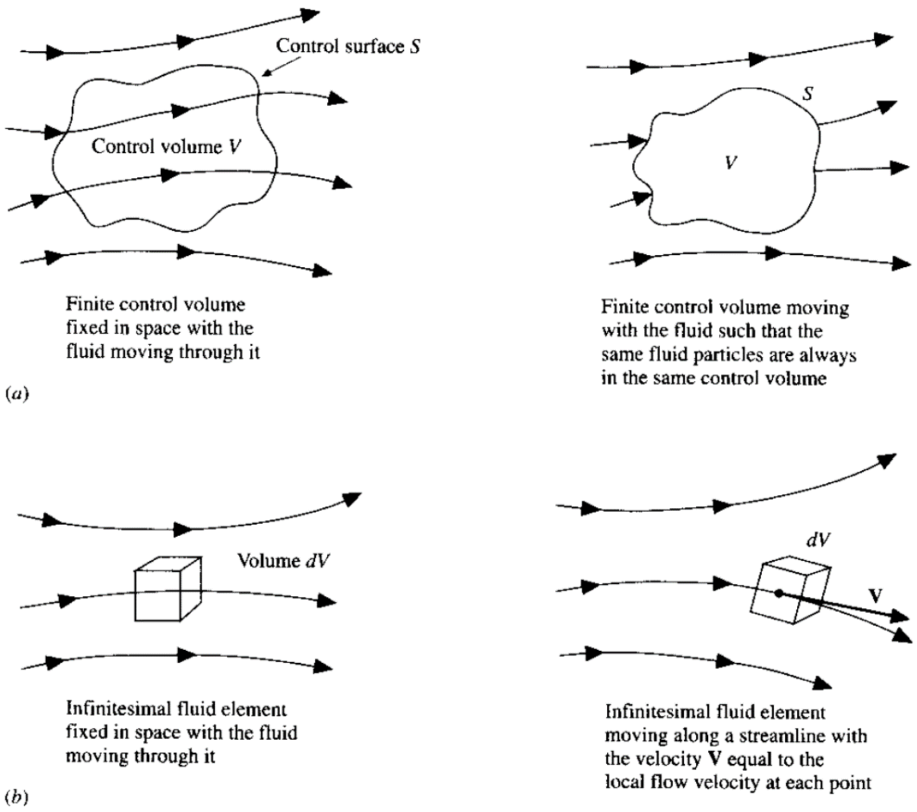

Figure 3-2 Models of the flow [16]

The conservation of linear momentum in differential form was derived originally by Stokes and independently by Navier and, therefore, is known as the Navier-Stokes equation. It is common to refer to the entire system of equations in differential form composed of conservations of mass, momentum, and energy as the Navier-Stokes equations [17].

In fluid flows, however, it is difficult to follow a parcel of matter (an infinitesimally small volume). It is more convenient to deal with the flow within a control volume. This method of analysis is called the control volume approach [14].

3.2.1 Continuity Equation

The governing flow equation which results from the application of conservation of mass physical principle to any one of the models of the flow shown in Figure 3-2 is called the continuity equation.

This conservation law requires that mass is neither created nor destroyed. Applied to the finite control volume fixed in space (shown at the left of Figure 3-2a), this fundamental physical principle means that net mass flow out of control volume through surface S is equal to time rate of decrease of mass inside control volume. Thus an integral form of the continuity equation in conservation form is obtained as:

$$\frac{\partial}{\partial t}\int_{\mathcal{V}} \rho d\mathcal{V} + \int_{S} \rho \vec{V}\cdot\vec{n} dS = 0, \tag{3.1}$$

where $\mathcal{V}$ – control volume, S – surface enclosing the control volume, $\vec{n}$ – unit vector orthogonal to S, $\vec{V}$ – fluid velocity.

When considering an infinitesimally small fluid element fixed in space as shown in Figure 3-2b on the left, Eq. (3.1) can be rewritten in its partial differential conservative form, which still represents the same physical meaning: the net mass flow out of the element must equal the time rate of decrease of mass inside the element. This statement is expressed as:

$$\frac{\partial \rho}{\partial t} + \nabla \cdot \left(\rho \vec{V}\right) = 0, \tag{3.2}$$

where $\nabla \cdot \left(\rho \vec{V}\right)$ term represents divergence of the velocity times density.

Finally, it can be demonstrated that all four equations (shown in Figure 3-1), including those expressed by Eqs. (3.1) and (3.2), are four different forms of the same equation. Any of these four forms can be derived by manipulation from any of the others [16].

3.2.2 Momentum Equation

The momentum equation is based on Newton's second law, $\vec{F} = m\vec{a}$. This law, when applied to the fluid element, says that the net force on the fluid element equals its mass times the acceleration of the element. There are two sources of this force [16]:

1. Body forces, which act directly on the volumetric mass of the fluid element. Examples are gravitational, electric, and magnetic forces.
2. Surface forces, which act directly on the surface of the fluid element. They are due to only two sources: (a) the pressure distribution acting on the surface, imposed by the outside fluid surrounding the fluid element, and (b) the shear and normal stress distributions (due to viscous effects) acting on the surface, also imposed by the outside fluid on the surface by means of friction.

The surface forces due to pressure and stresses are, from the molecular point of view, the microscopic momentum fluxes across a surface. If these fluxes cannot be written in terms of the properties whose conservation the equations govern (density and velocity), the system of equations is not closed; that is there are fewer equations than dependent variables and solution is not possible [14]. This possibility can be avoided by considering that the fluid is Newtonian (fluid in which shear stress is proportional to the time rate of strain, i.e., velocity gradients); fortunately, the Newtonian model applies to many actual fluids.

An integral form of the momentum equation in conservation form (obtained for a finite control volume fixed in space, as shown in Figure 3-2a on the left) is obtained as:

$$\frac{\partial \rho}{\partial t} \int_{\mathcal{V}} \rho \vec{V} d\mathcal{V} + \int_{S} \rho \vec{V} \vec{V} \cdot \vec{n} dS = \int_{S} \vec{T} \cdot \vec{n} dS + \int_{\mathcal{V}} \rho \vec{b} d\mathcal{V}, \tag{3.3}$$

where $\mathcal{V}$ – control volume, S – surface enclosing the control volume, $\vec{n}$ – unit vector orthogonal to S, $\vec{V}$ – fluid velocity, T – stress tensor, $\vec{b}$ – body forces (per unit mass).

This equation states that the sum of the forces acting on a control volume is equal to the sum of the rate of change of linear momentum within the control volume and net efflux of the linear momentum across the control surfaces [17].

The stress tensor term, present in Eq. (3.3), is the molecular rate of transport of momentum, and can be written:

$$\vec{T} = -\left(p + \frac{2}{3}\mu\nabla\cdot\vec{V}\right)I + 2\mu D, \tag{3.4}$$

where p – static pressure, μ – dynamic viscosity, I – unit tensor, D – rate of strain tensor:

$$D = \frac{1}{2}\left[\nabla\vec{V} + \left(\nabla\vec{V}\right)^{T}\right], \tag{3.5}$$

where $\nabla\vec{V}$ – gradient of the velocity, while superscript ^{T} means transpose.

The partial differential conservation form of Eq. (3.3) is written:

$$\frac{\partial(\rho\vec{V})}{\partial t} + \nabla\cdot\left(\rho\vec{V}\,\vec{V}\right) = \nabla\cdot T + \rho\vec{b} \tag{3.6}$$

Eq. (3.6) is the Navier-Stokes equation (in a coordinate-free vector form) in conservation form. However, usually separate equations for each direction (for Cartesian coordinates) are written.

The momentum equations are said to be in "strong conservation form" if all terms have the form of the divergence of a vector or tensor. The strong conservation form of the equations, when used together with a finite volume method, automatically insures global momentum conservation in the calculation. This is an important property of the conservation equations and its preservation in the numerical solution is equally important [14]. Eq. (3.6) is in strong conservation form.

3.2.3 Energy Equation

Energy equation is based on the third physical principle as itemized at the beginning of Section 3.2, namely, energy is conserved.

The physical principle stated above is the first law of thermodynamics. When applied to the flow model of a finite control volume fixed in space, the first law states that rate of change of energy inside the control volume is equal to the sum of rate of heat transfer to the control volume and rate of work done on the control volume. This conservation law may be expressed as:

$$\frac{d(\rho e_t)}{dt} = \frac{\partial Q}{\partial t} + \frac{\partial W}{\partial t}, \tag{3.7}$$

where e_t – total energy of the system per unit mass, $\frac{\partial Q}{\partial t}$ and $\frac{\partial W}{\partial t}$ represent the rate of heat transfer to the system and the rate of work done on the system, respectively.

Eq. (3.7) can be rewritten in the integral form:

$$\frac{\partial\rho}{\partial t}\int_{\mathcal{V}} \rho e_t d\mathcal{V} + \int_{S} e_t\left(\rho\vec{V}\cdot\vec{n}\right)dS = \dot{Q} + \dot{W} \tag{3.8}$$

In general, the total energy is the sum of the internal energy (the internal energy is the energy of each molecule or atom, summed over all the molecules and atoms in the system), kinetic energy (due to translational motion of the fluid element) and potential energy, or in terms of energy per unit mass:

$$e_t = e + \frac{1}{2}V^2 + gz, \tag{3.9}$$

where e – internal energy per unit mass, g – gravitational acceleration, z – altitude.

The partial differential conservation form of the energy equation, written in terms of total energy:

$$\begin{gathered}\frac{\partial}{\partial t}(\rho e_t) + \nabla \cdot \left(\rho e_t \vec{V} + p\vec{V}\right) = \frac{\partial}{\partial x}\left[u\tau_{xx} + v\tau_{xy} + w\tau_{xz} - q_x\right] \\ + \frac{\partial}{\partial y}\left[u\tau_{yx} + v\tau_{yy} + w\tau_{yz} - q_y\right] + \frac{\partial}{\partial z}\left[u\tau_{zx} + v\tau_{zy} + w\tau_{zz} - q_z\right],\end{gathered} \tag{3.10}$$

where q – heat flux.

3.2.4 Equation of State

The governing equations of fluid motion typically involve more unknowns than available conservation equations which include conservations of mass, momentum, and energy. Therefore, in order to close the system, additional relations such as the equation of state must be introduced.

For example, considering five conservation equations (the continuity equation, the three momentum equations, and the energy equation), there are seven unknowns ρ, p, e, T, u, v, w. It is obvious that two additional equations are required to close the system. These two additional equations can be obtained by determining relations that exist between the thermodynamic variables. Relations of this type are known as equations of state [18].

According to the state principle of thermodynamics, the local thermodynamic state is fixed by any two independent thermodynamic variables, provided that the chemical composition of the fluid is not changing owing to diffusion or finite-rate chemical reactions. For most problems in gas dynamics, it is possible to assume a perfect gas. A perfect gas is defined as a gas whose intermolecular forces are negligible. A perfect gas obeys the perfect gas equation of state:

$$p = \rho R T, \tag{3.11}$$

where R – gas constant, which can be defined by the universal gas constant $\mathcal{R}$ divided by the molecular weight:

$$R = \frac{\mathcal{R}}{M} \tag{3.12}$$

According to thermodynamics, for a perfect gas the internal energy e depends on T only, which gives a second equation of state:

$$\mathrm{e} = \mathrm{e}(T) \tag{3.13}$$

Seven equations are finally obtained: five conservation laws and two equations of state. Because the conservation laws contain time-evolution equations for ρ and e, it is best to take these as two independent state variables. Because of the explicit occurrence of T in Eq. (3.11) and the simplicity of relation in Eq. (3.13) it may be a little more convenient to use T instead of e. Given ρ and T, the other state variables p and e follow from the two equations of state [19].

The intermolecular forces become important under conditions of high pressure and relatively low temperature. For these conditions, the gas no longer obeys the perfect gas equation of state, and an alternative equation of state must be used.

3.3 Discretization Methods

The starting point of any numerical method is the mathematical model, i.e. the set of partial differential or integro-differential equations and boundary conditions.

After selecting the mathematical model, a suitable discretization method has to be chosen, i.e. a method of approximating the differential equations by a system of algebraic equations for the variables at some set of discrete locations in space and time. There are many approaches, but the most important of which are: finite difference (FD), finite volume (FV) and finite element (FE) methods. Each type of method yields the same solution if the grid is very fine. However, some methods are more suitable to some classes of problems than others [14].

Discretization yields a large system of non-linear algebraic equations. The method of solution depends on the problem. One of the methods will be presented in Section 4.2.

3.3.1 Finite Difference Method

The starting point is the conservation equation in differential form. The solution domain is covered by a grid. At each grid point, the differential equation is approximated by replacing the partial derivatives by approximations in terms of the nodal values of the functions. The result is one algebraic equation per grid node.

Taylor series expansion or polynomial fitting is used to obtain approximations to the first and second derivatives of the variables with respect to the coordinates. When necessary, these methods are also used to obtain variable values at locations other than grid nodes (interpolation).

It is the easiest method to use for simple geometries. The disadvantage of FD methods is that the conservation is not enforced unless special care is taken. Also, the restriction to simple geometries is a significant disadvantage in complex flows [14].

3.3.2 Finite Volume Method

The FV method uses the integral form of the conservation equations as its starting point. The solution domain is subdivided into a finite number of contiguous control volumes (CVs), and the conservation equations are applied to each CV. At the centroid of each CV lies a computational node at which the variable values are to be calculated. Interpolation is used to express variable values at the CV surface in terms of the nodal (CV-center) values. Surface and volume integrals are approximated using suitable quadrature formulae. As a result, one obtains an algebraic equation for each CV, in which a number of neighbor nodal values appear.

The FV method is suitable for complex geometries. The grid defines only the control volume boundaries and need not be related to a coordinate system. Another advantage of the finite-volume method is that mass, momentum, and energy are automatically conserved, since the integral forms of the governing equations are solved.

The disadvantage of FV methods compared to FD schemes is that methods of order higher than second are more difficult to develop in 3D. This is due to the fact that the FV approach requires three levels of approximation: interpolation, differentiation, and integration [14].

The popularity of the FV method in CFD stems from the high flexibility it offers as a discretization method. It owes much of its flexibility and popularity to the fact that discretization is carried out directly in the physical space with no need for any transformation between the physical and the computational coordinate system [20].

3.3.3 Finite Element Method

The FE method is similar to the FV method in many ways. The domain is broken into a set of discrete volumes or finite elements. The distinguishing feature of FE methods is that the equations are multiplied by a weight function before they are integrated over the entire domain. In the simplest FE methods, the solution is approximated by a linear shape function within each element in a way that guarantees continuity of the solution across element boundaries. Such a function can be constructed from its values at the corners of the elements.

This approximation is then substituted into the weighted integral of the conservation law and the equations to be solved are derived by requiring the derivative of the integral with respect to each nodal value to be zero. The result is a set of non-linear algebraic equations.

An important advantage of finite element methods is the ability to deal with arbitrary geometries. The grids are easily refined; each element is simply subdivided. The principal drawback is that the matrices of the linearized equations are not as well structured as those for regular grids making it more difficult to find efficient solution methods [14].

3.4 Turbulence Modeling

The vast majority of engineering applications in fluids involves turbulence. A turbulent flow may be defined as a flow which contains self-sustaining fluctuations of flow properties imposed on the main flow. It is highly unsteady, three-dimensional and contains a great deal of vorticity.

There are several factors which may cause an originally laminar flow to transition to turbulence. The fundamental quantity in describing transition to turbulent flow is the Reynolds number:

$$\mathrm{Re} = \frac{\rho V L}{\mu}, \tag{3.14}$$

where ρ – density of the fluid, V – velocity of the fluid with respect to the object, L – characteristic linear dimension, μ – dynamic viscosity of the fluid.

For example, for internal pipe flow a transition to turbulent flow can be achieved at around a Reynolds number of 2300 and for a boundary layer flow over a flat plate at a Reynolds number of around 300,000-500,000.

Several important factors affecting transition to turbulent flow include freestream turbulence, pressure gradient, heat transfer, surface roughness, and surface curvature [17].

In the past, the primary approach to studying turbulent flows was experimental. Overall parameters such as the time-averaged drag or heat transfer are relatively easy to measure but as the sophistication of engineering devices increases, the levels of detail and accuracy required also increase, as does cost and the expense and difficulty of making measurements. To optimize a design, it is usually necessary to understand the source of the undesired effects; this requires detailed measurements that are costly, time-consuming and sometimes almost impossible to make. As a result, numerical methods have an important role to play [14].

The conservation equations in differential form (the Navier-Stokes equations) can be solved numerically to predict transition and evolution of turbulence. In fact, the Navier-Stokes equations can be numerically solved for any turbulent flow and it is common to refer to the approach as Direct Numerical Simulation (DNS). However, this approach requires massive computational power (as all scales of turbulence from smallest to largest must be accommodated) and thus is impractical for most engineering applications: since the number of grid points that can be used in a computation is limited by the processing speed and memory of the machine, DNS is possible only for flows at relatively low Reynolds numbers and in geometrically simple domains [14].

Another approach is the Large Eddy Simulation (LES), where large scale structure in the flow are directly simulated, whereas small scales are filtered out and are computed by turbulence models called subgrid scale models. The small scale eddies are more uniform and have more or less common characteristics. Therefore, modeling of small scale turbulence appears more appropriate and the models should apply over wide range of applications. From numerical point of view (compared with DNS), since the small-scale turbulence is now modeled, the grid spacing could be much larger than Kolmogorov length scale. This in turn allows applications of LES to larger Reynolds numbers possible [17]. As a result, LES requires significantly less computational effort and is more applicable for practical purposes.

Third approach is based on equations obtained by averaging the equations of motion over time (if the flow is statistically steady), over a coordinate in which the mean flow does not vary, or over an ensemble of realizations (an imagined set of flows in which all controllable factors are kept fixed). Thus all of the unsteadiness is averaged out, i.e. all unsteadiness is regarded as part of the turbulence. This approach is called one-point closure and leads to a set of partial differential equations called the Reynolds-averaged Navier-Stokes (or RANS) equations. These equations do not form a closed set, so the introduction of approximations (turbulence models) is required [14].

The complexity of turbulence makes it unlikely that any single Reynolds-averaged model will be able to represent all turbulent flows, so turbulence models should be regarded as engineering approximations rather than scientific laws.

As engineers are normally interested in knowing just a few quantitative properties of a turbulent flow, such as the average forces on a body, the degree of mixing between two incoming streams of fluid, or the amount of a substance that has reacted, using the methods described above (DNS or LES) to compute these quantities is not practical (due to large computational effort required). These methods should only be used as a last resort, when nothing else succeeds or, occasionally, to check the validity of RANS which produces less information [14].

Finally, the schematic representation of the turbulent kinetic energy spectrum as a function of the wavenumber k (inverse of the eddy size) is shown in Figure 3-3, which graphically explains differences of application of the tree numerical approaches described.

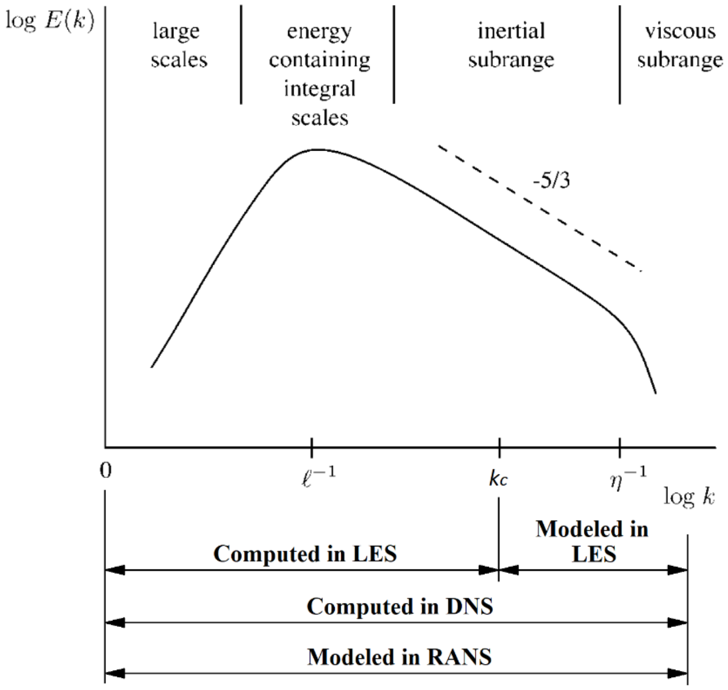

Figure 3-3 Turbulent kinetic energy spectrum as a function of the wavenumber k. Application areas of DNS, LES and RANS are shown. kc is the cutoff wavenumber for LES method, l is the integral length scale, and η is the Kolmogorov length scale

3.4.1 Reynolds-Averaged Navier-Stokes (RANS) Equations

As has been mentioned above, solving RANS equations to describe turbulence is usually sufficient for most of engineering applications, as knowing just a few quantitative properties of a turbulent flow is required.

In Reynolds-averaged approaches to turbulence, all of the unsteadiness is averaged out i.e. all unsteadiness is regarded as part of the turbulence. Traditionally this modification is accomplished by representing the instantaneous flow quantities by the sum of a mean value and a time-dependent fluctuating value (about the mean value). Mathematically, it is expressed as (velocity u is used):

$$u(x,t) = \bar{u}(x) + u'(x,t), \tag{3.15}$$

where the mean velocity:

$$\bar{u}(x) = \lim_{T\to\infty} \frac{1}{T}\int_0^T u(x,t)dt, \tag{3.16}$$

where t is the time and T is the averaging interval. If T is large enough, ū does not depend on the time at which the averaging is started.

If the flow is unsteady, time averaging cannot be used and it must be replaced by ensemble averaging [14]:

$$\bar{u}(x,t) = \lim_{N\to\infty} \frac{1}{N} \sum_{n=1}^{N} u(x,t), \tag{3.17}$$

where N is the number of members of the ensemble and must be large enough to eliminate the effects of the fluctuations.

This type of averaging can be applied to any flow. The term Reynolds averaging is used to refer to any of these averaging processes; applying it to the Navier-Stokes equations yields the Reynolds-averaged Navier-Stokes (RANS) equations.

The time average of the mean velocity is again the same time-averaged value, while the time average of the fluctuating part of the velocity is zero. Thus, averaging any linear term in the conservation equations simply gives the identical term for the averaged quantity. From a quadratic nonlinear term, we get two terms, the product of the average and a covariance:

$$\overline{u_i u_j} = \overline{(\bar{u}_i + u_i')(\bar{u}_j + u_j')} = \bar{u}_i\bar{u}_j + \overline{u_i' u_j'} \tag{3.18}$$

The last term is zero only if the two quantities are uncorrelated; this is rarely the case in turbulent flows and, as a result, the conservation equations contain terms such as $\rho\overline{u_i' u_j'}$, called the Reynolds stresses, among others (e.g., $\rho\overline{u_i' \phi'}$ is known as the turbulent scalar flux, where ϕ is any conserved intensive property, like velocity v for momentum conservation). These cannot be represented uniquely in terms of the mean quantities.

The presence of the Reynolds stresses and turbulent scalar flux in the conservation equations means that the latter are not closed, that is to say, they contain more variables than there are equations. Closure requires use of some approximations, which usually take the form of prescribing the Reynolds stress tensor and turbulent scalar fluxes in terms of the mean quantities [14]. The approximations introduced are called turbulence models.

the Reynolds averaged equations of motion in conservation form for incompressible flows without body forces (continuity and momentum equations):

$$\frac{\partial(\rho\bar{u}_i)}{\partial x_i} = 0 \tag{3.19}$$

$$\frac{\partial(\rho\bar{u}_i)}{\partial t} + \frac{\partial}{\partial x_j}\left(\rho\bar{u}_i\bar{u}_j + \rho\overline{u_i' u_j'}\right) = -\frac{\partial\bar{p}}{\partial x_i} + \frac{\partial\bar{\tau}_{ij}}{\partial x_j}, \tag{3.20}$$

where $\bar{\tau}_{ij}$ are the mean viscous stress tensor components:

$$\bar{\tau}_{ij} = \mu\left(\frac{\partial\bar{u}_i}{\partial x_j} + \frac{\partial\bar{u}_j}{\partial x_i}\right) \tag{3.21}$$

Aside from replacement of instantaneous variables by mean values, the only difference between the time-averaged and instantaneous momentum equations is the appearance of the Reynolds stress tensor $-\rho\overline{u_i' u_j'}$.

3.4.2 Turbulence Models

Four main categories of turbulence models had evolved [21]:

1. Algebraic (Zero-Equation) Models: eddy-viscosity/mixing-length model, etc.
2. One-Equation Models: Bradshaw-Ferriss-Atwell model, Spalart and Allmaras model, etc. Such model equations can be solved easier numerically, relative to two-equation models and second-order closure models. Of the four types of turbulence models, the one-equation model has enjoyed the least popularity and success.
3. Two-Equation Models: k-ε model, k-ω model, and their modified versions.
4. Second-Order Closure Models: Launder, Reece and Rodi model, etc. However, because of the large number of equations and complexity involved in second-order closure models, they have thus far found their way into a relatively small number of applications compared to algebraic and two-equation models.

Turbulence models based upon the equation for the turbulence kinetic energy have become the cornerstone of modern turbulence modeling research. There are two types of turbulence energy equation models – one-equation models and two-equation models. These models both retain the Boussinesq eddy-viscosity approximation (the momentum transfer caused by turbulent eddies can be modeled with an eddy viscosity), but differ in one important respect. One-equation models are incomplete as they relate the turbulence length scale to some typical flow dimension. By contrast, two-equation models provide an equation for the turbulence length scale or its equivalent and are thus complete [21].

Two-equation models are most widely used. These models provide not only for computation of k, but also for the turbulence length scale or equivalent. Consequently, two-equation models are complete, i.e., can be used to predict properties of a given turbulent flow with no prior knowledge of the turbulence structure. They are, in fact, the simplest complete model of turbulence. By far, the most popular two-equation model is the k-ε model.

3.4.3 RNG k-ε Turbulence Model

In laminar flows, energy dissipation and transport of mass, momentum, and energy normal to the streamlines are mediated by the viscosity, so it is natural to assume that the effect of turbulence can be represented as an increased viscosity. This leads to the eddy-viscosity model for the Reynolds stress [14]:

$$-\rho\overline{u_i'u_j'} = \mu_t\left(\frac{\partial\bar{u}_i}{\partial x_j}+\frac{\partial\bar{u}_j}{\partial x_i}\right)-\frac{2}{3}\rho\sigma_{ij}k, \tag{3.22}$$

where μ_t – turbulent eddy viscosity, σ_{ij} – stress tensor, k – turbulent kinetic energy:

$$k = \frac{1}{2}\overline{u_i'u_i'} = \frac{1}{2}\left(\overline{u_x'u_x'}+\overline{u_y'u_y'}+\overline{u_z'u_z'}\right) \tag{3.23}$$

Although the eddy-viscosity hypothesis is not correct in detail, it is easy to implement and, with careful application, can provide reasonably good results for many flows.

The modeled version of the turbulence kinetic energy equation:

$$\begin{gathered}\frac{\partial(\rho k)}{\partial t}+\frac{\partial(\rho \bar{u}_j k)}{\partial x_j}=\frac{\partial}{\partial x_j}\left(\mu\frac{\partial k}{\partial x_j}\right)-\frac{\partial}{\partial x_j}\left(\frac{\rho}{2}\overline{u'_j u'_i u'_i}+\overline{p' u'_j}\right)\\ -\rho\overline{u'_i u'_j}\frac{\partial \bar{u}_i}{\partial x_j}-\mu\overline{\frac{\partial \bar{u}_i}{\partial x_k}\frac{\partial \bar{u}_i}{\partial x_k}}\end{gathered} \tag{3.24}$$

The terms on the left-hand side of this equation and the first term on the right-hand side need no modeling. The last term represents the product of the density ρ and the dissipation, ε, the rate at which turbulence energy is irreversibly converted into internal energy. For this reason, an equation for the dissipation is also necessary.

The second term on the right-hand side represents turbulent diffusion of kinetic energy (which is actually transport of velocity fluctuations by the fluctuations themselves). The third term of the right-hand side represents the rate of production of turbulent kinetic energy by the mean flow, a transfer of kinetic energy from the mean flow to the turbulence. As the right hand side of this equation can be calculated from quantities that will be computed, the development of the turbulent kinetic energy equation is complete [14]. For more details, refer to [14] and [21].

In formulating the k-ε model, the idea is to derive the exact equation for ε and to find suitable closure approximations for the exact equation governing its behavior. Although an exact equation for the dissipation can be derived from the Navier-Stokes equations, the modeling applied to it is so severe that it is best to regard the entire equation as a model. In its most commonly used form, this equation is:

$$\frac{\partial(\rho\varepsilon)}{\partial t}+\frac{\partial(\rho u_j \varepsilon)}{\partial x_j}=\frac{\partial}{\partial x_j}\left(\frac{\mu+\mu_t}{Pr_\varepsilon}\frac{\partial \varepsilon}{\partial x_j}\right)+C_{\varepsilon 3}\rho\varepsilon\frac{\partial u_i}{\partial x_i}+\frac{\varepsilon}{k}\left(C_{\varepsilon 1}\frac{\partial u_i}{\partial x_i}\tau_{ij}-C_{\varepsilon 2}\rho\varepsilon\right)-\rho R, \tag{3.25}$$

where μ – molecular viscosity, μ_t – turbulent eddy viscosity, Pr_ε – reciprocal ε Prandtl number, τ_{ij} – mean viscous stress tensor components [from Eq. (3.21)], $C_{\varepsilon 1}$, $C_{\varepsilon 2}$, $C_{\varepsilon 3}$ – model constants.

In this model, the eddy viscosity is expressed as:

$$\mu_t=\rho C_\mu\sqrt{k}L=\rho C_\mu\frac{k^2}{\varepsilon}, \tag{3.26}$$

where C_μ is a model constant, L – turbulence length scale.

Neglecting R in Eq. (3.25) the standard k-ε model is obtained. If R is considered, the model is called RNG k-ε.

The RNG model was developed using Re-Normalization Group (RNG) methods to renormalize the Navier-Stokes equations, to account for the effects of smaller scales of motion. In the standard k- ε model the eddy viscosity is determined from a single turbulence length scale, so the calculated turbulent diffusion is that which occurs only at the specified scale, whereas in reality all scales of motion will contribute to it. The RNG approach results in a modified form of the ε equation which attempts to account for the different scales of motion through changes to the production term [22].

For the RNG k-ε model, R in Eq. (3.25) [23]:

$$R = \frac{C_\mu \eta^3 \left(1 - \frac{\eta}{\eta_0}\right)}{1 + \beta \eta^3} \frac{\varepsilon^2}{k}, \tag{3.27}$$

where β – constant, while η and η_0 are defined by Eqs. (3.28) and (3.29) respectively.

$$\eta = \frac{k}{\varepsilon} \sqrt{2 S_{ij} S_{ij}}, \tag{3.28}$$

where $S_{ij} = \frac{1}{2}\left(\frac{\partial \bar{u}_i}{\partial x_j} + \frac{\partial \bar{u}_j}{\partial x_i}\right)$ – mean strain.

$$\eta_0 = \left[\frac{C_{\varepsilon 2} - 1}{C_\mu (C_{\varepsilon 1} - 1)}\right]^{\frac{1}{2}} \tag{3.29}$$

Finally, constants used for RNG k-ε model are given in Table 3.1 [24]:

Table 3.1 RNG k-ε model constants

Model constant	Value
$C_{\varepsilon 1}$	1.42
$C_{\varepsilon 2}$	1.68
$C_{\varepsilon 3}$	-1.0
C_μ	0.0845
Pr_ε	1.39
β	0.012
η_0	4.38

RNG k-ε model is recommended for internal combustion engines applications by CONVERGE CFD.

4 CONVERGE CFD Software

CONVERGE CFD software is a product of Convergent Science, which was founded in 1997 by graduate students at the University of Wisconsin-Madison. Convergent Science was a CFD consulting company in its early years. In 2008, the first CONVERGE licenses were sold and the company transitioned to a CFD software company [25].

CONVERGE software is an advanced CFD tool, especially suited to IC engines simulations. It offers autonomous meshing: the software automatically creates the mesh at runtime, dynamically adapts the mesh throughout the simulation, and invokes Adaptive Mesh Refinement to maximize both accuracy and computational efficiency.

Moreover, CONVERGE software contains a wide variety of modeling options for combustion, emissions, spray and turbulence.

4.1 Discretization Method

CONVERGE uses the finite volume method, briefly described in Section 3.3.2, to solve numerically the integral form of the conservation equations.

An advantage of the finite volume method is that it conserves transported quantities for regularly or irregularly shaped cells. The integral form of the equation is solved by summing fluxes on the faces of the cells. In CONVERGE, all values are collocated and stored at the center of the cell, as shown in Figure 4-1 [24].

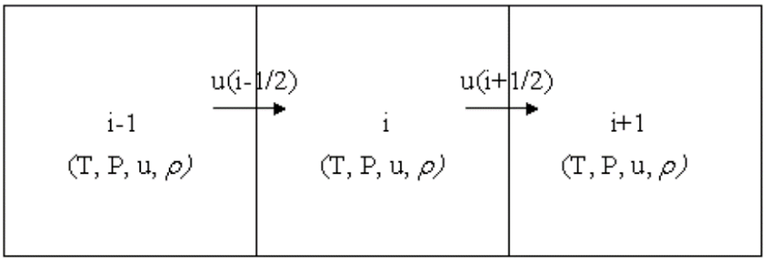

Figure 4-1 Sample three-cell, one-dimensional spatial domain [24]

To solve the integral form of the equation, values must be interpolated to the cell surface. There are several options for obtaining the cell surface value. One option is to average the two adjacent cell values and place them on the surface:

$$\phi_{i\pm\frac{1}{2}} = \frac{1}{2}\phi_i + \frac{1}{2}\phi_{i\pm1} \tag{4.1}$$

Another option is to upwind the surface value:

$$\phi_{i+\frac{1}{2}} = \phi_i \text{ and } \phi_{i-\frac{1}{2}} = \phi_{i-1} \tag{4.2}$$

There is also a possibility to use a blended scheme, where the surface value would be between that of evenly interpolated [Eq. (4.1)], and that of entirely upwinded [Eq. (4.2)].

4.2 Solution Procedure and Solver

The order in which the governing (or transport) equations are solved in CONVERGE is summarized in Figure 4-2.

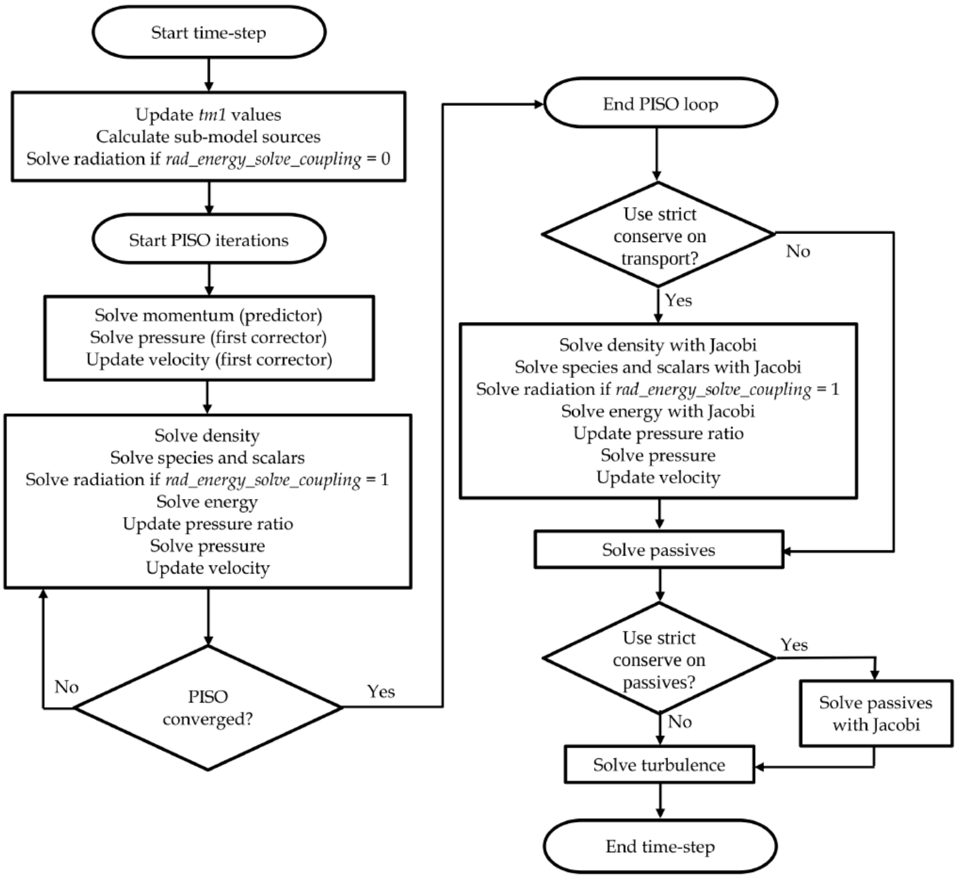

Figure 4-2 Solution order of the transport equations [24]

At the start of each time-step, the previous values [the time-step minus 1 (*tm1* in Figure 4-2)] are stored for all transported quantities. Next, explicit sources are calculated for each sub-model that is currently activated and radiation is solved if energy and radiation are decoupled. At the beginning of the PISO loop (i.e., the first PISO iteration), CONVERGE solves for momentum and pressure, which sets the velocity for the other transport equations. After each PISO iteration, it is necessary to check for PISO loop convergence. For compressible cases, CONVERGE considers the PISO loop to be converged if [24]:

$$\Delta\rho < piso\_tol, \tag{4.3}$$

where $\Delta\rho$ – density correction error, $piso\_tol$ – PISO tolerance.

For incompressible cases, CONVERGE considers the PISO loop to be converged if:

$$\Delta P < piso\_tol, \tag{4.4}$$

where ΔP – pressure correction error.

If the PISO iteration has converged but the PISO iteration number is less than *piso_itmin* (which can be user defined), the PISO iterations will continue until the minimum number of PISO iterations has been exceeded. If the PISO iteration did not converge, CONVERGE executes an additional PISO iteration.

After the PISO loop has ended, CONVERGE may perform an additional Jacobi iteration to enforce strict conservation. The Jacobi iteration guarantees that the quantity is conserved to machine zero, rather than to the tolerance set by *piso_tol*.

The turbulence equations are outside of the PISO loop for efficiency reasons.

4.2.1 PISO Algorithm

The pressure-velocity coupling in CONVERGE is achieved using a modified Pressure Implicit with Splitting of Operators (PISO) method, thoroughly explained in [26]. PISO is described as a non-iterative method for handling the coupling of the implicitly discretized time-dependent fluid flow equations.

The method is based on the use of pressure and velocity as dependent variables and is hence applicable to both the compressible and incompressible versions of the transport equations. The main feature of the technique is the splitting of the solution process into a series of steps whereby operations on pressure are decoupled from those on velocity at each step, with the split sets of equations being amenable to solution by standard techniques. At each time-step, the procedure yields solutions which approximate the exact solution of the difference equations [26].

The PISO algorithm as implemented in CONVERGE starts with a predictor step where the momentum equation is solved. After the predictor, a pressure equation is derived and solved, which leads to a correction applied to the momentum equation.

This process of correcting the momentum equation and re-solving can be repeated as many times as necessary to achieve the desired accuracy. After the momentum predictor and first corrector step have been completed, the other transport equations are solved in series [24].

In order to limit the PISO corrections, the minimum and maximum number of PISO corrections allowed can be entered. If the maximum number of PISO iterations is exceeded and the solution has not converged, the following time-step will be reduced.

4.3 Mesh Generation

CONVERGE discretizes the domain into control volumes called nodes or cells (terms “node” and “cell” are used interchangeably). Each node is defined by its center and the faces that bound the node. The software uses internal data structures to define the domain(s) of the mesh, assign an order to nodes and the faces of the node, and establish connectivity between nodes.

CONVERGE has an innovative approach to grid generation – it automatically generates the grid at runtime. To make this possible, the software uses a modified cut-cell Cartesian grid generation method. The geometry surface is immersed within a Cartesian block. Cells are trimmed at the intersecting surface, after which the intersection information (surface areas, normal vectors, etc.) is reduced before being stored for each cell. This allows for complex surface intersections to be represented more easily. Cut-cell is shown in Figure 4-3a.

A slave node is a cut-cell whose volume is less than 30% of the master node volume. In a process called cell pairing, CONVERGE pairs the master and slave nodes to form a single node, which is known as a paired node. The center of the paired node is at the volumetric center of the combined nodes. The master node and the slave node share values of transport entities [24]. Master and slave nodes ae shown in Figure 4-3b.

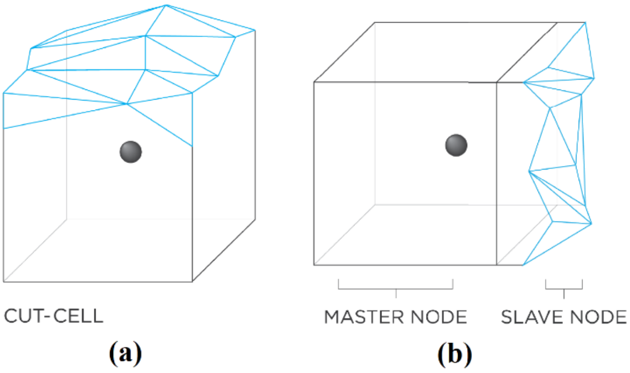

Figure 4-3 Visualization of the cut-cell method in CONVERGE [27]

All nodes are transport nodes (Figure 4-4a). CONVERGE solves transport entities such as velocity, temperature, and species at the center of a transport node. A parcel cell (also known as a parcel), shown in Figure 4-4b, is a theoretical representation of spray drops that are identical to one another (i.e., the drops have the same radii, temperature, and other properties). A parcel is used to statistically represent the discrete phase of all of the drops in that parcel [27].

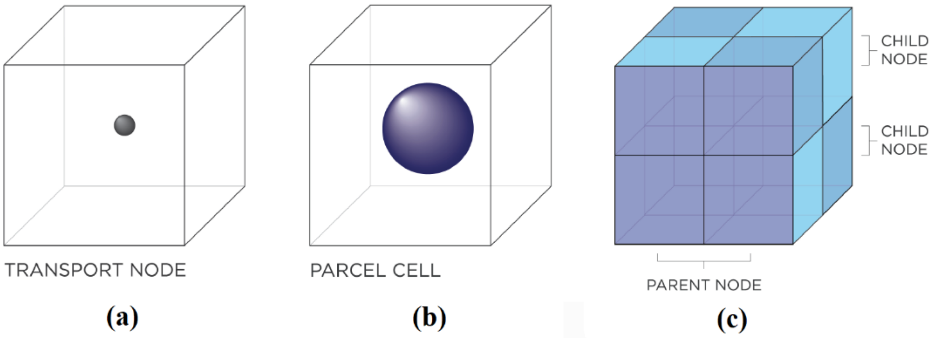

Figure 4-4 Types of cells in CONVERGE [27]

Automatic grid generation involves moving the surface to the proper location (if the geometry includes moving components), trimming the boundary cells, refining any embedding areas, and then removing the refinement from the embedding. For stationary geometries, CONVERGE performs this process once at the start of the simulation and again whenever the geometry is refined or coarsened. For moving geometries, the grid generation process at each time-step is performed.

CONVERGE includes several tools for controlling the grid size before and during a simulation. Grid scaling coarsens or refines the base grid size. Fixed embedding refines the grid at specified locations and times. Adaptive Mesh Refinement (AMR) automatically changes the grid based on fluctuating and moving conditions.

CONVERGE employs an octree data structure for grid refinement. During a grid refinement process (fixed embedding or Adaptive Mesh Refinement), a parent transport node is subdivided into eight (or multiples of eight) child nodes (Figure 4-4c).

4.3.1 Grid Scaling

Grid scaling refers to changing the base grid size at specified times during a simulation. Grid scaling can greatly reduce runtimes by coarsening the grid during non-critical simulation times and can help capture critical flow phenomena by refining the grid at other times [24].

The base grid size $\mathrm{dx}_{\mathrm{base}}$ is changed according to:

$$dx\_scaled = \frac{dx\_base}{2^{grid\_scale}}, \tag{4.5}$$

where *dx_scaled* – scaled grid size, *grid_scale* – scaling factor.

A *grid_scale* value of 0 will leave the base cells unchanged, a negative value will coarsen the base grid, and a positive value will refine the base grid.

4.3.2 Fixed Embedding

Fixed embedding can be used to refine the grid at specific locations in the domain where a finer resolution is critical to the accuracy of the solution. For example, when simulating sprays, an area of fixed embedding can be added by the nozzle to resolve the complex flow behavior. Fixed embedding allows the rest of the grid to remain coarse to minimize simulation time [24].

For each fixed embedding, an embedding scale (*embed_scale*), that indicates how CONVERGE will refine the grid in that location, has to be defined. It must be a positive integer, and scales the base grid sizes (*dx_base*, *dy_base*, and *dz_base*) according to:

$$dx\_embed = \frac{dx\_base}{2^{embed\_scale}} \tag{4.6}$$

A specific time period for each fixed embedding can be specified, which can further reduce the computational time by refining the grid only for a portion of the simulation. Also, there are several specific types of fixed embedding:

1. Boundary embedding: provides finer grid near boundaries. For example, surfaces defining a combustion chamber (cylinder head, piston crown, liners) can be embedded to enable more accurate heat transfer simulation (see Figure 4-5 on the right), or when simulating flow around a valve, extra resolution near the valve surface is useful to more accurately model the flow in this section of the domain.
2. Sphere embedding: a spherical area is embedded.
3. Cylinder embedding: a cylindrical or truncated conical area is embedded.
4. Nozzle and injector embedding: a conical area is embedded around a nozzle (nozzle embedding), or a conical area is embedded around all nozzles of an injector (injector embedding). This type of embedding is especially useful to accurate modeling of sprays. Example of the nozzle embedding is shown in Figure 4-5.
5. Box embedding: an area confined in a “box” is embedded.
6. Region embedding: the entire region of a domain is embedded. For example, the region embedding can be used to refine the grid in the cylinder of an engine.

Figure 4-5 shows an example of nozzle embedding: on the left the cone representing the area to be embedded is visible, while on the right the mesh in a plane along the axis of the cone is demonstrated with fixed embedding active (shortly before start of injection, SOI).

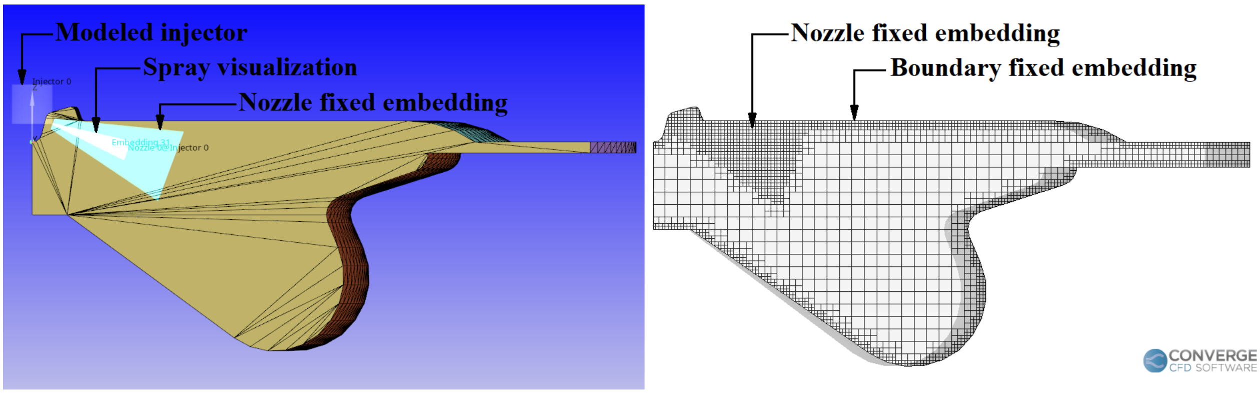

Figure 4-5 Visualization of nozzle and boundary fixed embedding application

4.3.3 Adaptive Mesh Refinement

Adaptive Mesh Refinement (AMR) automatically refines the grid based on fluctuating and moving conditions such as temperature or velocity. This option is useful for using a highly refined grid to accurately simulate complex phenomena such as flame propagation or high-velocity flow without unnecessarily slowing the simulation with a globally refined grid.

Ideally, a good AMR algorithm will add higher grid resolution (embedding) where the flow field is most under-resolved or where the sub-grid field is the largest (i.e., where the gradient of a specified field variable is the highest). The AMR method in CONVERGE estimates the magnitude of the sub-grid field to determine where embedding will be added [24].

For a scalar, the sub-grid field is defined as the difference between the actual field and the resolved field:

$$\phi' = \phi - \overline{\phi}, \tag{4.7}$$

where ϕ is the actual scalar field, $\overline{\phi}$ is the resolved scalar field, and ϕ' is the sub-grid scalar field.

The sub-grid for any scalar can be expressed as an infinite series, however it is not possible to evaluate the entire series, and only the first term (the second-order term) in the series is used to approximate the scale of the sub-grid:

$$\phi' \cong -\alpha_{[k]} \frac{\partial^2 \overline{\phi}}{\partial x_k \, \partial x_k}, \tag{4.8}$$

where $\alpha_{[k]} = \frac{dx_k^2}{24}$ for a rectangular cell.

This equation can be easily generalized for a vector field, such as velocity. A cell is embedded if the absolute value of the sub-grid field is above a user-specified value. Conversely, a cell is released (i.e., the embedding is removed) if the absolute value of the sub-grid is below 1/5 of the user-specified value.

AMR can be enabled for any or as many of the following fields: velocity, number of parcels per cell, temperature, void fraction, species, passives, or boundary (y+). AMR can be specified with a different embedding scale and different sub-grid criterion for each condition. In addition to the field control, the time when the AMR will start and when it will end can be specified for each field, similar to fixed embedding timing control [24].

Example of AMR is given in Figure 4-6, where AMR for temperature, velocity and species is applied (level of embedding is 2). Comparing to the right view of Figure 4-5, extension of AMR during diesel spray combustion (at 11° ATDC) can be appreciated.

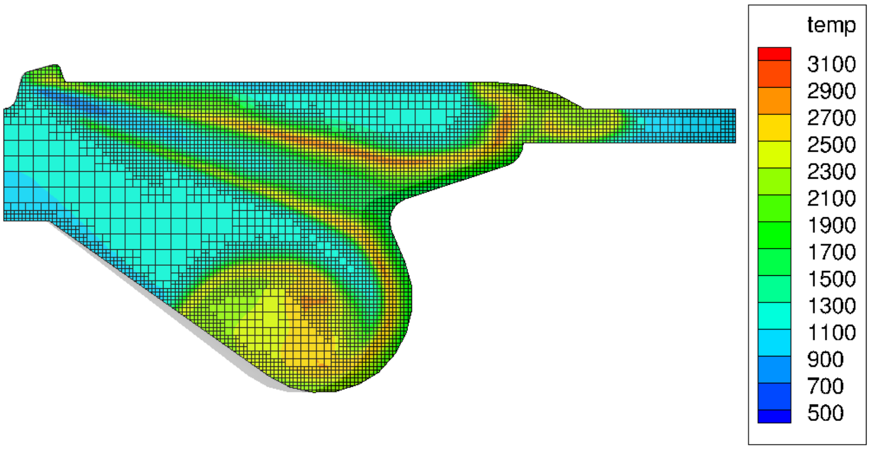

Figure 4-6 Visualization of Adaptive Mesh Refinement during diesel spray combustion

4.3.4 Adaptive Collision Mesh

It is well known that collision calculations (see Section 4.6.5) can be highly grid-sensitive when an under-resolved fluid-phase mesh is used. To help alleviate this issue, an adaptive collision mesh option has been implemented in CONVERGE.

In a simulation without collision mesh, parcels collide only with parcels in the same grid cell. This can lead to artifacts in the spray, since parcels do not collide across cell walls. This can also slow down computational time because there can be many parcels in larger cells. Using a collision mesh can eliminate both these problems. Simulations with collision mesh can much more accurately represent the spray dispersion by eliminating grid effects. However, the caution should be used when decreasing the collision mesh cell size: parcels can pass right through a collision mesh cell without having the chance to collide if the collision mesh to too refined.

The collision mesh is a uniform grid, used only for parcel collision, that rotates about a random axis at every time-step. The embed level of the collision mesh (set by the *coll_scale* parameter) is the number of levels below the base mesh size. Eq. (4.6) can be used to calculate the new grid size.

This mesh is completely independent of the fluid-phase mesh and is used only for collision calculations. The algorithm for creating the collision mesh is based on randomly selecting a coordinate system and creating a collision mesh at each time-step. Once the mesh is created, the parcels are placed in the appropriate collision mesh cell and the collision calculation proceeds as usual [24].

4.4 Combustion Modeling

CONVERGE contains the SAGE detailed chemical kinetics solver, presented in [28], which models detailed chemical kinetics via a set of CHEMKIN-formatted input files.

A chemical reaction mechanism is a set of elementary reactions that describe an overall chemical reaction. The combustion of different fuels can be modeled by changing the mechanism. SAGE calculates the reaction rates for each elementary reaction while the CFD solver solves the transport equations. Given an accurate mechanism, SAGE (in addition to AMR) can be used for modeling many combustion regimes (ignition, premixed, mixing controlled) [24].

As described by Turns [29], a multi-step chemical reaction mechanism can be written in the form:

$$\sum_{m=1}^{M} \nu'_{m,r}\chi_m \leftrightarrow \sum_{m=1}^{M} \nu''_{m,r}\chi_m, \qquad \text{for } r = 1, 2, \dots, R \tag{4.9}$$

where $\nu'_{m,r}$ and $\nu''_{m,r}$ are the stoichiometric coefficients for the reactants and products, respectively, for species m and reaction r; R is the total number of reactions, and χ_m is the chemical symbol for species m.

The net production rate of species m is given by:

$$\dot{\omega}_m = \sum_{r=1}^{R} \nu_{m,r} q_r, \qquad \text{for } m = 1, 2, \dots, M \tag{4.10}$$

where M is the total number of species, and $\nu_{m,r}$:

$$\nu_{m,r} = \nu''_{m,r} - \nu'_{m,r} \tag{4.11}$$

The rate-of-progress variable q_r for the r-th reaction is:

$$q_r = k_{fr} \prod_{m=1}^{M} [X_m]^{\nu'_{m,r}} - k_{rr} \prod_{m=1}^{M} [X_m]^{\nu''_{m,r}}, \tag{4.12}$$

where $[X_m]$ is the molar concentration of species m, k_{fr} and k_{rr} are the forward and reverse rate coefficients for reaction r.

In SAGE, the forward rate coefficient is expressed by the Arrhenius form:

$$k_{fr} = A_r T^{b_r} e^{\left(-\frac{E_r}{R_u T}\right)}, \tag{4.13}$$

where A_r is the pre-exponential factor, b_r is the temperature exponent, E_r is the activation energy, and R_u is the universal gas constant.

In addition, the reverse rate coefficient can either be specified in an analogous fashion as Eq. (4.13), or calculated from the equilibrium coefficient K_{cr} as:

$$k_{rr} = \frac{k_{fr}}{K_{cr}}, \tag{4.14}$$

where the equilibrium coefficient K_{cr} is determined from the thermodynamic properties and is given by:

$$K_{cr} = K_{pr} \left(\frac{p_{atm}}{RT}\right)^{\sum_{m=1}^{M} \nu_{m,r}}, \tag{4.15}$$

where p_{atm} is the atmospheric pressure, R is the gas constant, and T is the temperature. The equilibrium constant K_{pr} is obtained via:

$$K_{pr} = \exp\left(\frac{\Delta S_r^0}{R} - \frac{\Delta H_r^0}{RT}\right), \tag{4.16}$$

where Δ refers to the change that occurs in passing completely from reactants to products in the r-th reaction, specifically:

$$\frac{\Delta S_r^0}{R} = \sum_{m=1}^{M} \nu_{m,r} \frac{S_m^0}{R} \tag{4.17}$$

and

$$\frac{\Delta H_r^0}{RT} = \sum_{m=1}^{M} \nu_{m,r} \frac{H_m^0}{R}, \tag{4.18}$$

where S and H denote entropy and enthalpy, respectively.

With the above information, the governing equations for mass and energy conservation can be solved for a given computational cell. The governing equation for mass and energy are, respectively:

$$\frac{d[X_m]}{dt} = \dot{\omega}_m \tag{4.19}$$

and

$$\frac{dT}{dt} = \frac{V\frac{dp}{dt} - \sum_m\left(\bar{h}_m \dot{\omega}_m\right)}{\sum_m\left([X_m]\bar{c}_{p,m}\right)}, \tag{4.20}$$

where V is volume, T is temperature, p is pressure, $\dot{\omega}_m$ is determined by Eq. (4.10), and $\bar{h}_m$ and $\bar{c}_{p,m}$ are the molar specific enthalpy and molar constant-pressure specific heat of species m, respectively.

Eq. (4.20) is for constant-volume combustion. The above equations are solved at each computational time-step and the species are updated appropriately. It is important to note that the temperature obtained from Eq. (4.20) is used to update only the rate coefficients as SAGE is solving the system of rate equations and is not used to update the CONVERGE cell temperature. The cell temperature is updated after the detailed chemistry calculation has converged using the computed species concentrations.

In order to expedite the detailed chemistry calculations, kinetics is not solved in cells that fall below a minimum cell temperature (T_{cut}) and a minimum mole fraction (HC_{min}). The minimum mole fraction is the total mole fraction of CO, H2, and the hydrocarbon species. The minimum mole fraction includes more than just the hydrocarbon species to allow carbon monoxide chemistry to take place in computational cells that do not include hydrocarbon species [24].

4.5 Emissions Modeling

CONVERGE contains several models to simulate soot and NOx production. In this work, detailed soot model – Particulate Mimic (PM) – is described, while NOx is calculated via the SAGE detailed chemistry solver, already described in Section 4.4.

4.5.1 Particulate Mimic (PM) Soot Model

The soot model describes the complex soot formation and oxidation process using several global steps, including soot inception, surface growth, coagulation, and oxidation [24]:

1. Soot inception is the formation of the smallest solid soot particles from the gas-phase hydrocarbon molecules [e.g., PAH (polycyclic aromatic hydrocarbons) species]. Inception serves as the link between gas-phase chemistry and soot particle dynamics, and can be described by the collision of two PAH molecules.
2. Soot surface growth is necessary to accomplish two-way coupling with the gas phase. Soot mass growth and heterogeneous reactions on surfaces as well as loss of soot particles due to reactions with gas phase species must be included in a detailed presentation of soot formation.
3. Soot coagulation is a physical process of collisions between small soot particles leading to the formation of larger soot particles.
4. Soot condensation is when the gas phase species (such as PAHs) coagulate together and form large soot particles.

Figure 4-7 describes the various steps of soot formation. The reaction rates of these global steps are determined by implementing simplified physical models. The soot models implemented in CONVERGE typically are solved with detailed PAH chemistry.

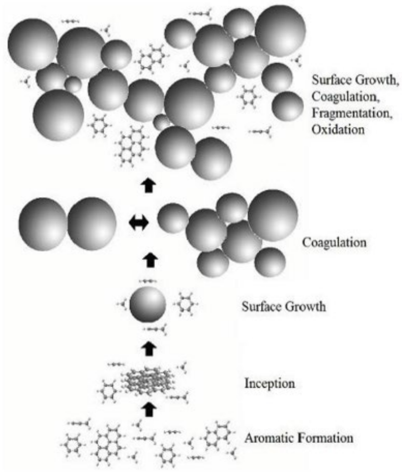

Figure 4-7 Descriptive overview of soot formation [24]

Detailed soot models apply comprehensive mathematical description for the soot particle size distribution function (PSDF) and solve the complex soot formation and oxidation with detailed chemistry. Detailed soot models feature good capability over wide ranges of operating conditions.

The properties of a soot ensemble can be described by the particle size distribution function (PSDF). The PSDF of soot can be obtained by solving equations for the number density of all size classes, based on the condition that the different physical and chemical processes changing the PSDF are known. This results in an infinite set of partial differential equations. Therefore, the size of the problem must be reduced using certain mathematical methods.

The method of moments is based on the fact that solving an infinite set of equations for the statistical moments of the PSDF is equivalent to the direct simulations of the PSDF. This method can be shown to have sufficient accuracy using only a few moments for global observables, such as mean number density and soot mass. Usually a set of equations for the first two to six moments is applied. The accuracy of the approach increases with the number of moments used.

The main advantages of the method of moments is its computational efficiency and that the major features of the PSDF, such as mean number density and soot volume fraction, can be extracted from the moments. The Particulate Mimic (PM) model in CONVERGE is based on the method of moments introduced above [24].

The basic physical and chemical processes assumed to be important for the formation of soot are: particle inception, coagulation, condensation, and heterogeneous surface reactions, i.e., surface growth and oxidation by OH and O2. The dynamics of the soot particle characteristics can be described by a set of equations for the moments of the soot particle size distribution function:

$$\frac{\mathrm{dM_r}}{\mathrm{dt}} = \dot{\mathrm{M}}_{\mathrm{r,pi}} + \dot{\mathrm{M}}_{\mathrm{r,con}} + \dot{\mathrm{M}}_{\mathrm{r,coag}} + \dot{\mathrm{M}}_{\mathrm{r,sr}}, \tag{4.21}$$

where $\dot{\mathrm{M}}_{\mathrm{r,pi}}$, $\dot{\mathrm{M}}_{\mathrm{r,con}}$, $\dot{\mathrm{M}}_{\mathrm{r,coag}}$ and $\dot{\mathrm{M}}_{\mathrm{r,sr}}$ are the rates of particle inception, condensation, coagulation, and surface reactions for the r-th moment of the PSDF, respectively.

The moments are defined as:

$$\mathrm{M_r} = \sum_{\mathrm{i}=1}^{\infty} \mathrm{i^r N_i}, \tag{4.22}$$

where N_i is the number density of soot particles of size class i.

It can be seen from the definition that the zero-th moment is related to the mean number density, whereas the first moment is related to the mean mass or mean volume of the soot particles.

Each moment in the particulate mimic model is solved as global transport passive:

$$\frac{D\left(\frac{\dot{M}_r}{\rho}\right)}{Dt} = \nabla\left(\frac{\mu}{Sc}\nabla\left(\frac{\dot{M}_r}{\rho}\right)\right) + \dot{S}_{Mr}, \tag{4.23}$$

where Sc is the Schmidt number, and $\dot{S}_{Mr}$ represents the source term:

$$\dot{S}_{Mr} = \dot{M}_{r,pi} + \dot{M}_{r,con} + \dot{M}_{r,coag} + \dot{M}_{r,sg} + \dot{M}_{r,ox}, \tag{4.24}$$

where $\dot{M}_{r,sg}$ and $\dot{M}_{r,ox}$, are the rates of surface growth and oxidation by OH and O2, respectively. Sum of these two terms is $\dot{M}_{r,sr}$, which appeared in Eq. (4.21).

The moment source term is coupled with species source term and solved using SAGE solver. It is a two-way coupling, which means that the soot formation will affect the gas phase and system heat release.

Stages of the PM model, including soot inception, surface reactions, coagulation and condensation are described in [24].

4.6 Spray Modeling

To calculate the spray in a simulation, drop parcels are introduced into the domain at the injector location at a user-specified rate. Parcels represent a group of identical drops (i.e., same radius, velocity, temperature, etc.) and are used to statistically represent the entire spray field. By using the concept of drop parcels, CONVERGE significantly reduces the computational time of a simulation involving spray.

Spray droplets are subject to several processes from the time of injection until the time of vaporization: breakup, collision and coalescence, turbulent dispersion. Droplets are also affected by characteristics of a nozzle.

4.6.1 Nozzle Discharge Coefficient

Contraction effects of nozzles are accounted in each injector, depending on the user inputs for discharge coefficient, nozzle diameter, liquid density, injection rate-shape, injected mass and injection duration. The contraction coefficient, C_a, of a nozzle is given as:

$$C_a = \frac{C_d}{C_v}, \tag{4.25}$$

where C_d – nozzle discharge coefficient, C_v – velocity coefficient, which is dynamically calculated based on the injection pressure at that time.

The area contraction coefficient accounts for cavitation or hydraulic flip effects which can lead to a reduced flow area at the nozzle exit [28]. The effective diameter of the nozzle is reduced with reducing of the contraction coefficient:

$$\mathrm{d_{eff}} = \sqrt{\mathrm{C_a}}\,\mathrm{d_{geom}}, \tag{4.26}$$

where $\mathrm{d_{geom}}$ is the geometrical nozzle diameter.

As the effective area of the nozzle is reduced, the initial parcel size is reduced (see Section 4.6.2) and the drop velocity magnitude is increased proportionally. The injection pressure is then:

$$\mathrm{P_{inj}} = \frac{1}{2}\rho_\mathrm{l}\left(\frac{\mathrm{V}}{\mathrm{C_d}}\right)^2, \tag{4.27}$$

where ρ_l is the liquid density, and V is the liquid velocity based on the geometric hole diameter (i.e., the velocity before a contraction coefficient is applied).

From Eq. (4.27) it is evident that correct description of the nozzle discharge coefficient is important to correctly predict the quantity of premixed phase of diesel combustion, as it is directly affected by injection pressure (as explained in Section 2.5.1).

4.6.2 Injection Size Distribution

Four injection size distributions are available in CONVERGE: blob, chi squared, Rosin-Rammler, and constant injected radius. Blob model is based on the size of a nozzle, while other three methods depend on the Sauter mean diameter (SMD), which has to be specified by the user.

Blob is described as discrete parcel of drops, which has the same diameter as nozzle exit diameter (or effective nozzle diameter). This blob injection method of prescribing atomization differs from those other three, which assume that the liquid is already finely atomized at the nozzle exit with an initial distribution of drop sizes at the nozzle assumed with the SMD. The assumption of immediate atomization at the nozzle exit does not account for the presence of a core within a high-pressure spray [30]. It is known that there is an “intact core” of largely unbroken liquid which can extend for hundreds of nozzle diameters (see Section 2.2).

A core region is predicted with the blob injection method. This is because the injected blobs breakup due to interaction with the surrounding gas as they penetrate, yielding a region of relatively large drops near the nozzle [30]. Schematic showing the conceptual liquid flow structure at the nozzle exit for diesel-type sprays is given in Figure 4-8.

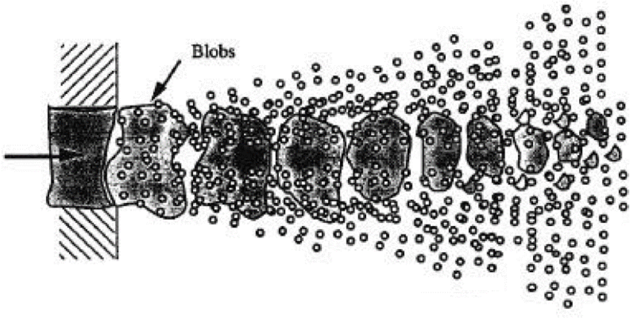

Figure 4-8 Schematic of the conceptual liquid flow structure at the nozzle exit [31]

4.6.3 Drop Drag

Accurate determination of drop drag coefficients is critical for accurate spray modeling. CONVERGE includes two models for drop drag (in addition to the option of no drag). The first model calculates the drag coefficient with the assumption that the drops are perfect spheres. The second model, called the dynamic drag model, determines the droplet drag coefficient dynamically, accounting for variations in the drop shape through a drop distortion parameter y. Values of the drop distortion parameter are determined from the Taylor Analogy Breakup (TAB) model, detail description of which is given in [24].

As an initially spherical droplet moves through a gas, its shape will distort significantly when the Weber number (a dimensionless parameter defined as the ratio of aerodynamic forces to surface tension forces) is large. In the extreme case, the drop shape will approach that of a disk. The drag on a disk is significantly higher than that of a sphere. Since the drop drag coefficient is highly dependent on the drop shape, a drag model that assumes the drop is spherical can under-predict drag. The dynamic drag model accounts for the effects of drop distortion by linearly varying the drag between that of a sphere, and a value corresponding to a disk [24].

The drag coefficient is given by:

$$\mathrm{C_D} = \mathrm{C_{D,sphere}}(1 + 2.632\mathrm{y}), \tag{4.28}$$

where y is the drop distortion parameter, as determined from the TAB model.

4.6.4 Spray Breakup

CONVERGE includes several spray breakup mechanisms, including models based on the Kelvin-Helmholtz (KH) and Rayleigh-Taylor (RT) instability mechanisms, the Taylor Analogy Breakup (TAB) drop breakup model, and the LISA (Linearized Instability Sheet Atomization) sheet breakup model.

The TAB model is best for low Weber-number sprays. It does not provide reasonable predictions for the characteristics of high-pressure sprays and simulated engine performance and emissions. TAB based models has been found to predict a quite small premixed combustion phase and a large diffusive combustion phase due to their over prediction of droplet breakup [32].

The LISA model is used to model liquid sheet breakup. The model includes two parts – a general liquid sheet breakup mechanism and a liquid injection methodology specifically for pressure-swirl atomizers. The pressure-swirl atomizers are widely used for liquid-fuel combustion in gas turbines, oil furnaces, and direct-injection spark-ignition automobile engines.

Finally, spray breakup models based on both Kelvin-Helmholtz (KH) and Rayleigh-Taylor (RT) instability are usually used together in a combined model, KH-RT. A version of it, called the modified KH-RT breakup model, has been found to be especially accurate in engine simulations [32]. This model is also available in CONVERGE and has been used in this thesis.

Kelvin-Helmholtz (KH) Breakup Model

The Kelvin-Helmholtz instability is based on a liquid jet stability analysis that is described in detail in [33]. The analysis considers the stability of a cylindrical, viscous, liquid jet of radius $\mathrm{r_0}$ issuing from a circular orifice at a velocity U into a stagnant, incompressible, inviscid gas of density ρ_g. The liquid has a density ρ_l and viscosity μ_l, and a cylindrical polar coordinate system is used which moves with the jet [24].

In the KH model, the initial parcel diameters are set equal to the nozzle hole effective diameter d_o (or d_{eff}) and the atomization process of the relatively large injected blobs is modeled using the stability analysis for liquid jets. The breakup of the parcels and resulting drops is calculated by assuming that the breakup drop radius r_c is proportional to the wavelength of the fastest growing unstable surface wave Λ_{KH}:

$$r_c = B_0 \Lambda_{KH}, \tag{4.29}$$

where B_0 is a model constant typically set to 0.61. However, it can be adjusted if necessary. A smaller value will result in smaller drops from breakup.

The rate of change of drop radius in a parent parcel is given by:

$$\frac{dr_p}{dt} = -\frac{(r_p - r_c)}{\tau_{KH}}, \qquad r_c \leq r_p \tag{4.30}$$

where the breakup time τ_{KH}:

$$\tau_{KH} = \frac{3.726 B_1 r_p}{\Lambda_{KH} \Omega_{KH}}, \tag{4.31}$$

where Ω_{KH} is the maximum growth rate (or most unstable wave), and B_1 is the breakup time constant. B_1 is related to the initial disturbance level on the liquid jet and has been found to vary from one injector to another [34]. This constant accounts for differences in the drop breakup time due to unknown initial conditions for the drop. The influence on B_1 should be related to upstream conditions in the nozzle, turbulence inside the injector, and cavitation at high injection pressures, for example. This constant has been set as low as 1.73, based on comparisons to the TAB model, and as high as 60 for some calculations [35]. Small values of B_1 result in faster breakup. In this work B_1 is set to 7.

The KH model can be run with or without the creation of new child parcels. When droplet breakup occurs, pieces of the original droplet fragment away. CONVERGE considers these fragmented masses of liquid to be child parcels when they accumulate a sufficient amount of mass. When the mass of the fragmented liquid exceeds the cutoff value, CONVERGE creates a child parcel with a drop size of radius r_c [24].

When breakup occurs and it is determined that child droplets should be added to the computation, they are given a velocity component normal to the path of the parent drop. This normal velocity is determined by:

$$V_n = C_1 \Lambda_{KH} \Omega_{KH}, \tag{4.32}$$

where C_1 is a model velocity constant typically set to 0.188.

Rayleigh-Taylor (RT) Breakup Model

In addition to the KH breakup mechanism, the Rayleigh-Taylor (RT) instability is also believed to be responsible for droplet breakup. The unstable RT waves are thought to occur due to the rapid deceleration of the drops from the magnitude of the drag force, $|F_{D,i}|$:

$$|F_{D,i}| = m_d|a_i| = m_d \frac{3}{8} C_D \frac{\rho_g |U_i|^2}{\rho_l r_0}, \tag{4.33}$$

where m_d is the mass of the drop, a_i is the deceleration of the drop, C_D is the drag coefficient, U_i is the velocity of the drop, ρ_g and ρ_l are densities of gas and liquid, respectively.

Typical implementations of the RT breakup model ignore both gas and liquid viscosity. CONVERGE spray models extend the standard RT model to include viscosity, which can have a large effect for the high decelerations typical of spray droplets. Description of calculation steps for the fastest growing wavelength, Λ_{RT}, and the corresponding growth rate, Ω_{RT}, are given in [24].

If the scaled wavelength given by $C_{RT}\Lambda_{RT}$ is calculated to be smaller than the droplet diameter, RT waves are assumed to be growing on the surface of the drop. When the RT waves have been growing for a sufficient time (i.e., for the RT liquid breakup time $\tau_{RT} = C_I/\Omega_{RT}$, where C_I is a constant), the drop is broken up according to the RT mechanism. Note that the RT model size constant C_{RT} can be increased or decreased to change the size of the predicted RT breakup. Similarly, the RT model breakup time constant C_I can be increased to delay RT breakup, or decreased to promote faster RT breakup.

Modified KH-RT Breakup Model

The previous sections described two breakup models based on fundamental liquid/gas instability mechanisms. CONVERGE allows to run these models concurrently, as is commonly done.

One option for running them together is to use the so-called KH-RT breakup length model. If the KH-RT breakup length model is activated, an intact core or breakup length, L_b, is defined. This model assumes that only KH instabilities are responsible for drop breakup inside of the characteristic breakup distance, L_b, while both KH and RT mechanisms are activated beyond the breakup length. In this case, CONVERGE first checks if the RT mechanism can break up the droplet. If not, the KH mechanism is responsible for breakup. The breakup distance, L_b, can be tuned changing the breakup length constant, C_{bl}.

An alternative to the KH-RT breakup length model allows to run a simulation with both breakup mechanisms without the use of an *ad hoc* breakup length definition (without L_b). In this modified KH-RT model, aerodynamic instabilities (i.e., KH waves) are responsible for the primary breakup of the injected liquid blobs (also known as parents). Child drops are created during this process, and the secondary breakup of these drops is modeled by examining the competing effects of the KH and RT mechanisms. The modified KH-RT model can be used only when the creation of child parcels is included in the KH breakup model [24].

The results of work presented in [32] indicate that the modified KH-RT breakup model, in which the fixed breakup length is removed, gives the most reasonable predicted results in both engine simulation and constant-volume vessel spray simulation. For the standard KH-RT model (the KH-RT breakup length model), the model constant C_{bl} has a significant effect on the predictability of the model, and a fixed value of constant C_{bl} cannot provide a satisfactory result for different operation conditions. Also, a single model (only KH or RT) is usually unable to sufficiently describe the whole breakup process of the engine sprays.

Also, Rosin-Rammler distribution of drops with RT model is applied, as according to [31], applied to newly created child drops Rosin-Rammler distribution improved the drop size distribution predictions (and better represented experimental drop size distribution measurements than the Chi-squared distribution, which is also available in CONVERGE).

Modified KH-RT breakup model constants used in the present work are given in Table 4.1.

Table 4.1 Spray breakup model parameters

Model constant	Value
KH model size constant B_0	0.61
KH model velocity constant C_1	0.188
KH model breakup constant B_1	7.0
RT model breakup time constant C_I	1.0
RT model size constant C_{RT}	0.1
RT drops distribution	Rosin-Rammler

4.6.5 Drop Collision

CONVERGE includes two collision models (along with choice with no collision), and two models for collision outcomes. It is possible to choose from O'Rourke and NTC collision models, and from O'Rourke and Post collision outcomes.

To more accurately represent the spray dispersion by eliminating grid effects it is recommended to use the collision mesh (see Section 4.3.4).

NTC Collision Model

The No Time Counter (NTC) method is described in [36]. The NTC method is based on techniques used in gas dynamics for Direct Simulation Monte Carlo (DSMC) calculations. This model has been shown to be faster and more accurate than O'Rourke's model under certain conditions [24].

The NTC method involves stochastic (randomly determined) sub-sampling of the parcels within each cell. This potentially results in much faster collision calculations. Unlike O'Rourke's method, which incurs an additional computational cost that increases with the square of the number of parcels, the NTC method has a linear cost. O'Rourke's method assumes that multiple collisions can occur between parcels and that this process is governed by a Poisson distribution. However, the Poisson distribution is not correct unless collision has no consequences for the parcels. Since collisions change parcels' velocities, size, and number, the method of repeated sampling used by the NTC method generates more accurate answers [36].

The NTC method is derived, without assumptions, from the basic probability model for stochastic collision. The basic probability model requires that the cell size is sufficiently small such that spatial variations in spray quantities can be neglected. These assumptions are a subset of those required for deriving the O'Rourke collision model.

The NTC method first sorts the parcels into groups that reside in the same cell. This requires only 2N operations, where N is the number of droplets in a cell. Next, the NTC method picks a stochastic subsample from all of the possible pairs in a cell. The probabilities for the sub-sample pairs are multiplied by the reciprocal of this fraction, increasing the probability of collision. Sampling is done with replacement so that multiple collisions for a pair can be correctly calculated. The resulting method incurs a cost that is linearly proportional to the number of parcels, as opposed to the N-squared cost of many existing methods. A detailed derivation can be found in [36].

Post Collision Outcomes Model

The O'Rourke Collision scheme can result in grazing collisions or in coalescence. In addition to the grazing collision and coalescence outcomes, Post and Abraham [37] included both stretching separation and reflexive separation in their model based on experimental results of hydrocarbon drops. This model is called Post collision outcomes.

In this model, first it is checked if the collision of two drops would result in a bounce. If yes, the post bounce velocities are calculated for both drops. In other case, either permanent coalescence, stretching separation, or reflexive separation take place. Detailed description can be found in [24].

4.6.6 Drop Turbulent Dispersion

CONVERGE models the effects of the turbulent flow on spray drops by adding a fluctuating velocity u_i' to the gas velocity u_i.

u_i' is described using RANS (see Section 3.4.1) or LES turbulence model (when used). RANS turbulence models in CONVERGE include source terms to account for the depletion of turbulent kinetic energy due to work done by turbulent eddies to disperse the liquid spray droplets. The source terms include the fluctuating component of the fluid-phase velocity u_i'. Then, u_i' can be determined by two models [24]:

1. O'Rourke model: it is assumed that each component of u_i' follows a Gaussian distribution.
2. TKE (turbulent kinetic energy) preserving model: model chooses each component of u_i' such that $|u_i'| = \sqrt{2k}$ (where k is the cell turbulent kinetic energy).

More detailed description of both models can be found in [24]. In this work, O'Rourke model is used for the drop turbulent dispersion modeling.

4.6.7 Drop/Wall Interaction

CONVERGE offers three options for modeling drop/wall interaction [24]:

1. Rebound/Slide Model: model includes two impingement regimes, rebound and slide, based on the Weber number, We_i, of the incoming drop at impact. If We_i is less than 80 (rebound regime), the drop rebounds elastically with a normal velocity. If We_i is greater than 80, the jet model is used to update the drop velocity. In this model, the sheet thickness produced from an impinging liquid jet is calculated.
2. Wall Film Model: it is a particle-based wall film for modeling the interaction of liquid drops with solid surfaces. The model uses a hybrid approach to film modeling: some calculations assume individual particle-based quantities, while other calculations assume

film-based quantities. For example, the thickness of the film on wall face α, which is used throughout the film model, is given by:

$$h_\alpha = \frac{\sum_p V_p}{|A_{\alpha,i}|}, \tag{4.34}$$

where V_p is the volume of parcel p, $A_{\alpha,i}$ is the area projection vector of face α, and the summation is over all particles located on face α.

3. Drop Vanish Model: with this model activated the spray droplets vanish as they impinge on the wall boundary. The mass of drops disappears from the simulation in such an instance. This is not the same as drop vaporization.

In this work, the Wall Film model is used. For it, the film momentum equation is used to model liquid film transport. However, it is used to update velocities of particles that impinged on a solid surface in a previous time-step. If a particle has just impinged on a wall in the current time-step, CONVERGE calculates its velocity with the jet model as in the Rebound/Slide model (rebound Weber number can be set by user).

The Wall Film model also takes into account drop/film splashing. Three models are available: O'Rourke, Kuhnke, and Bai-Gosman. Kuhnke and Bai-Gosman models consider the wall temperature, the Weber numbers of the impinging drops, and the wall condition (i.e., wet or dry) to determine the extent of drop/film splashing. The Bai-Gosman model in CONVERGE has been customized for simulations that involve urea selective catalytic reduction. This model should be used with caution for non-urea applications. In this work O'Rourke model is chosen. Detailed description for all three models can be found in [24].

The Wall Film model includes two other effects: film separation and film striping (if enabled). Film separation can occur if wall film particles flow over a sharp corner. The separation criterion is used to determine if film separation takes place: if yes, the film parcels are converted to spray parcels with a diameter equal to the film thickness. Film stripping takes place due to the growth of waves on the surfaces caused by the aerodynamic forces acting on the film. Once the waves reach a critical amplitude, fragments of the liquid are broken off which contract to form cylindrical ligaments that are believed to move normal to the ligament axis. As a result, capillary forces cause the unstable ligaments to break into drops.

4.6.8 Vaporization

CONVERGE contains vaporization models to determine how the radius of a drop changes over time. The Frossling correlation and the Chiang correlation are available. Also, droplet boiling model can be enabled. Finally, CONVERGE contains two methods for computing thermal transfer to a drop: Uniform Temperature model and Discretized Temperature model [24].

In this work, Frossling correlation with droplet boiling model is used. Thermal transfer to a drop is calculated using the Discretized Temperature model.

Frossling Correlation

Frossling correlation is used to calculate droplet radius change, as once the liquid spray is injected into the computational domain, a model is needed to convert the liquid into gaseous vapor. The Frossling correlation is:

$$\frac{dr_0}{dt} = -\frac{\alpha_{spray}\rho_g D}{2\rho_l r_0} B_d Sh_d, \tag{4.35}$$

where α_{spray} is the user-specified scaling factor for the mass transfer coefficient, D is the mass diffusivity of liquid vapor in air. B_d is defined as:

$$B_d = \frac{\Upsilon_1' - \Upsilon_1}{1 - \Upsilon_1'}, \tag{4.36}$$

where Υ_1' is the vapor mass fraction at the drop's surface, Υ_1 is the vapor mass fraction, and Sh_d [in Eq. (4.35)] is the Sherwood number given by:

$$Sh_d = \left(2 + 0.6 Re_d^{1/2} Sc^{1/3}\right) \frac{\ln(1 + B_d)}{B_d}, \tag{4.37}$$

where Re_d:

$$Re_d = \frac{\rho_{gas}|u_i + u_i - v_i'|d}{\mu_{air}}, \tag{4.38}$$

where d is the drop diameter and μ_{air} is the air viscosity which is evaluated at the temperature $\overline{T}$ given by:

$$\overline{T} = \frac{T_{gas} + 2T_d}{3}, \tag{4.39}$$

where T_{gas} is the gas temperature and T_d is the drop temperature.

Then, $Sc = \frac{\mu_{air}}{\rho_{gas}D}$ in Eq. (4.37) is the Schmidt number of air, and D is determined from the correlation:

$$\rho_{gas}D = 1.293 D_0 \left(\frac{\overline{T}}{273}\right)^{n_0 - 1}, \tag{4.40}$$

where D_0 and n_0 are experimentally-determined model constants.

In addition, Υ_1' is determined from the expression:

$$\Upsilon_1' = \frac{M_{C_nH_{2m}}}{M_{C_nH_{2m}} + M_{mix}\left(\frac{p_{gas}}{p_v} - 1\right)}, \tag{4.41}$$

where $\mathrm{M_{mix}}$ is the molecular weight of the mixture (not including vapor from the liquid species), $\mathrm{p_{gas}}$ is the gas pressure, and $\mathrm{p_v}$ is the vapor pressure at the current droplet temperature.

Droplet Boiling Model

To model droplet boiling, CONVERGE includes a model for droplet radius change in the boiling regime. Eq. (4.42) below is used to calculate the time rate of change of the droplet radius when the droplet temperature exceeds the boiling point:

$$\frac{dr_0}{dt} = \frac{k_{air}}{\rho_d c_{p,air} r_0}\left(1 + 0.23\sqrt{Re_d}\right) \ln\left[1 + \frac{c_{p,air}(T_{air} - T_d)}{h_{fg}}\right], \tag{4.42}$$

where $\mathrm{k_{air}}$ is the thermal conductivity, $\mathrm{c_{p,air}}$ is the specific heat capacity, $\mathrm{Re_d}$ comes from Eq. (4.38), and $\mathrm{h_{fg}}$ is the heat of vaporization. Once the droplet temperature, $\mathrm{T_d}$, reaches the boiling temperature, this model considers the droplet temperature fixed at the boiling temperature.

The droplet boiling model can be used in conjunction with either the Frossling or the Chiang correlation for droplet radius change. CONVERGE models droplet radius change with the selected correlation until the droplet temperature reaches the boiling point. At the boiling point, CONVERGE uses Eq. (4.42) to model droplet radius change [24].

Discretized Temperature Model

As has been mentioned at the beginning of this section, there are two different methods for computing thermal transfer to a drop in CONVERGE:

1. Uniform Temperature model: the droplet temperature is assumed to be uniform and temperature is solved using two ordinary differential equations, ODEs.
2. Discretized Temperature model: the droplet temperature is assumed to be spherically symmetric and temperature is solved using a partial differential equation (the 1D spherical heat equation), PDE, for the droplet temperature.

When Discretized Temperature model is used, for all droplets whose radii are larger than the user-specified *model_transition_radius*, CONVERGE will use the droplet thermal transfer using a PDE to calculate the droplet temperature. For all droplets whose radii are smaller than or equal to the *model_transition_radius*, CONVERGE will use ODEs. In other words, below this radius, the evaporation model will switch to the Uniform Temperature model.

If a value larger than any possible droplet for *model_transition_radius* is specified, CONVERGE will use only ODEs for determining droplet temperature. Using the Discretized Temperature model can be computationally expensive, but is useful for generating accurate spray temperature results, as the ODE tends to under-predict the temperature and evaporation rate for large drops. Detailed description of both the Uniform Temperature model and the Discretized Temperature model is given in [24].

4.6.9 Summary of Spray Modeling

Models used for the spray modeling in this work are summarized in Table 4.2.

Table 4.2 Models used for the spray modeling

Phenomenon to be modeled	Model
Actual nozzle geometry	Discharge coefficient model
	Correlation for velocity coefficient
Initial injected drop size	Blob model
Drop drag	Dynamic drop drag model
Spray breakup	Modified KH-RT model
	Rosin-Rammler distribution with RT
Drop collision	NTC collision model
	Post collision outcomes
Drop turbulent dispersion	O'Rourke model
Drop/wall interaction	Wall film model without film strip
	O'Rourke film splash model
Vaporization	Frossling model
	Drop boiling model
	Discretized Temperature model

5 Experimental Data and CFD Model Calibration

In the present chapter the preparation and validation of the CFD model is explained, starting from the engine specifications, experimental data, and continuing with determination of initial conditions and various parameters used in the CONVERGE CFD software.

5.1 Engine Specifications and Operating Points

The engine used in this work is FPT F1C 3.0 L Euro VI DI light-duty diesel engine, having the specifications shown in Table 5.1. The combustion chamber is a bowl-in type located in the center of the piston. An eight-hole injector is centered in the cylinder bore. The piston is symmetrical, and a sector of 45° (one eight of the piston due to the eight-hole injector) is simulated. The computational mesh used in this work is shown in Figure 5-1.

Table 5.1 Engine specifications

Parameter	Units	Value
Number of cylinders	–	4
Bore × stroke	mm	95.8 x 104
Connecting rod length	mm	158
Crankshaft offset	mm	0.5
Displacement	cm^3	2998
Compression ratio	–	17.5
Valves per cylinder	–	4
Intake valve closing (IVC)	deg	-145
Exhaust valve opening (EVO)	deg	110
Number of injector nozzle orifices	–	8
Nozzle orifice diameter	μm	138
Included spray angle (in X-Z plane)	deg	139.8

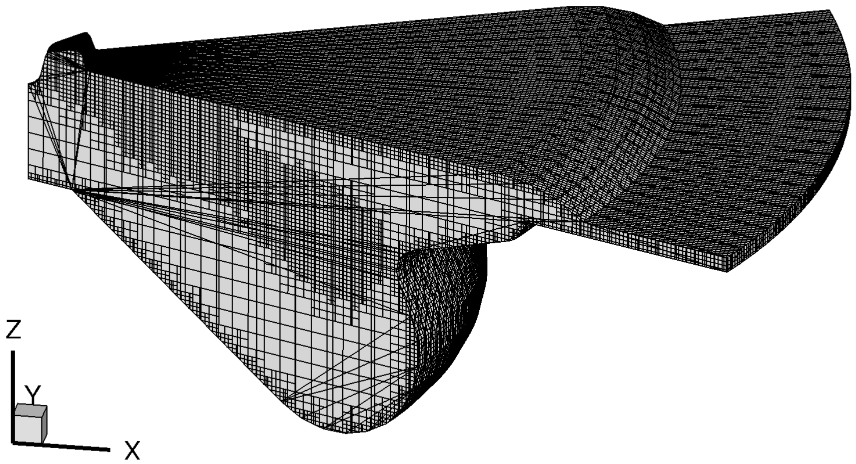

Figure 5-1 Computational mesh at TDC

Operating points [engine speed versus load (measured in brake mean effective pressure, BMEP)] used for experiments of the engine are shown in Figure 5-2. The black solid line represents a full load operation over the speed range. Two red points are operating points used in the present work to validate the CFD model. They are labelled as follows:

1. Full load: o. p. 2000 [rev/min] x 18 [bar].
2. Part load: o. p. 2000 [rev/min] x 9 [bar].

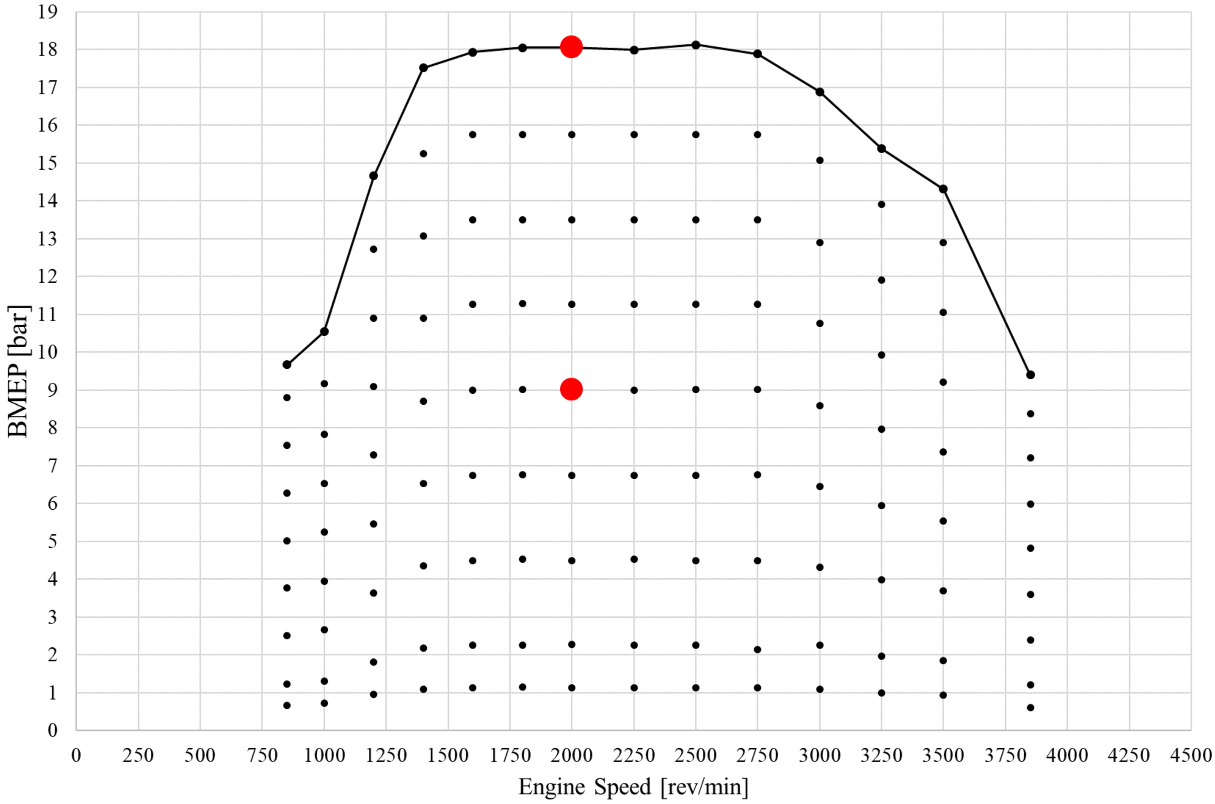

Figure 5-2 Engine operating points

Some experimental parameters for both operating points are given in Table 5.2. These parameters will be used for developing the CFD model.

Table 5.2 Experimental data

Parameter	Units	Value	
		2000 [rev/min] x 18 [bar]	2000 [rev/min] x 9 [bar]
Total trapped mass per cylinder at IVC (air + EGR)	kg	0.001578	0.001076
EGR mass fraction	%	10.2	17.2
Fuel rail pressure	bar	1398	1381
Fuel mass injected per cylinder*	mg	76.9	39.0
Relative air-fuel ratio	–	1.27	1.55
* In engine sector CFD simulations, mass of injected fuel per sector has to be defined			

5.2 Experimental Data

Experimental data has been obtained while testing the F1C engine in a laboratory at the Energy Department of Politecnico di Torino. Many experimental parameters are available in their final form, however the heat release rate has to be calculated using other data, and the fuel injection rate curves have to be interpolated to match injection times used in testing. The procedures to analyze the experimental data and prepare it to be used in CFD analysis are explained in the present section.

5.2.1 In-Cylinder Pressure

Final in-cylinder pressure curves were obtained by using TAF (time average filtering) procedure to filter in-cylinder pressure signals obtained during the engine testing. This procedure is not explained in the present thesis, as the filtering was done by other people at the Energy Department.

Figure 5-3 shows the in-cylinder pressure curves for both operating points analyzed (see Section 5.1) from IVC (at -145 CAD) to EVO (at 110 CAD). The maximum peak firing pressure at full load is 138.9 bar, while at part load it is 103.1 bar.

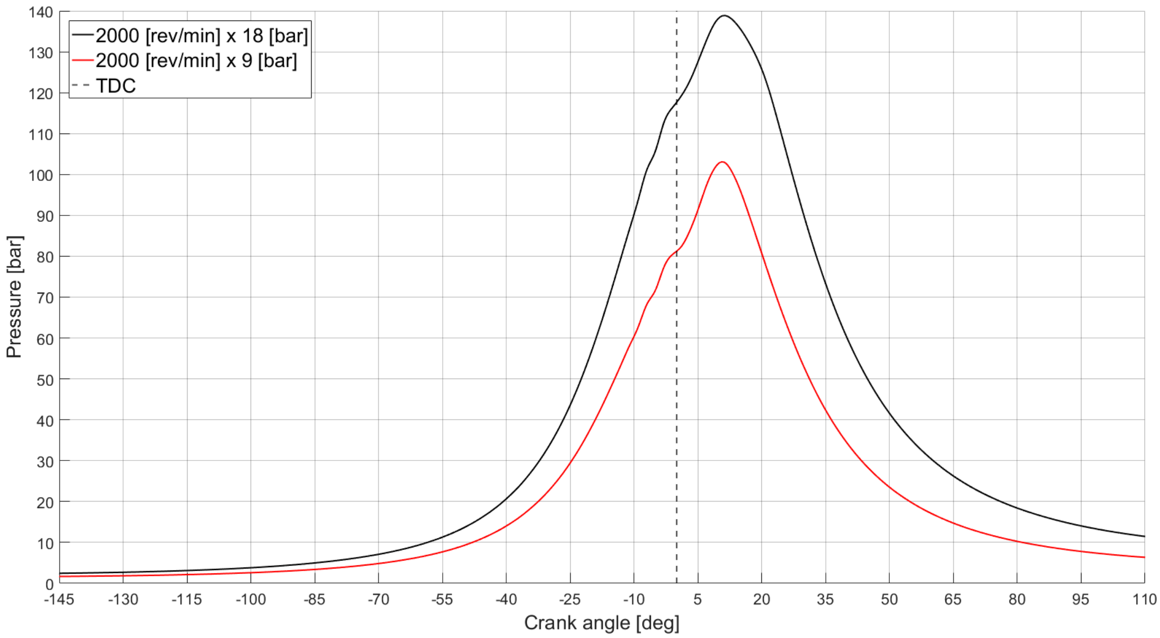

Figure 5-3 Experimental in-cylinder pressure

5.2.2 Heat Release Rate

Accurate heat release analysis of cylinder pressure data is a powerful tool used in the development of diesel engines [38]. In the present thesis, a traditional single-zone First Law heat release model is used to obtain the heat release rate (HRR) from the in-cylinder pressure data.

Single-zone-models are normally employed in preference to the potentially more accurate multi-zone models since they are less complex, numerically more efficient and usually yield results of similar accuracy. The single-zone models do not include spatial variations and hence assume uniform charge temperature and composition (for example, the single-zone model peak charge temperature is much lower than the actual peak burned gas temperature). Terms for work, chemical energy changes (heat release) and changes in sensible internal energy are always included.

Additional terms may also be incorporated for cylinder charge to wall heat transfer, crevice volumes, blow-by, fuel enthalpy and in-cylinder fuel injection mass. With the exception of charge to wall heat transfer, these additional effects are usually small for production engines and can be neglected with minimal loss of accuracy. The charge to wall heat transfer is also often ignored for simplicity and the heat release thus determined is referred to as "net" heat release, whose values are typically 15% lower than those obtained on a "gross" heat release basis (with heat transfer effects included) [38].

A derivative with respect to distance (in crank angles) of the traditional single-zone First Law equation has to be calculated in order to obtain the rate of heat release. The equation to calculate the net heat release rate used in the present work is:

$$\mathrm{d\dot{Q}_{hr}} = \frac{\mathrm{k}}{\mathrm{k}-1}\mathrm{p}\frac{\mathrm{dV}}{\mathrm{d\theta}} + \frac{1}{\mathrm{k}-1}\mathrm{V}\frac{\mathrm{dp}}{\mathrm{d\theta}}, \tag{5.1}$$

where k is the ratio of specific heats, p is the in-cylinder pressure, V is the cylinder volume, and θ is the crank angle.

The ratio of specific heats, *k*, varies with charge temperature and composition, and is known to have a very significant effect on the calculated heat release energy. Ideally, *k* would be varied with fuel specification, air to fuel ratio (AFR), exhaust gas recirculation (EGR), charge pressure and charge temperature but for general purpose applications *k* is usually made a function of temperature only. An approximate relationship is used for *k* which was defined to be used in diesel engines [38]:

$$\mathrm{k} = 1.35 - 6 \cdot 10^{-5}\mathrm{T} + 1 \cdot 10^{-8}\mathrm{T}^2 \tag{5.2}$$

To, use Eq. (5.2), the mean in-cylinder temperature at each crank angle degree is calculated using the perfect gas equation of state (see Section 3.2.4), which can be rewritten as follows:

$$\mathrm{T} = \frac{\mathrm{pV}}{\mathrm{m_{air}R_{air}} + \mathrm{m_{EGR}R_{EGR}}}, \tag{5.3}$$

where m is the mass, and R is the gas constant.

Figure 5-4 shows the HRR curves for both operating points analyzed from -25 CAD (before start of injection, see the following Section) to 95 CAD (HRR drops to 0 at about 75 CAD).

The HRR curves in Figure 5-4 are uncharacteristically smooth for a diesel combustion. The reasons are the TAF procedure applied to the experimental in-cylinder pressure data (as mentioned in Section 5.2.1) and the simplified single-zone First Law heat release model used for calculation of HRR. Filtered pressure curves lose their "sharp" parts, while the simplified HRR calculation model does not consider in-cylinder fuel injection effects, etc.

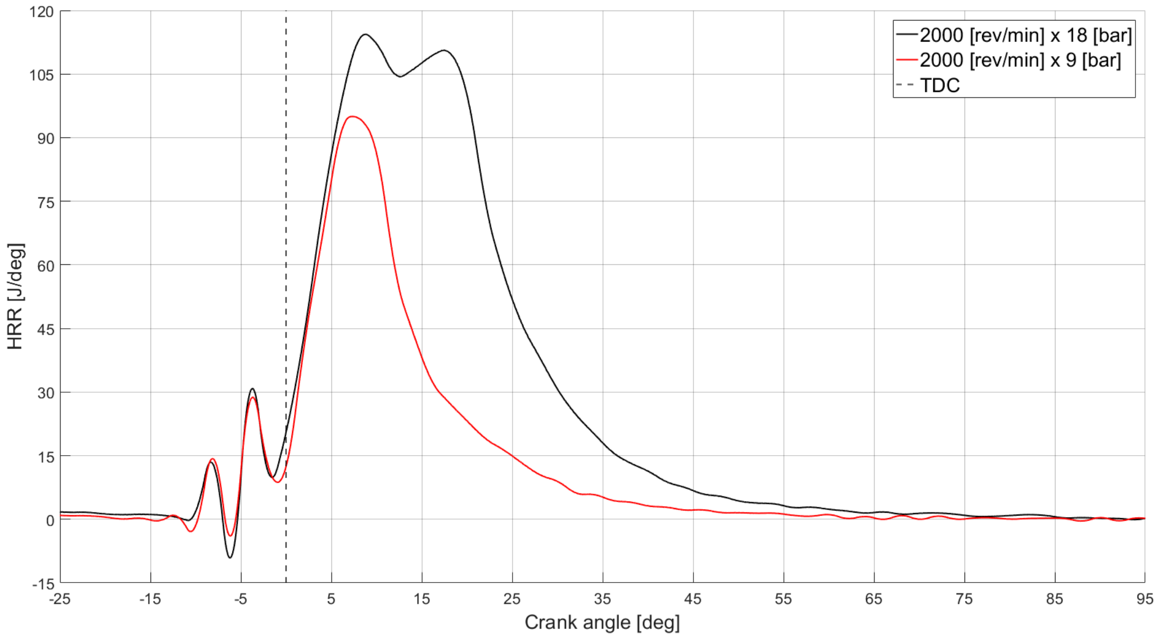

Figure 5-4 HRR calculated from experimental in-cylinder pressure

5.2.3 Injection Parameters

Following experimental data is available from the engine testing activity (1 to 4 in the list) and the injector testing (5 to 6 in the list):

1. Number of injection events.
2. Mass of the injected fuel during each injection event.
3. Timing of injection events (start of injection, SOI).
4. Energizing time (ET) for each injection event.
5. Injection rates for several rail pressures and energizing times.
6. Nozzle opening delay (NOD).

Table 5.3 provides the injection data obtained during the engine testing for both operating points.

Table 5.3 Experimental data for injection

Parameter	Units	Value	
		2000 [rev/min] x 18 [bar]	2000 [rev/min] x 9 [bar]
Number of injection events	–	3 [pilot 1 (P1), pilot 2 (P2), main (M)]	3 [pilot 1 (P1), pilot 2 (P2), main (M)]
Injected mass (P1 / P2 / M)	mg	0.7* / 3.0 / 73.2	1.0* / 2.7 / 35.3
SOI** (P1 / P2 / M)	CAD	-14.7 / -9.4 / -4.3	-15.6 / -10.1 / -4.7
ET (P1 / P2 / M)	µs	131 / 157 / 705	134 / 150 / 436
* Error of ±0.5 mg is possible ** SOI here defines the start of electrical signal, and not the start of hydraulic injection			

Figure 5-5 shows fuel injection rate-shapes at 1400 bar injection pressure (see Table 5.2 for experimental data) for different energizing times. From the injection rate data, the nozzle opening delay is determined, which is equal to 220 µs, or to 2.64 deg at 2000 rev/min engine speed.

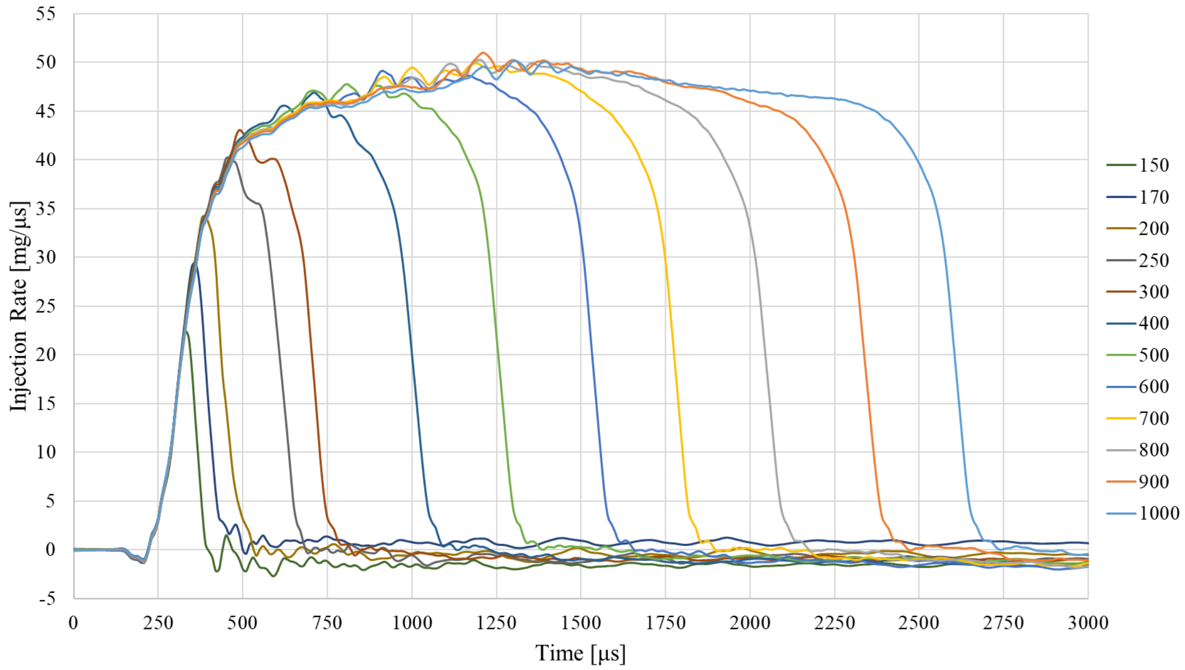

Figure 5-5 Experimental injection rate-shapes at 1400 bar injection pressure for different ET

Injection rate-shape profiles used for CFD simulations are obtained by interpolating the shapes in Figure 5-5 to match the energizing times given in Table 5.3. The area below the rate-shapes (which equal the injected mass) has to be found out to compare with the mass injected during each injection event (see Table 5.3), and confirm the correctness of these rate-shapes. Normalized injection rate-shapes for operating points are shown in Figure 5-6.

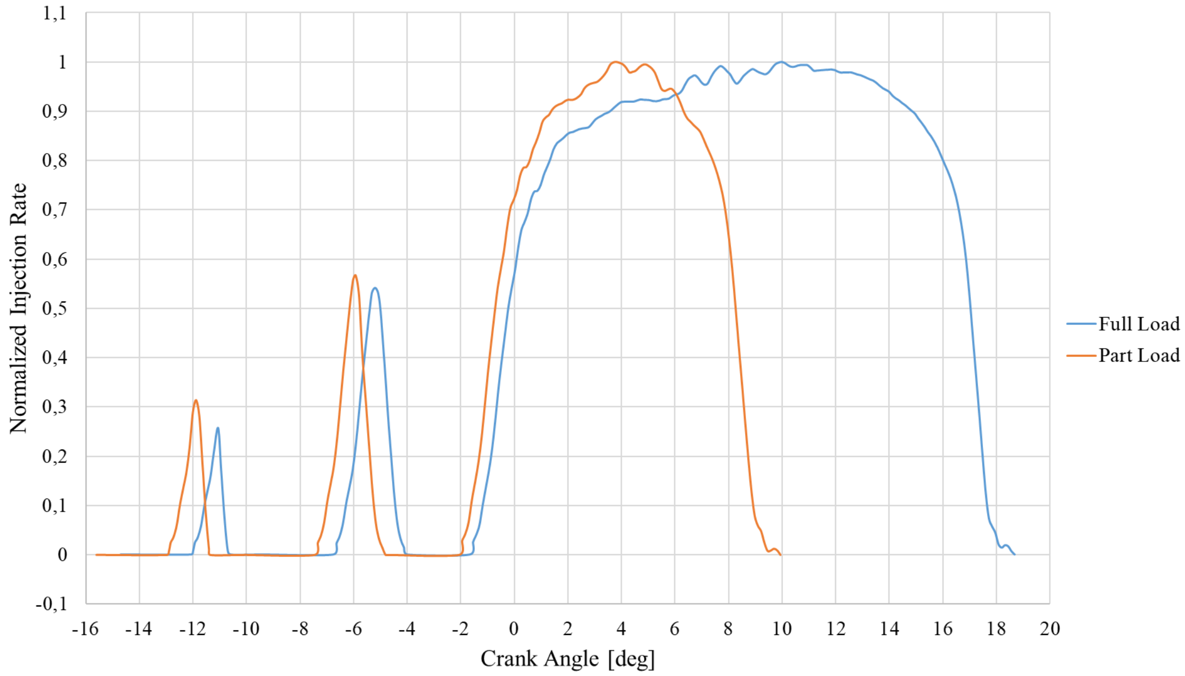

Figure 5-6 Normalized injection rate-shapes for CFD simulations

CONVERGE CFD software also requires to determine SOI timing and the injection duration as inputs. If the start of electrical signal timing (see Table 5.3) is used as SOI, shapes in Figure 5-6 can be used directly. However, if NOD is considered by adding it to the start of electrical signal timing to obtain the start of hydraulic injection to be used as input in the software, the initial part of injection rate-shapes (where the rate equals 0) has to be removed.

5.2.4 Pollutant Emissions

Table 5.4 gives experimental values of NOx, soot, CO, and HC emissions for both operating points.

Table 5.4 Experimental data for pollutant emissions

Pollutant	Units	Value	
		2000 [rev/min] x 18 [bar]	2000 [rev/min] x 9 [bar]
NOx	mg	1.51	0.653
Soot	mg	0.00782	0.013
CO	mg	0.264	0.115
HC	mg	0.0165	0.0163

5.3 Mesh

The base grid size is 1 mm, and parameters used for the fixed embedding (see Section 4.3.2) and the Adaptive Mesh Refinement (see Section 4.3.3) are given in Table 5.5.

Table 5.5 Mesh parameters

Parameter	Value
Fixed Embedding	
Nozzle (type: nozzle)	Scale: 2
Piston (type: boundary)	Scale: 2
Head (type: boundary)	Scale: 2
Adaptive Mesh Refinement	
Velocity	Scale: 2; sub-grid criterion: 1 m/s
Temperature	Scale: 2; sub-grid criterion: 5 K
Species (N-C7H16)	Scale: 2

Visualization of the mesh during a simulation is given in Figure 4-5, Figure 4-6, and Figure 5-1, where the finer mesh next to boundaries or in nozzle region (fixed embedding), and in the spray region (AMR) can be seen.

5.4 Initial Conditions and Inputs

5.4.1 Engine Parameters

Along with engine geometrical parameters given in Table 5.1, initial swirl has to be defined. In the present work, the intake process is not simulated, and it is considered that at IVC (when the simulation starts) the swirl is homogeneous within the cylinder. This swirl is defined by the swirl ratio (SR) (see Section 6.2) and the swirl profile (increasing the swirl profile, flow velocity decreases near the cylinder wall). The latter is equal to 3.11, as recommended by the CONVERGE, and the swirl ratios for both operating points are taken from 1D simulations performed for the analyzed engine with the GT-POWER software. For simulations at full and part load, SR is equal to -1.48 and -1.46, respectively (at IVC).

5.4.2 Global Transport Parameters

There are two global transport parameters used in the CONVERGE CFD software: turbulent Prandtl number, and turbulent Schmidt number (see Section 6.3). The Prandtl number is set equal to 0.9, as recommended by the CONVERGE. Then, the Schmidt number equal to 0.5 was found to be the most accurate for diesel engines with modern injection systems [39]. Thus, this value is selected in the present work.

5.4.3 Boundaries

Boundaries of the computational domain (see Figure 5-1) are five:

1. Piston. According to the terminology used in the CONVERGE CFD software, the piston is defined as a translating wall with piston motion. For more details, see [24].
2. Head. Boundary type is stationary wall.
3. Liner. Boundary type is stationary wall.
4. Front face. Boundary type is periodic stationary with sector shape. Periodic boundaries are specified in pairs (in the present case, the front face is paired with the back face). During the simulation, the software reads the match keyword and copies the values of each boundary condition on the first periodic boundary to its matching boundary [24]. Only this way it is possible to simulate an engine sector (see Section 5.1).
5. Back face. It is a periodic boundary, paired with the front face.

Temperatures for each boundary (except of periodic boundaries, which do not require to define the temperature) are set up according to several researches, and are given in Table 5.6. These temperatures are considered as surface mean temperatures at IVC.

Table 5.6 Temperature of boundaries

Boundary	Units	Value		Reference
		2000 [rev/min] x 18 [bar]	2000 [rev/min] x 9 [bar]	
Piston	K	493	453	[40]
Head		473	433	[41]
Liner		398	388	[42]

5.4.4 In-Cylinder Region

Pressure and Temperature

Pressure at IVC is defined from the experimental measurements (see Section 5.2.1). Then, temperature is calculated (taking into account the composition of the charge) using the perfect gas equation of state given in Eq. (5.3). Defined pressure and temperature for analyzed operating points are given in Table 5.7.

Turbulence Initialization

When the intake flow is not calculated (in the present thesis, a simulation of the intake process is not performed), engine simulations use empirical correlations to set the turbulence characteristics for the turbulence model at intake valve closure. A commonly used correlation for the turbulence kinetic energy is [43]:

$$k = C_1 U^2, \tag{5.4}$$

where C_1 is a constant, and U is the average intake flow velocity.

The value of C_1 is 0.23 [43], while U is taken from results of 1D simulations performed with the GT-POWER software by the manufacturer of the engine used in the present work. Both values of U and the calculated turbulence kinetic energy for both operating points are given in Table 5.7.

Another parameter is turbulence dissipation, which is calculated using the following, length-scale based, equation [24]:

$$\varepsilon = c_\mu^{3/4} k^{3/2} \frac{1}{l}, \tag{5.5}$$

where c_μ is a turbulence model constant, k is the turbulence kinetic energy, and l is the turbulence length scale.

c_μ for the RNG k-ε model used in the present work (see Section 3.4.3) is 0.0845, k is calculated using Eq. (5.4), and l can be estimated from a physical dimension in the domain. The length scale should not be larger than the dimension of the problem, since the turbulent eddies would be larger than the problem size [44]. Thus, l is selected to be equal to 7 % of the cylinder bore.

Summary

Table 5.7 presents parameters calculated to set initial conditions for the in-cylinder region to be used in CFD simulations.

Table 5.7 In-cylinder region initial conditions

Parameter	Units	Value	
		2000 [rev/min] x 18 [bar]	2000 [rev/min] x 9 [bar]
Pressure	Pa	245530	168500
Temperature	K	402	406
Average intake flow velocity	m/s	17.5	19.3
Turbulence kinetic energy	m^2/s^2	70.4	85.7
Turbulence dissipation	m^2/s^3	13805	18532

5.4.5 Inputs for Spray Simulation

Nozzle orifice diameter and included spray angle are given in Table 5.1, total injected masses for analyzed operating points are presented in Table 5.2, and injection rate-shapes are shown in Figure 5-6. The CONVERGE CFD software asks additional parameters for the spray modeling: number of injected parcels and spray cone angle. Determination of these parameters is presented in this section.

Total Number of Injected Parcels

CONVERGE recommends to use $1.5 \cdot 10^{-10}$ kg of fuel per parcel for 0.25-0.35 mm cells. However, injecting more parcels helps to increase accuracy and stability of simulation. Table 5.8 gives calculated numbers for both operating points.

Spray Cone Angle

When experimental spray data is not available, following equation can be used to calculate the spray cone angle [45]. This is an empirically derived equation for the vaporizing spray.

$$\tan\left(\frac{\theta}{2}\right) = c \cdot \left[\left(\frac{\rho_a}{\rho_f}\right)^{0.19} - 0.0043\sqrt{\frac{\rho_f}{\rho_a}}\right], \tag{5.6}$$

where c is a constant equal to 0.26 [45], ρ_a is the ambient gas density, and ρ_f is the fuel density.

The ambient gas density is calculated using the perfect gas equation of state [Eqs. (3.11) and (5.3)], while the fuel density is selected as 848 kg/m^3 (defined by CONVERGE for DIESEL2 fuel available in the software and used in the present thesis). Also, as the ambient gas density changes during the engine cycle, and a constant spray cone angle has to be defined in the software, it was decided to calculate it at the start of the main injection event.

For both analyzed operating points of the engine, the spray cone angles are given in Table 5.8.

Summary

Table 5.8 presents parameters for the simulation of injection process to be used in CFD simulations.

Table 5.8 Calculated injection parameters

Parameter	Units	Value	
		2000 [rev/min] x 18 [bar]	2000 [rev/min] x 9 [bar]
Total number of injected parcels	–	100000	50000
Spray cone angle	deg	13.8	12.0

5.5 Validation of CFD Model

The created CFD model has to be validated against the experimental data. Matching the in-cylinder pressure is one of the primary means of validating the accuracy of an internal combustion engine CFD simulation, followed by the HRR and emissions data matching. Most important aspects for the correct matching of numerical and experimental data in diesel simulations are the following:

1. Sufficient mesh resolution in the spray region, combustion region, and at combustion chamber boundaries.
2. Matching of the compression line in the pressure curve: correct initial trapped mass has to be defined, taking into account the pressure and temperature at IVC, and the composition of the charge (air and products of the previous combustion; the composition is calculated automatically by the CONVERGE CFD software according to the specified EGR level).
3. To correctly simulate the spray and combustion, the flow conditions at start of combustion must be correct, including bulk mass flow (swirl) and turbulence (TKE).
4. To match the pressure line during the combustion, correct injection rate-shape profile and injected mass of fuel have to be defined. Also, models of the spray (see Section 4.6), combustion (see Section 4.4), and turbulence (see Section 3.4) have to be set-up properly.
5. Matching of the expansion line in the pressure curve: if experimental and simulated HRR are similar, and the trapped mass is accurately predicted, the expansion line should match the experimental data. Too high premixed burn, providing an overestimation of the peak firing pressure, may result in increased wall heat transfer and a lower pressure curve tail.
6. Matching the emissions data: combustion modeling and emissions modeling (see Section 4.5) play a fundamental role in predicting engine pollutant emissions. However, also the mesh resolution (see Section 6.1) and initial conditions (see Sections 6.2 and 6.3) influence the results.

In this section, validation of the developed CFD model is presented for both operating points in terms of the in-cylinder pressure, HRR, integrated heat release, NOx and soot emissions.

5.5.1 Operating Point 2000 [rev/min] x 18 [bar]

In-cylinder pressure at full load between IVC and EVO, and near TDC, are shown in Figure 5-7 and Figure 5-8, respectively.

Figure 5-7 shows that the compression line is matched perfectly, and correct peak firing pressure is achieved during the combustion. However, the simulation predicts more intensive combustion from around 10 CAD, indicated by the overpredicted in-cylinder pressure between 10 CAD and 23 CAD. Nevertheless, the maximum difference is acceptable, being less than 2 %. Overpredicted pressure near the peak results in slightly underestimated in-cylinder pressure near EVO. Again, the maximum difference is relatively small, being 0.54 bar.

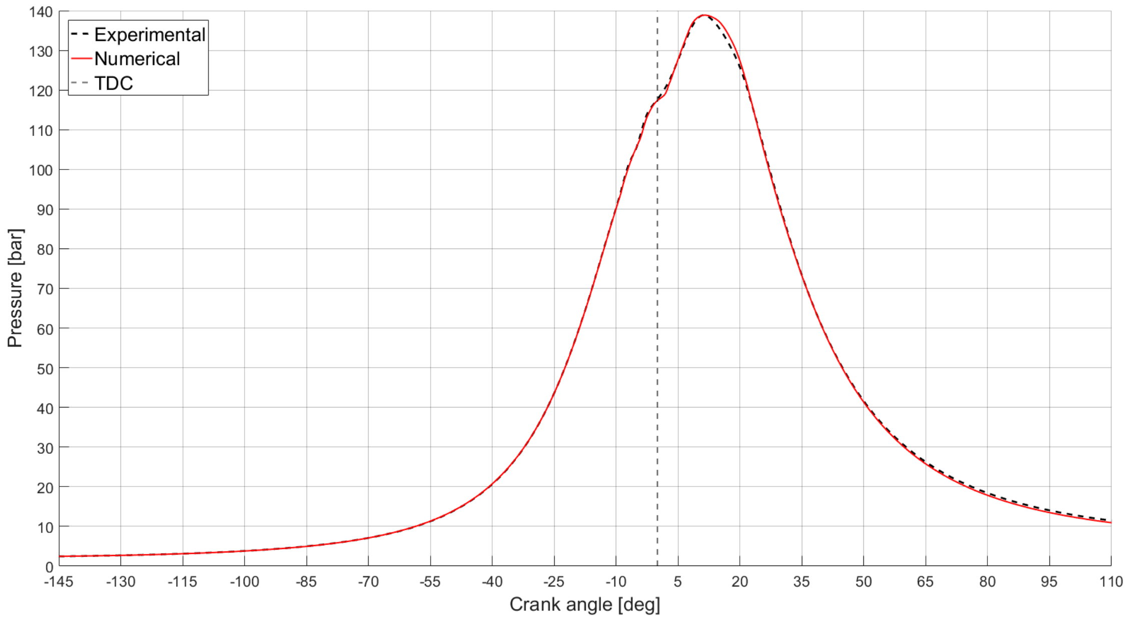

Figure 5-7 In-cylinder pressure for CFD model validation at full load

Looking closer at pressure curves near TDC (Figure 5-8), following remarks can be made: the combustion of fuel injected during the second pilot injection event is slightly delayed for the numerical case (between -5 CAD and 2 CAD), and pressure rise during the premixed burn (from 2 CAD to 10 CAD) is higher than for the experimental case. The first may be associated with uncertainty of SOI timing (see Section 5.2.4), as some errors are expected to appear in experimental measurements.

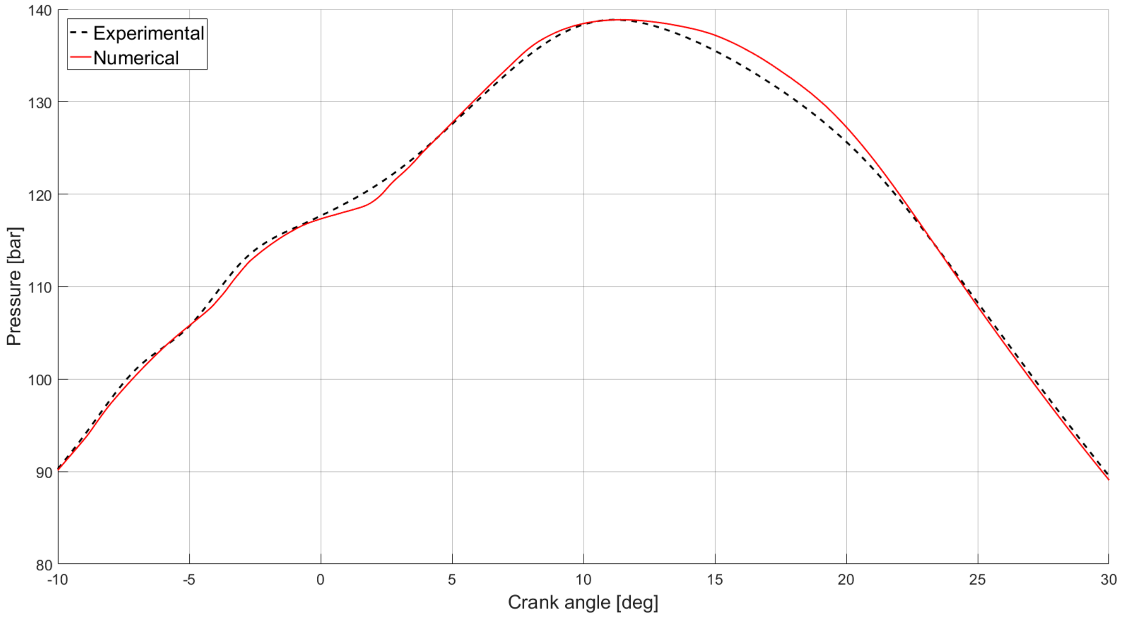

Figure 5-8 In-cylinder pressure near TDC for CFD model validation at full load

Heat release rate and integrated heat release at full load are shown in Figure 5-9 and Figure 5-10, respectively.

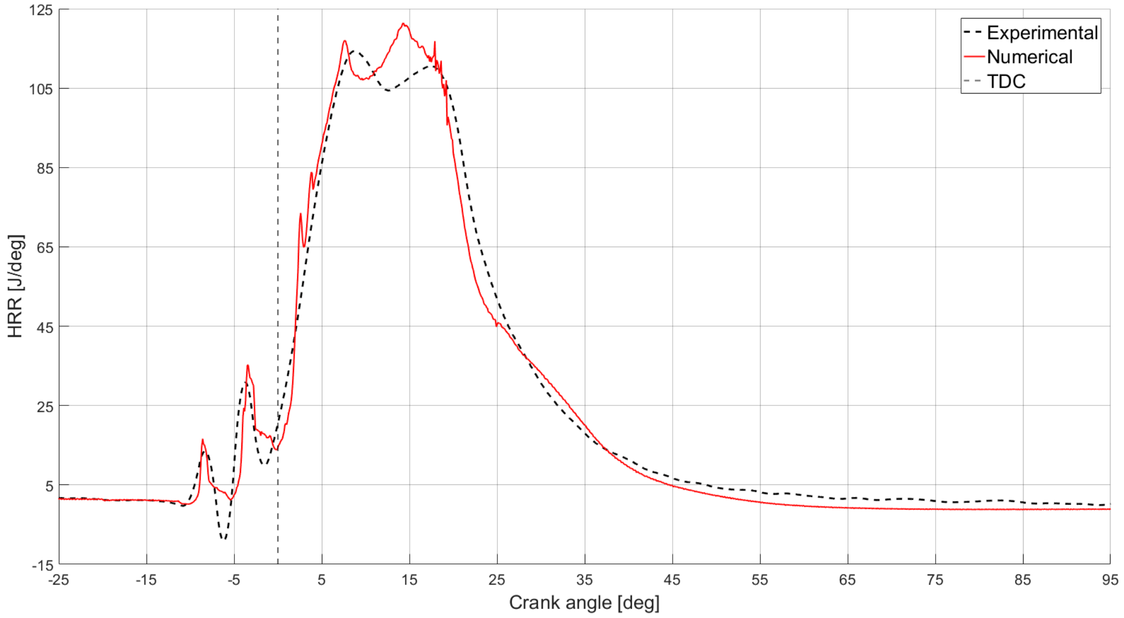

Figure 5-9 HRR for CFD model validation at full load

Matching between experimental and numerical HRR is good, the overall shape is estimated correctly. However, as mentioned talking about the in-cylinder pressure, the combustion of second pilot is slightly delayed, and premixed phase is more intensive (between 0 CAD and 5 CAD). Also, HRR is overestimated between 10 CAD and 18 CAD, which results in the in-cylinder pressure overestimation over the same period as mentioned before. Finally, Figure 5-10 shows somehow faster combustion for the numerical case (in agreement with the previous discussion), the overall matching between experimental and numerical curves being very good.

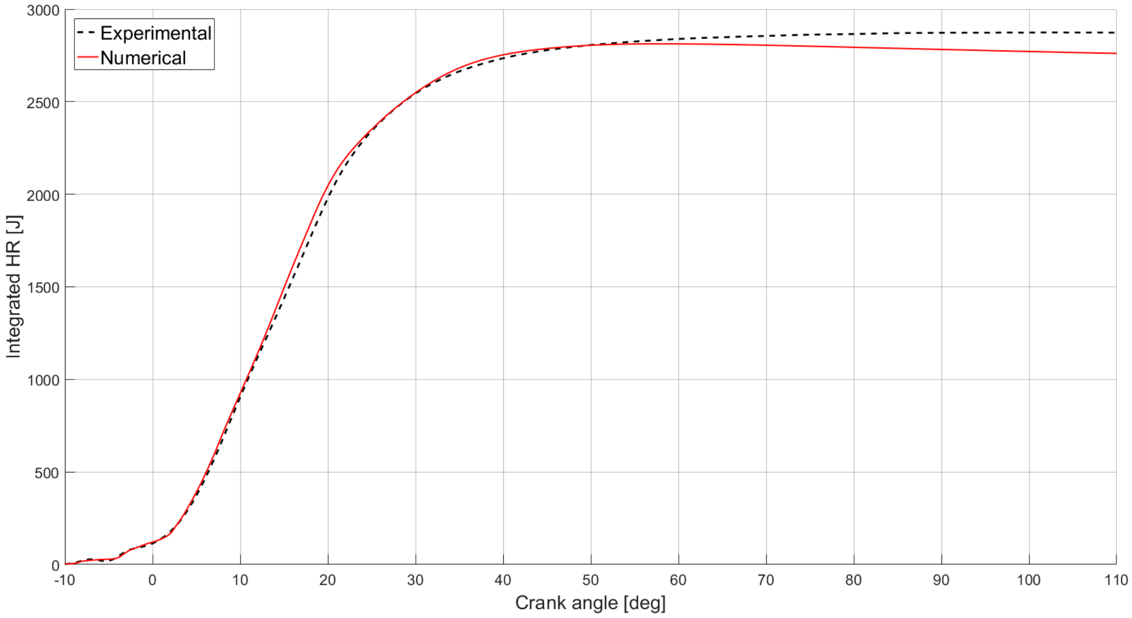

Figure 5-10 Integrated HR for CFD model validation at full load

Figure 5-11 shows curve representing NOx mass within the cylinder over the simulation at full load, and experimental value. Then, Figure 5-12 presents the same comparison for soot.

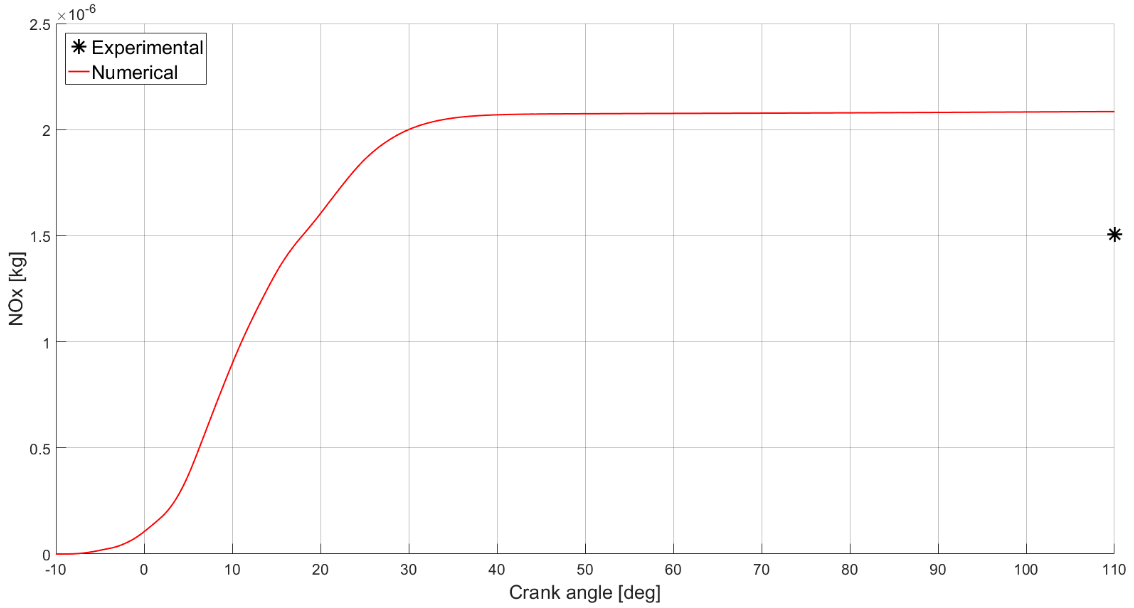

Figure 5-11 NOx mass for CFD model validation at full load

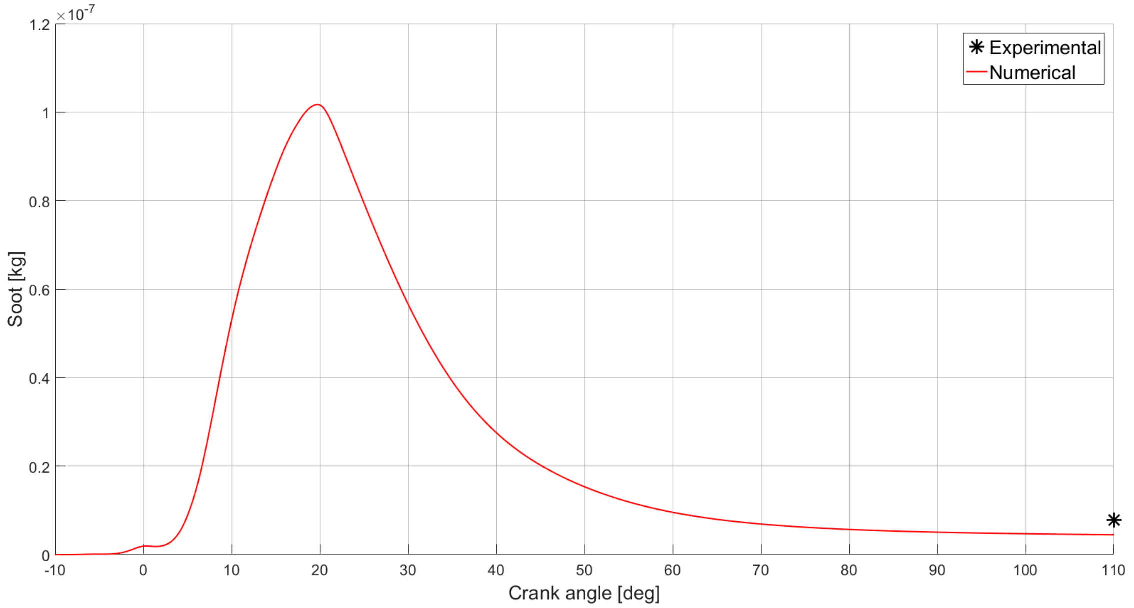

Figure 5-12 Soot mass for CFD model validation at full load

Figure 5-11 shows that NOx emissions are overestimated by the CFD model. As has been explained in Section 2.5.1, the premixed phase of combustion has a high impact on NOx production. Thus, as the simulated premixed phase has been found to be more intense than the experimental, initial NOx production is increased. Also, higher HRR during the mixing controller combustion (from 10 CAD to 18 CAD in Figure 5-9) helps to keep the in-cylinder temperature higher during the early expansion stroke, delaying the freezing of NOx production process.

As NOx production is overestimated, the soot production is underestimated, as can be seen in Figure 5-12. Measures that increase soot oxidation, e.g. the increase of the oxidizer temperature or the increase of residence times, typically lead to increased emissions of NOx. In this case, more fuel burning in the premixed phase provides more time for soot oxidation, while intensive mixing-controlled combustion keeps in-cylinder temperatures high enough for the oxidation process.

5.5.2 Operating Point 2000 [rev/min] x 9 [bar]

In-cylinder pressure at part load between IVC and EVO, and near TDC, are shown in Figure 5-13 and Figure 5-14, respectively.

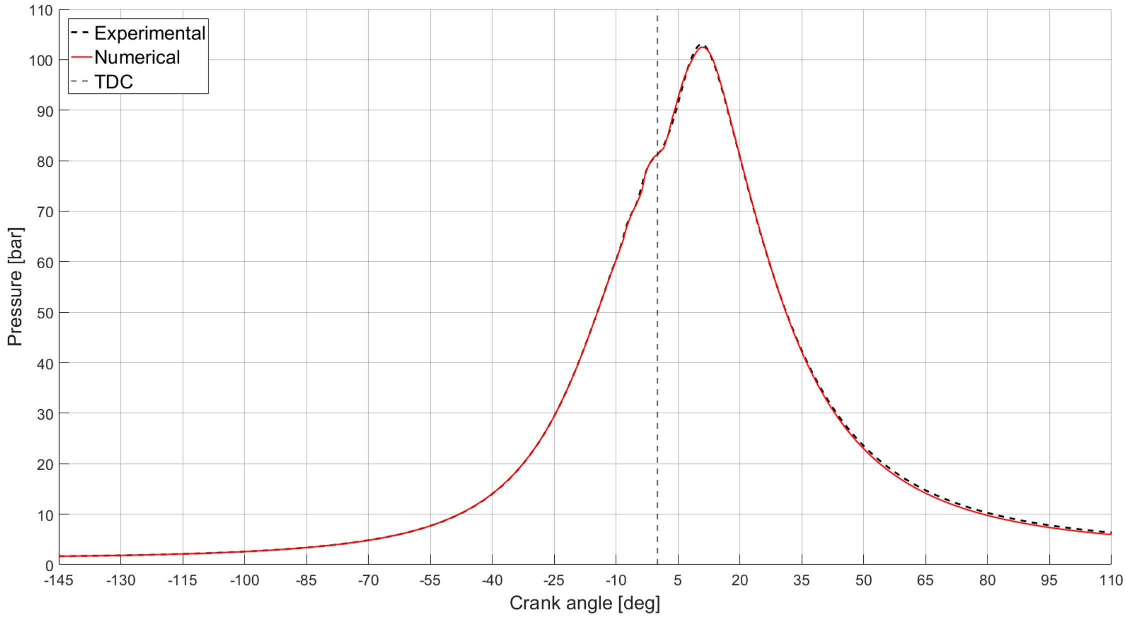

Figure 5-13 In-cylinder pressure for CFD model validation at part load

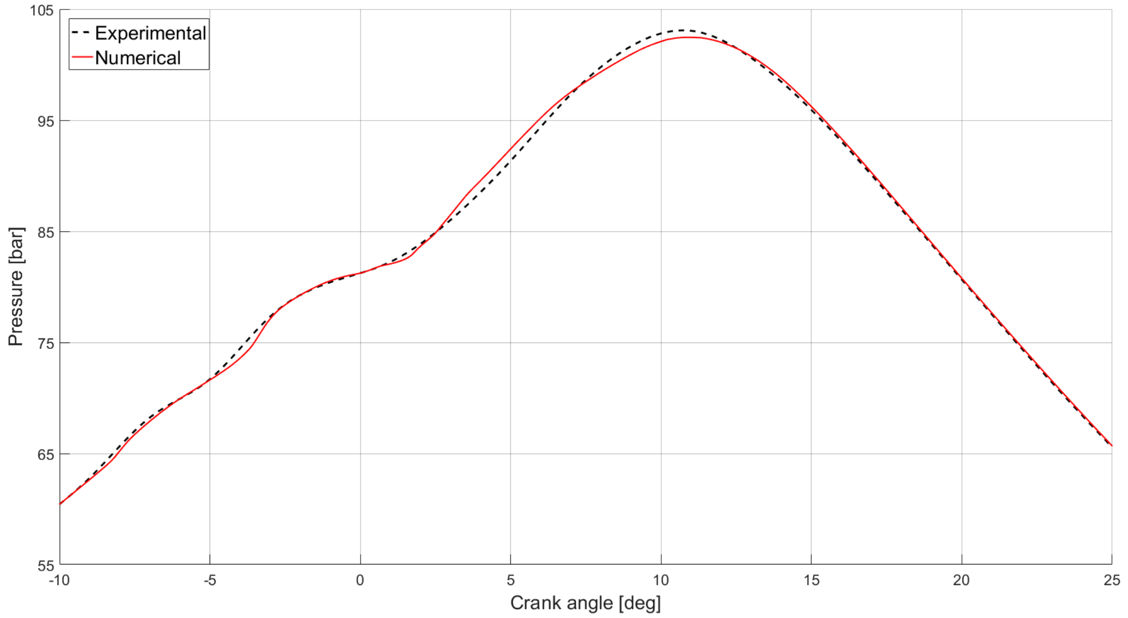

Figure 5-14 In-cylinder pressure near TDC for CFD model validation at part load

The same as at full load, Figure 5-13 shows that the compression line is matched perfectly. However, the peak firing pressure is slightly underpredicted (the maximum difference is less than 0.6 %). Also, the simulation predicts more intensive premixed burn, indicated by steeper pressure rise from 2 CAD to 7 CAD. Finally, the pressure near EVO is underestimated as at full load case, the maximum difference being only 0.38 bar.

Looking closer at pressure curves near TDC (Figure 5-14), the combustion of pilots seems to start later for numerical simulation. This trend was visible also at full load, and it was associated with the uncertainty of SOI timing. However, also modeling of spray and combustion may have an influence, impacting ignition delay and other parameters.

Heat release rate and integrated heat release at part load are shown in Figure 5-15 and Figure 5-16, respectively.

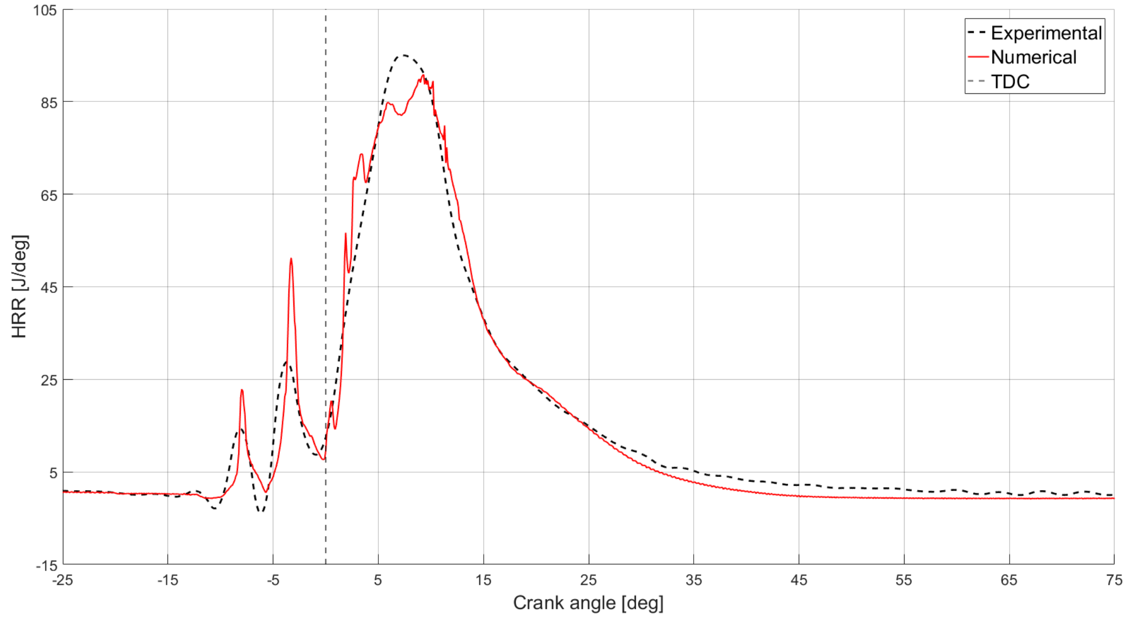

Figure 5-15 HRR for CFD model validation at part load

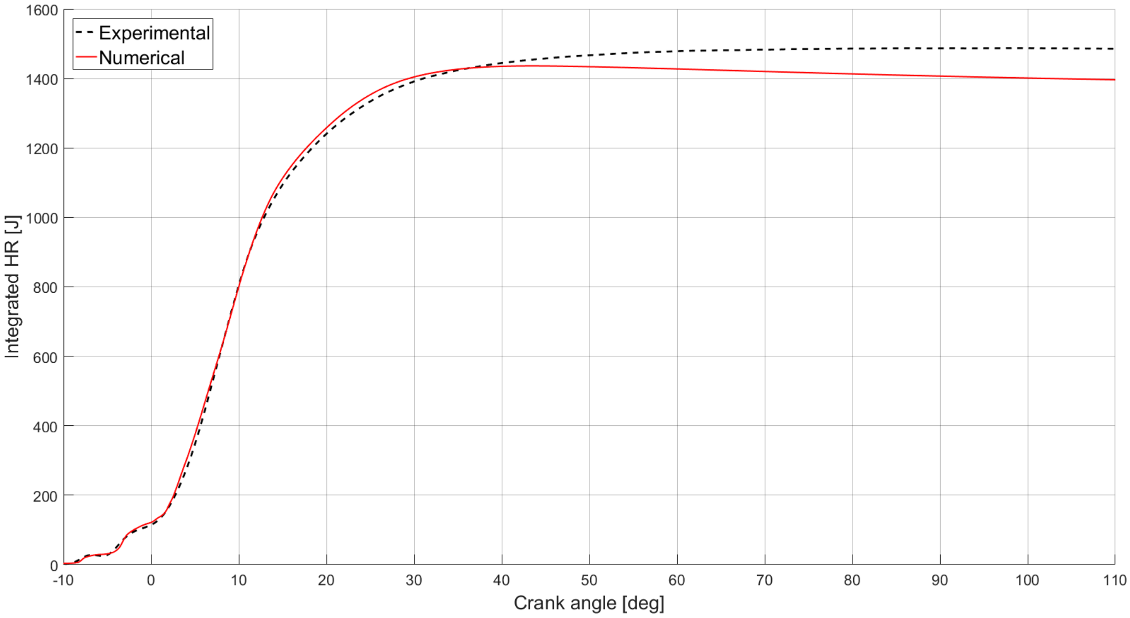

Figure 5-16 Integrated HR for CFD model validation at part load

The shape of experimental HRR is estimated correctly by the CFD model, as can be seen in Figure 5-15. However, as mentioned before, the combustion of pilots is slightly delayed (for both P1 and P2), and HRR peaks for both events are higher than in the experimental data. Increased HRR may be related to the longer ignition delay, enabling more fuel to accumulate prior to the start of combustion. Interestingly, at part load this behavior is more pronounced than at full load (see Figure 5-9 for reference). Additionally, the premixed phase is more intensive (between 0 CAD and 5 CAD), but the peak firing pressure is still underestimated as discussed previously. The reason is underestimated HRR during the mixing controlled combustion between 5 CAD and 10 CAD.

Finally, Figure 5-16 shows good matching between the experimental and numerical curves, with the latter indicating slightly faster combustion, the same as at full load.

Figure 5-17 and Figure 5-18 show curves representing NOx and soot mass within the cylinder over the simulation, respectively. The trend is the same as at full load, with NOx emissions being overestimated, and soot – underestimated. However, at part load the prediction seems less accurate, with bigger differences between experimental and numerical values.

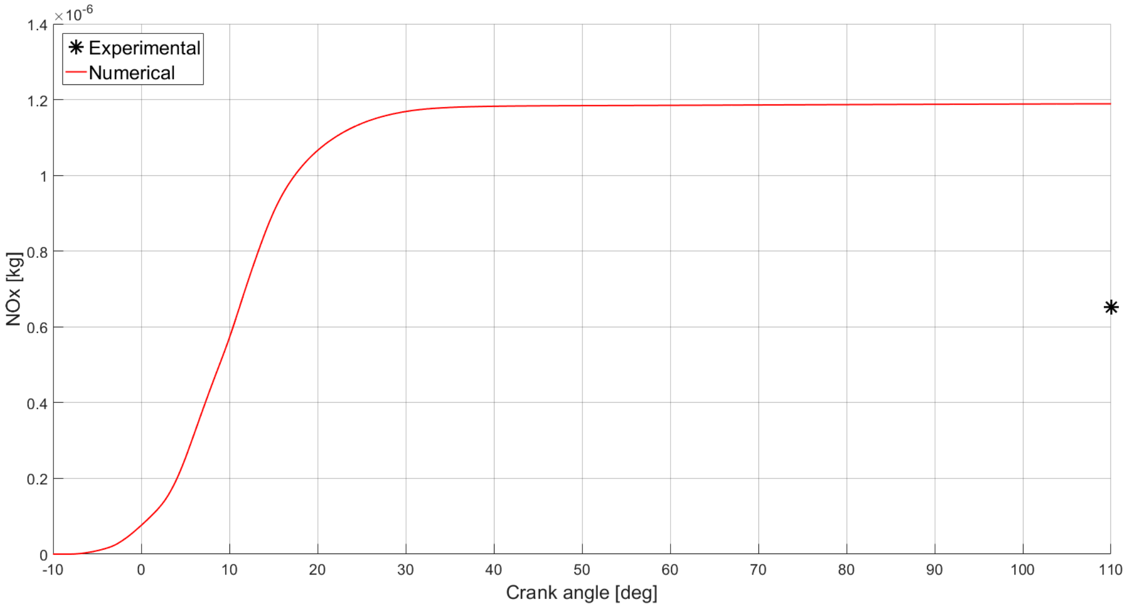

Figure 5-17 NOx mass for CFD model validation at part load

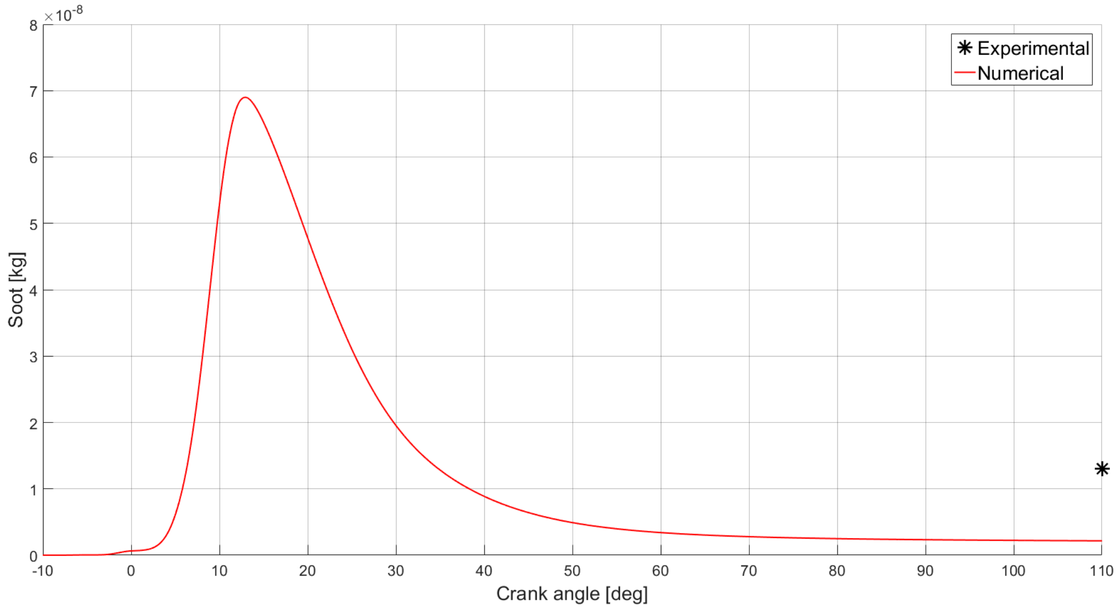

Figure 5-18 Soot mass for CFD model validation at part load

6 Results of Sensitivity Analysis

Having calibrated CFD models for two operating points of the engine enables to investigate influence of CFD, engine, and physical parameters on diesel injection and combustion processes. In this thesis, the sensitivity analysis is done for the following parameters:

1. Mesh size, which has an important influence on accuracy of results and computational cost.
2. Initial swirl ratio (SR) after intake valve closure (IVC), which influences mixing of air and fuel, further impacting combustion process.
3. Turbulent Schmidt number, which in CONVERGE CFD software impacts diffusion terms for transport equations of species and passives, so air-fuel mixing rate.

Sensitivity analysis means trying several different values of a parameter to understand importance, linearity and limits of this parameter on investigated processes. Also, taking into account simplifications accepted in setting up the case setups (as described in Chapters 4 and 5), the sensitivity analysis is useful for finding more accurate values of certain parameters while trying to better match experimental and computational results.

6.1 Mesh Size Sensitivity Analysis

The size of the mesh used for CFD computation has an important influence on two aspects:

1. Accuracy of results: the discretization of the space in order to solve governing equations is the fundamental approximation imposed by CFD (see Sections 3.3, 4.1 and 4.3). Usually, the smaller mesh size enables to better approximate simulated processes, providing more accurate results. Some exceptions are present in the spray simulation (see Section 4.3.4).
2. Computational cost: decreasing the mesh size increases the number of computational cells, meaning that more equations will be needed to solve. This can highly increase the time required to finish a simulation. Thus, lowering of the mesh size is limited by the computational power and time available.

For mesh sensitivity analyses done in this thesis, following settings were varied for different cases of two operating points of the engine:

1. Adaptive mesh refinement scale for temperature, velocity and species.
2. Fixed embedding scale for nozzle.
3. Parcels collision mesh adaptive mesh refinement scale.

It has to be noted that changing grid size, also number of injected parcels has to be changed: increasing refinement scale by 1, number of parcels has to be increased by 4. As injected fuel mass is kept constant, changing the number of injected parcels changes their mass, thus changing the number of droplets contained in each parcel.

Keeping the total number of injected parcels over the injection duration constant while refining the mesh around a spray can result in the undesirable behavior of ever increasing liquid penetration from successive refinements of the mesh. When the mass in a cell is small compared to the mass of a parcel, the amount of momentum in the liquid is enough to quickly bring the cell's velocity up to the liquid velocity. As a result, there is minimal or no drag on the parcel's drops outside of the core of the spray, resulting in excessive penetration. To remedy this issue, the injected number of parcels is increased as the embed scale is increased [46].

6.1.1 Influence on Computation

The main data and results of the mesh sensitivity analysis at full load (o. p. 2000 [rev/min] x 18 [bar]) are presented in Table 6.1. Calibration of the base case was presented in Section 5.5.

Table 6.1 Data for mesh sensitivity analysis at full load

	Coarse Mesh	Base Mesh	Fine Mesh
Base grid size, mm	1.0	1.0	1.0
Min. grid size, mm	0.5 (refinement scale 1)	0.25 (refinement scale 2)	0.125 (refinement scale 3)
Max. number of cells	264 934	538 555 (+103 %)	1 887 290 (+612 %)
Computational time	27 h 58 min	69 h 10 min (+147 %)	455 h 18 min (+1528 %)

As can be seen from the presented data, increase in the refinement scale has a big impact on the maximum number of cells and computational time. However, the increase is not linear, as number of cells increases more than twofold changing the refinement scale from 1 to 2, and more than 7 times changing from 2 to 3.

Increase in the computational time is even bigger: more than 2 times and more than 16 times changing from 1 to 2 and from 2 to 3, respectively.

The same comparison at part load (o. p. 2000 [rev/min] x 9 [bar]) is given in Table 6.2.

Table 6.2 Data for mesh sensitivity analysis at part load

	Coarse Mesh	Base Mesh	Fine Mesh
Base grid size, mm	1.0	1.0	1.0
Min. grid size, mm	0.5 (refinement scale 1)	0.25 (refinement scale 2)	0.125 (refinement scale 3)
Max. number of cells	251 783	439 942 (+74.7 %)	1 615 120 (+542 %)
Computational time	10 h 34 min	56 h 1 min (+430 %)	215 h 34 min (+1940 %)

Increase in the number of cells follows the same trend as at full load. However, increase in the computational time is even more pronounced when comparing simulations with the base and the coarse meshes.

In conclusion, running highly refined meshes imposes high requirements for the computational power. If limited resources are present, the computational time may be highly increased: the simulation with the fine mesh at full load run for 19 days, as can be seen from data provided in Table 6.1. In most applications, when multiple simulations are necessary for research and development activities, the computational cost like that would be unacceptable. Thus, it is necessary to understand to what extent results are impacted in terms of accuracy by running simulations with less refined computational grids.

6.1.2 Influence on Injection Process

Fine mesh has two effects on the simulation of the injection process:

1. Computational cells are smaller: the spray is better resolved and the liquid-gas relative velocity is better approximated.
2. Mass of injected parcels is reduced, while number increased, as explained in Section 6.1.
3. As a reacting spray is evaluated, the combustion process is also affected by the grid resolution, further impacting the spray evolution over time.

Liquid and vapor penetrations at full load conditions (o. p. 2000 [rev/min] x 18 [bar]) are shown in Figure 6-1.

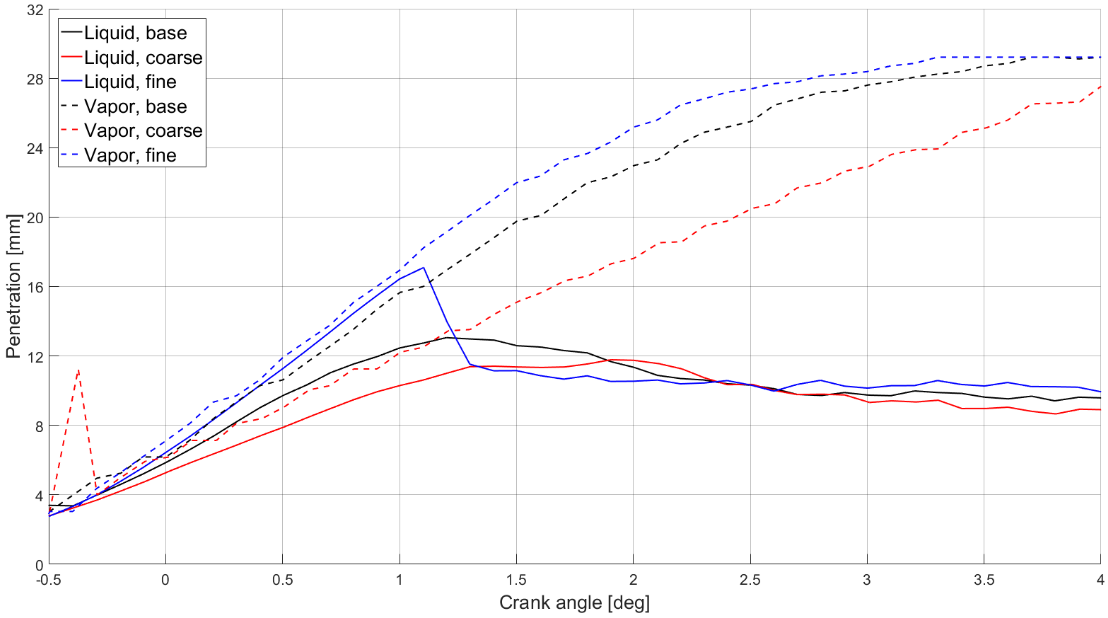

Figure 6-1 Liquid and vapor penetrations for different mesh sizes at full load

Increasing the mesh refinement, the initial penetration of the liquid spray increases, while grid convergence is achieved for a quasi-steady liquid length for all three mesh sizes from 2.5 CAD.

An under-resolved velocity field (coarse mesh) results in an overprediction of the liquid-gas relative velocity, which in turn produces excessive drag and drop breakup. This leads to an underprediction of the near-nozzle penetration as shown in Figure 6-1 (from -0.5 CAD to about 1 CAD). On the other hand, as the cell size is decreased, the gas-phase velocity near the nozzle increases, resulting in lower relative velocities and less drag [46]. When the combustion starts, the liquid penetration drops because of the combustion heating and following more intense evaporation (see Section 2.4), and reaches the quasi-steady liquid length.

In addition to liquid penetrations, fuel vapor penetrations are also available for comparison and are shown in Figure 6-1. It is clear that reducing the mesh size increases the initial vapor penetration. For simulations with the base and the fine grids, the penetration reaches the same steady-state value from about 3.7 CAD.

To measure the liquid penetration, CONVERGE first calculates the total mass of the liquid parcels from the nozzle and then multiplies this mass by the liquid penetration fraction (0.95 is used in the present work) to yield the penetrated spray mass. Starting from the center of the nozzle hole, CONVERGE sums the mass of the liquid parcels until it reaches the penetrated spray mass. This distance is the liquid penetration [24].

Figure 6-2 shows the spray penetration for the fine mesh from 0.5 CAD to 2 CAD. Parcels differ in size and color depending on their radius and temperature, respectively. The surrounding colors represent the in-cylinder temperature across the given slice. At 0.5 CAD, the initial stage of main injection event happens, with big parcels near the nozzle (see Section 4.6.2), and ever smaller parcels downstream due to the break-up and evaporation. Smallest parcels far away from the nozzle are remains from the previous injection event (the second pilot). There is small heat release (indicated by higher temperature) near the nozzle, which is part of the heat released during the combustion of the second pilot. At 1 CAD the spray penetrates further and HRR seems to cover the periphery of the spray, although intensity remains low. Then, between 1.1 CAD and 1.3 CAD, the temperature increases all around downstream portion of the spray (see also Figure 6-4 for the heat release rate). Parcels that are furthest from the nozzle decrease in size as a result of increased vaporization due to the combustion heating, and more liquid mass becomes concentrated closer to the nozzle. Thus, the liquid length, as calculated by CONVERGE, reduces (this can be seen also in Figure 6-1). From then on, as shown in schematics at 1.5 CAD and 2 CAD, the liquid penetration stays at the quasi-steady length, while the combustion (the diffusion flame) covers the spray.

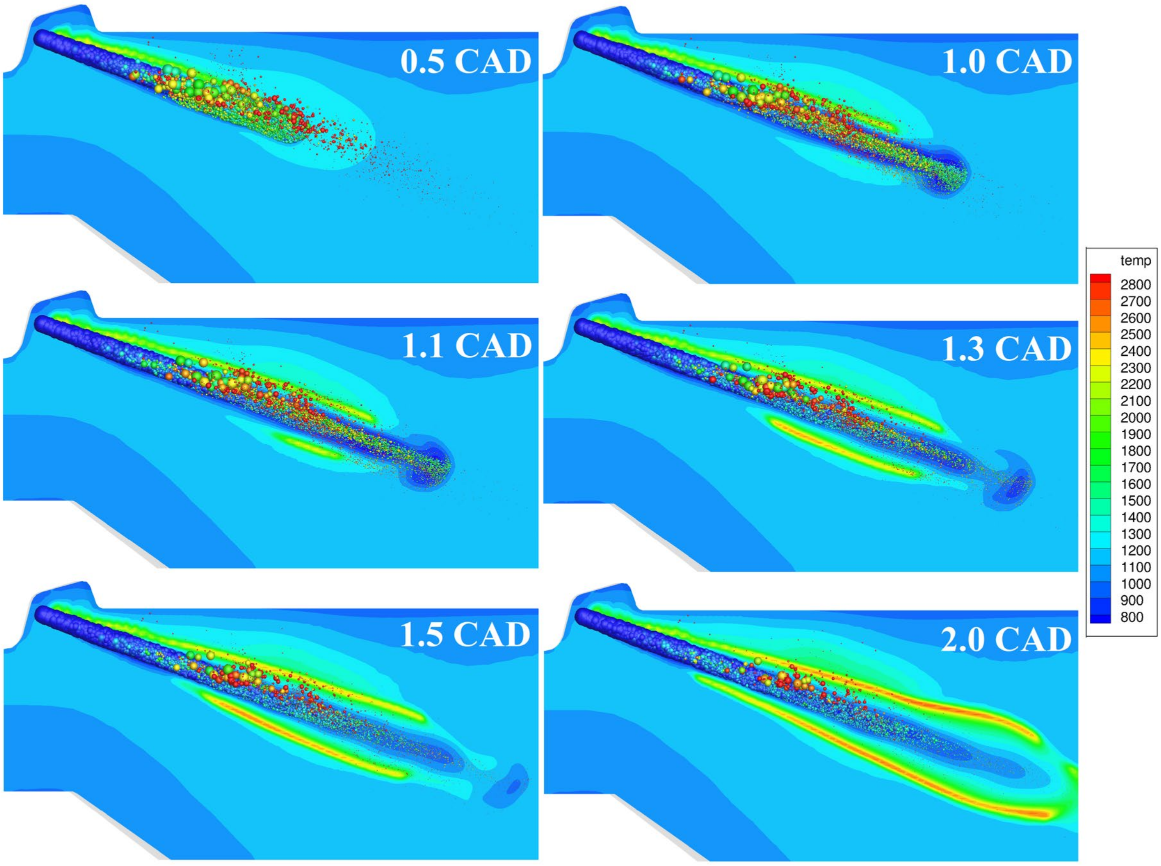

Figure 6-2 Liquid penetration time history for fine mesh at full load

Figure 6-3 shows a comparison of sprays for the base and coarse meshes. Compared with schematics for the fine mesh, the temperature around the spray is higher for both coarse and fine meshes already at 1 CAD, indicating earlier start of HRR (see also Figure 6-4). The reason may be lower penetration and smaller amount of parcels, which impede evaporation and don't take as much heat from the surroundings. Thus, together with excessive drag and drop breakup mentioned earlier, also the increased heating during the initial phase of injection contributes to reduced liquid penetration for the coarse mesh. However, maximum temperatures at 1.5 CAD and 2 CAD are higher for the fine mesh, as improved air entrainment enhances the premixed burn.

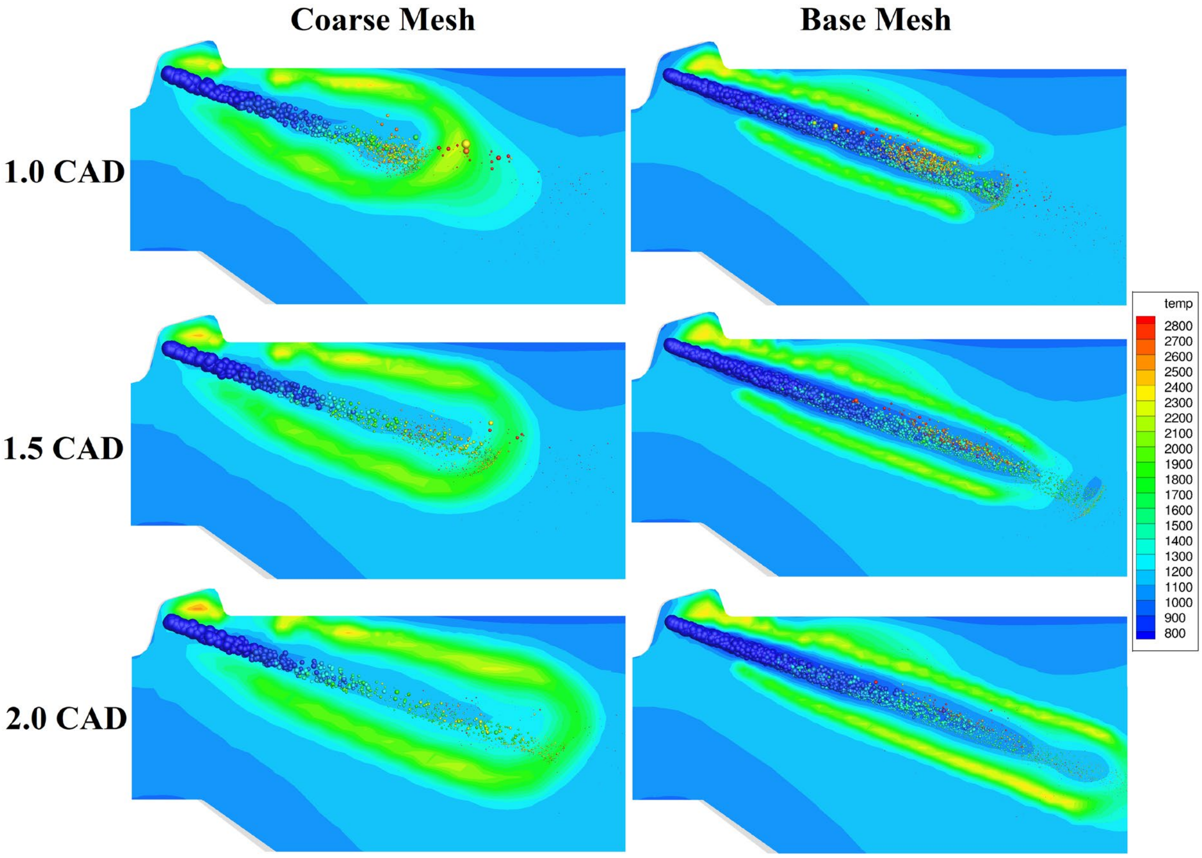

Figure 6-3 Liquid penetration time history for coarse and base meshes at full load

Liquid and vapor penetrations at part load conditions (o. p. 2000 [rev/min] x 9 [bar]) are shown in Figure 6-4. Results correspond to those obtained at full load and explained above.

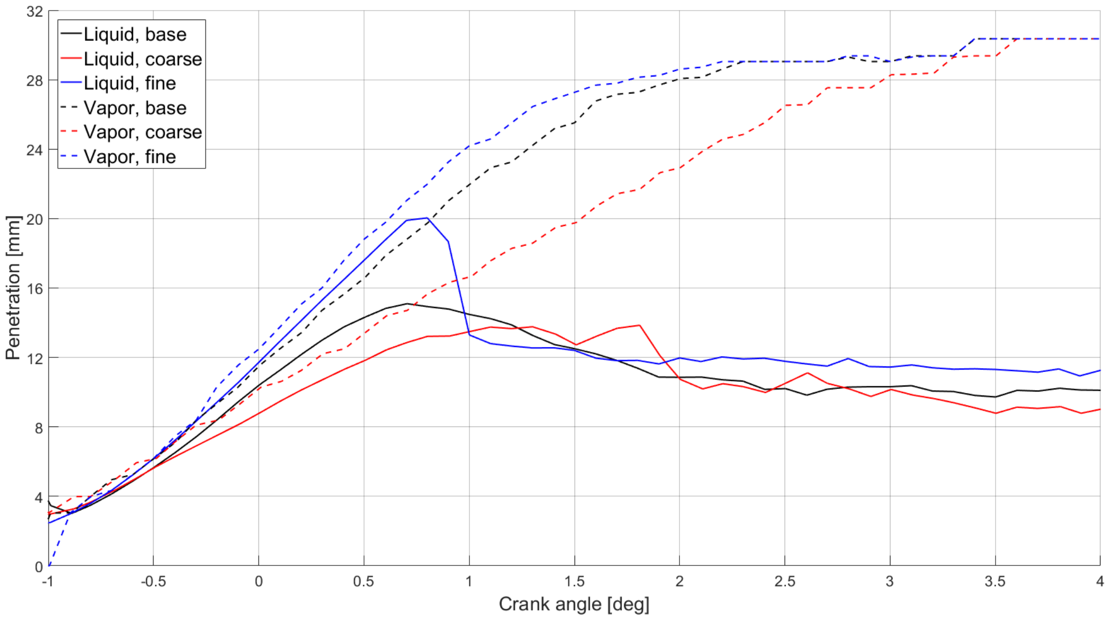

Figure 6-4 Liquid and vapor penetrations for different mesh sizes at part load

6.1.3 Influence on Combustion Process

In-cylinder pressure and heat release rate at full load (o. p. 2000 [rev/min] x 18 [bar]) are shown in Figure 6-5.

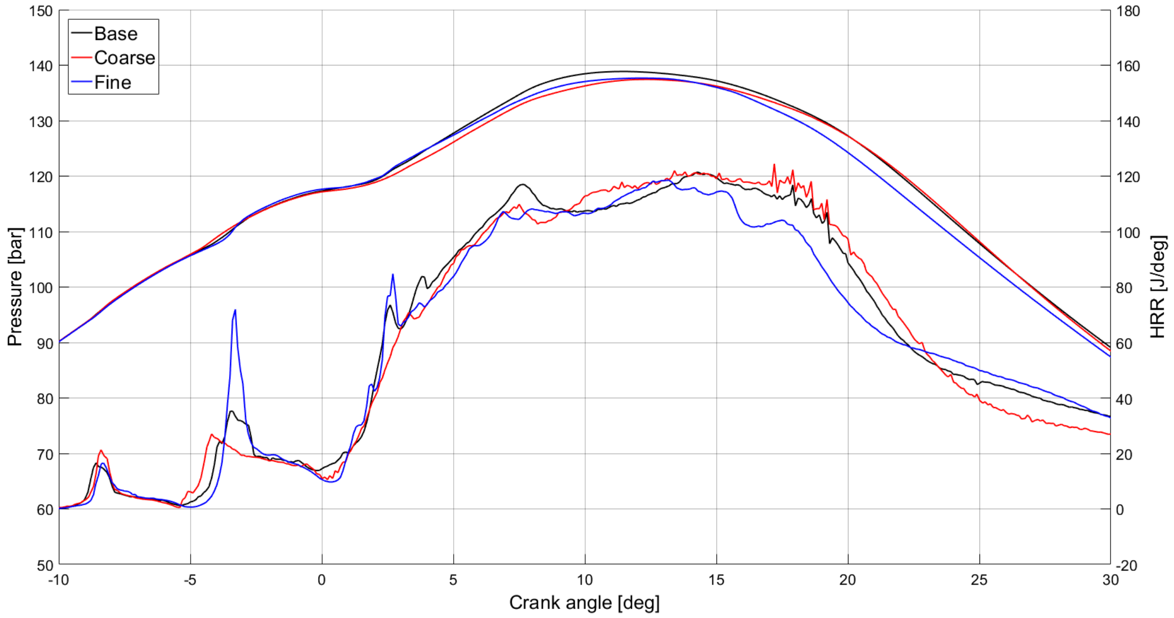

Figure 6-5 In-cylinder pressure and HRR for mesh sensitivity analysis at full load

Increasing the mesh refinement, the heat release rate during the combustion of the second pilot and the premixed phase is increased, as a result of improved air-fuel mixing process.

Compared with the base case, the simulation with the coarse mesh shows less pronounced combustion of the second pilot (from -4 CAD to 0 CAD), and lower premixed burn (from 0 CAD to about 3 CAD). This is expected, taking into account analysis done in Section 6.1.2: the coarse mesh underpredicts the near-nozzle penetration of the liquid fuel, providing less area for air entrainment, thus impeding the air-fuel mixing process. Less fuel is within combustible limits at the start of combustion of the second pilot, as well as at the start of combustion of the main event. Finally, the in-cylinder pressure rise is smaller, and lower peak firing pressure is achieved for the coarse mesh. Also, it should be considered that reducing the mesh size, the number of injected parcels is increased, while mass of injected fuel remains unchanged. Thus, more parcels are available, evaporation of the liquid fuel is enhanced, and more mixture is available at the time of start of combustion. This effect may complement that of the longer liquid length.

For the fine mesh, the heat release rate of the second pilot is the highest of all cases, while the premixed burn is comparable with that of the base mesh. The early part of the mixing-controlled combustion (from 3 CAD to 13 CAD) is less intense than for the simulation with the base case, resulting in lower peak firing pressure. During the late part of the mixing-controlled combustion, HRR shows a visible drop at about 13 CAD.

Enhanced evaporation of fuel parcels takes more energy from the surrounding gas, resulting in locally cooler gas temperatures and later ignition. This is especially visible in the timing of start of heat release of the second pilot combustion in Figure 6-5.

The heat release rate during the combustion of the first pilot injection is influenced the least by the mesh size. The reason may be related to a small amount of fuel injected during this event.

Figure 6-6 and Figure 6-7 show comparison of temperature distributions and sprays at 3 CAD before top dead center (BTDC) at full load for coarse-base, and base-fine meshes, respectively. 3 degrees BTDC is a timing near the maximum heat release rate of the second pilot combustion.

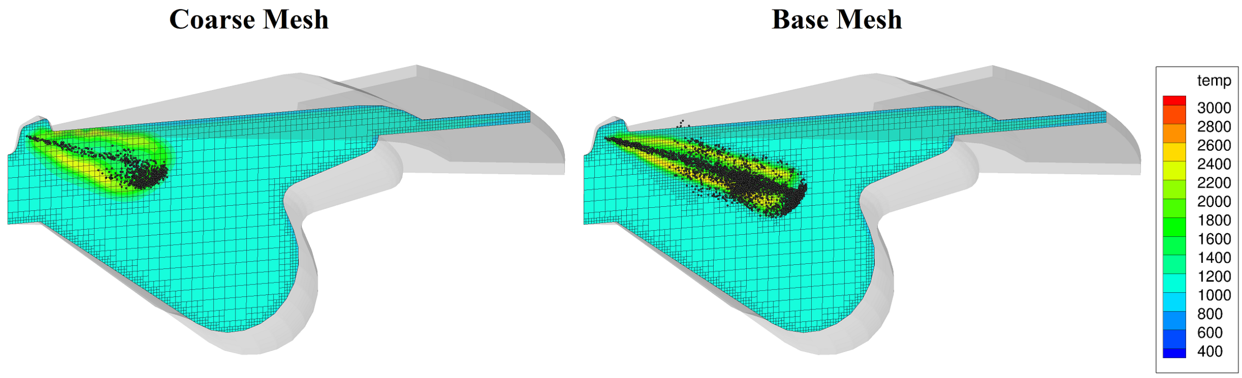

Figure 6-6 Temperature distribution and scatter of parcels for coarse and base meshes

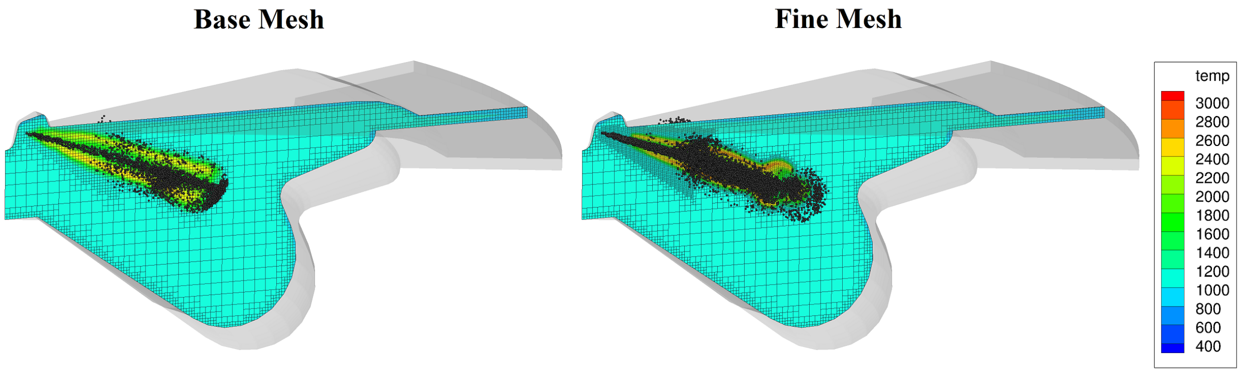

Figure 6-7 Temperature distribution and scatter of parcels for base and fine meshes

Figure 6-6 shows a big difference in penetration of parcels, which matches the previous explanation. Accordingly, for the coarse mesh the volume in which the combustion happens (here only a slice is shown) is smaller, less heat is released. In opposite, Figure 6-7 shows a higher penetration of parcels for the fine mesh. Also, the difference between density of parcels (or number of parcels) is visible in both figures.

Quantitative comparisons between different mesh sizes at full load (o. p. 2000 [rev/min] x 18 [bar]) are provided in Table 6.3 in terms of combustion progress, i.e., peak firing pressure, crank angle location for the peak firing pressure, MFB50 (CA corresponding to 50 % of the total heat release), and MFB10-MFB90 (CA corresponding to distance between 10 % and 90 % of the total heat release). Percentage differences relative to the base case for all parameters are also included.

Table 6.3 Comparison of combustion progress for different mesh sizes at full load

Mesh	Peak Firing Pressure	CA at Peak Firing Pressure	MFB50	MFB10-MFB90
	bar	deg	deg	deg
Base	138.9	11.4	15.3	28.5
Coarse	137.4 (-1.08 %)	12.4 (+8.60 %)	15.6 (+2.43 %)	32.3 (+13.4 %)
Fine	137.8 (-0.79 %)	12.1 (+5.96 %)	15.3 (–)	30.1 (+5.87 %)

There are no big differences in terms of peak firing pressures and MFB50 timings. However, the location of peak firing pressure and the combustion duration (MFB10-MFB90) are more impacted by the mesh resolution. Also, the simulation with the coarse mesh shows bigger differences compared with the base case than the simulation with the fine mesh.

In-cylinder pressure and heat release rate at part load (o. p. 2000 [rev/min] x 9 [bar]) are shown in Figure 6-8.

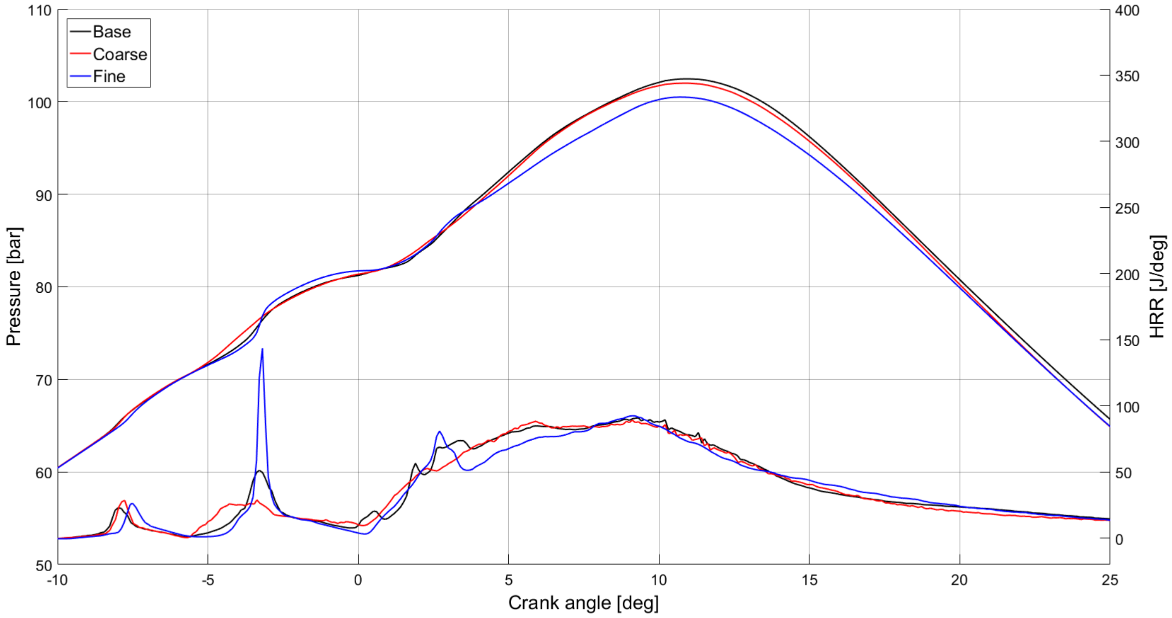

Figure 6-8 In-cylinder pressure and HRR for mesh sensitivity analysis of case at part load

Same as at full load, HRR of the second pilot combustion (between -4 CAD and -2 CAD) and of the premixed phase (from 0 CAD to 3 CAD) is higher for the fine mesh and lower for the coarse mesh (compared with the base case). Then, the early part of the mixing-controlled combustion (from 3 CAD to 7.5 CAD) is less intense for the fine mesh, which results in slower pressure rise and lower peak firing pressure. However, differently than at full load, later parts (from about 7.5 CAD) of heat release curves are converging to one line for all three cases.

Quantitative comparisons between different mesh sizes at part load (o. p. 2000 [rev/min] x 9 [bar]) are provided in Table 6.4 in terms of combustion progress, i.e., peak firing pressure, crank angle location for the peak firing pressure, MFB50, and MFB10-MFB90.

Table 6.4 Comparison of combustion progress for different mesh sizes at part load

Mesh	Peak Firing Pressure	CA at Peak Firing Pressure	MFB50	MFB10-MFB90
	bar	deg	deg	deg
Base	102.5	10.9	9.88	22.7
Coarse	102.0 (-0.49 %)	10.9 (–)	10.1 (+2.23 %)	26.7 (+18.0 %)
Fine	100.5 (-1.95 %)	10.7 (-1.83 %)	10.2 (+3.24 %)	23.9 (+5.47 %)

In opposite to analysis done for simulations at full load, results given in Table 6.4 indicate smaller impact of the mesh size on the location of peak firing pressure at part load. The combustion duration parameter (MFB10-MFB90) remains the most sensitive to the grid resolution.

Also, while at full load the simulation with the fine mesh showed smaller differences (compared with the base case) than the simulation with the coarse mesh, at part load situation is reversed (except in the case of combustion duration parameter).

6.1.4 Influence on Pollutant Emissions

Figure 6-9 shows curves representing NOx mass within the cylinder for different mesh sizes at full load (o. p. 2000 [rev/min] x 18 [bar]).

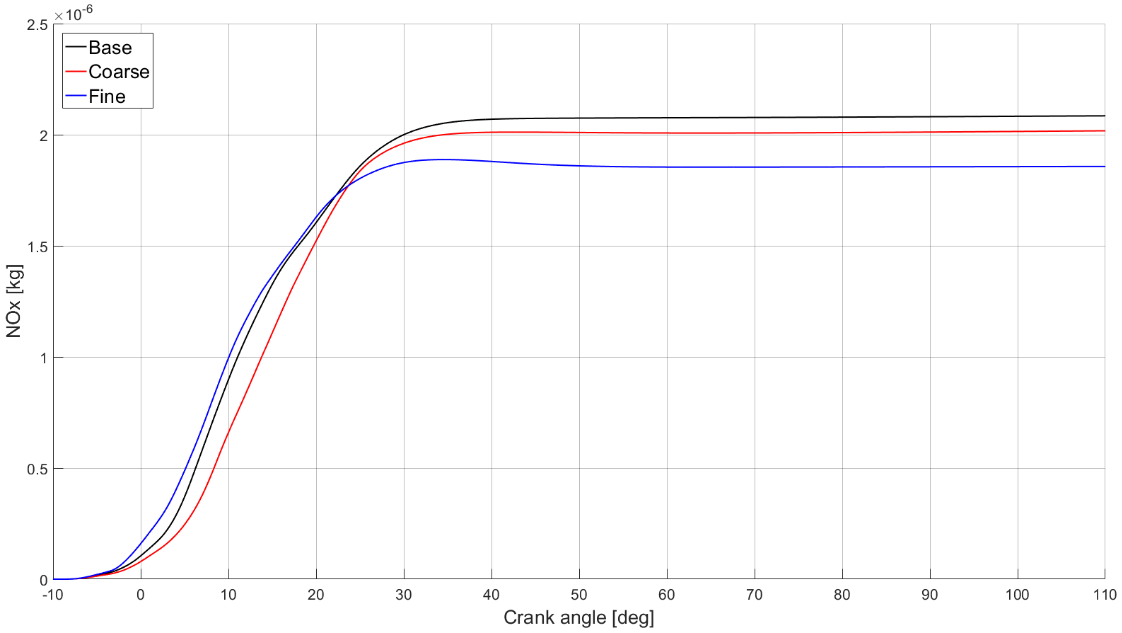

Figure 6-9 NOx emissions for mesh sensitivity analysis at full load

The simulation with the fine mesh shows more intense combustion of the second pilot and the premixed phase (see Figure 6-5), so the initial production of NOx is higher than for the base case. When intensity of the mixing-controlled combustion drops (at 13 CAD), production of NOx falls accordingly. The peak firing pressure and the heat release rate during the mixing-controlled combustion are higher for the base case (producing higher mean in-cylinder temperature, as shown in Figure 6-10; temperature is highly important for NOx production as explained in Section 2.5), and so is the final emitted value of NOx.

For the coarse mesh, HRR during the premixed and early mixing-controlled combustion phases is lower, making initial NOx production slower. During the late part of mixing-controlled combustion, production rate of NOx becomes higher than for both other cases (slope does not decrease at about 15 CAD in Figure 6-9). However, as the mean temperature drops (see Figure 6-10) and the expansion stroke is well underway, production of NOx freezes and emitted value remains lower than for the base case.

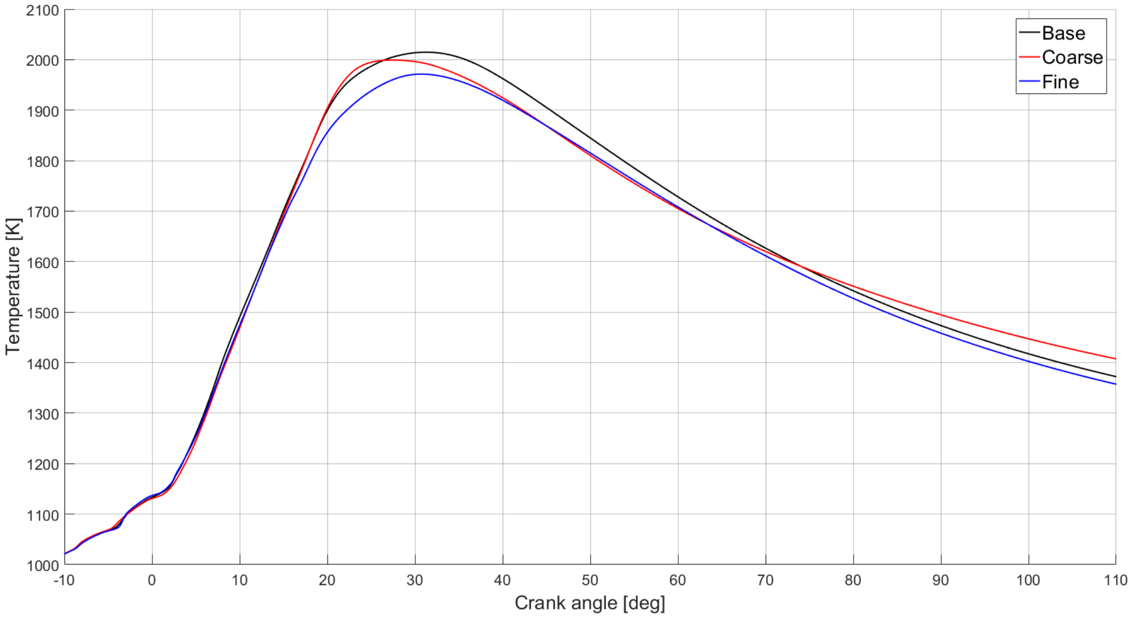

Figure 6-10 Mean in-cylinder temperature for mesh sensitivity analysis at full load

Figure 6-11 shows curves representing NOx mass within the cylinder for different mesh sizes at part load (o. p. 2000 [rev/min] x 9 [bar]).

In opposite to the situation at full load, NOx emissions for the fine mesh are marginally higher than for the coarse mesh. The reason is that the late part of HRR of the mixing-controlled combustion (see Figure 6-8) does not drop below that of the coarse mesh, and NOx produced due to initially more intensive burning of the second pilot is augmented enough to remain above the value achieved in the simulation with the coarse mesh. However, as the initial part of HRR during the mixing-controlled combustion is lowest in the case of the fine mesh, the final difference is small (compared with emission for the coarse mesh) and again lower than for the base case.

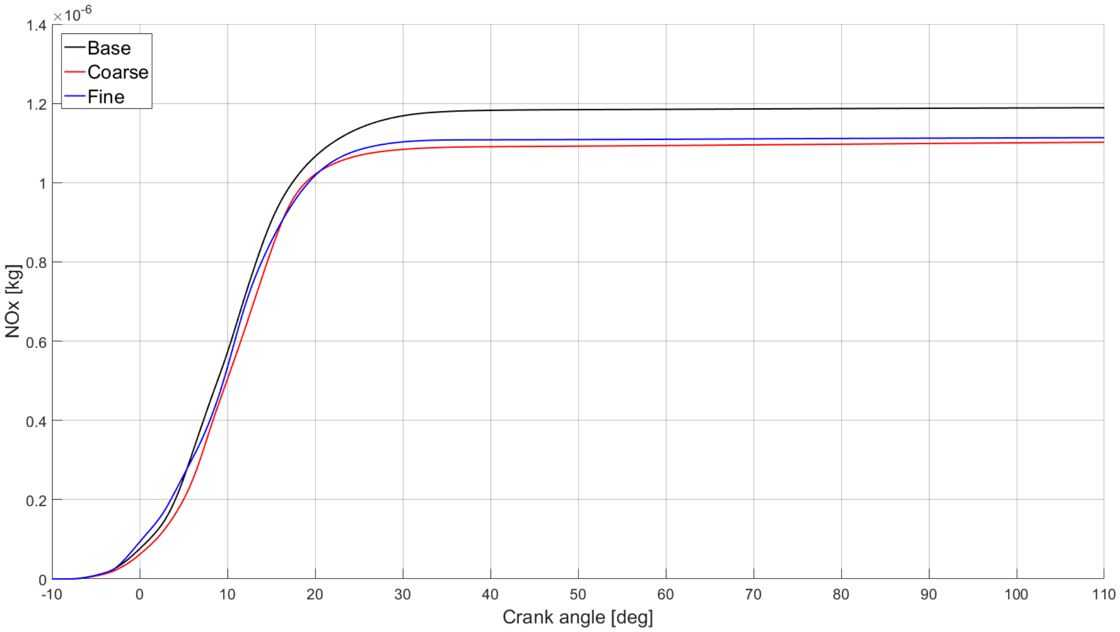

Figure 6-11 NOx emissions for mesh sensitivity analysis at part load

Figure 6-12 shows curves representing soot mass within the cylinder for different mesh sizes at full load (o. p. 2000 [rev/min] x 18 [bar]).

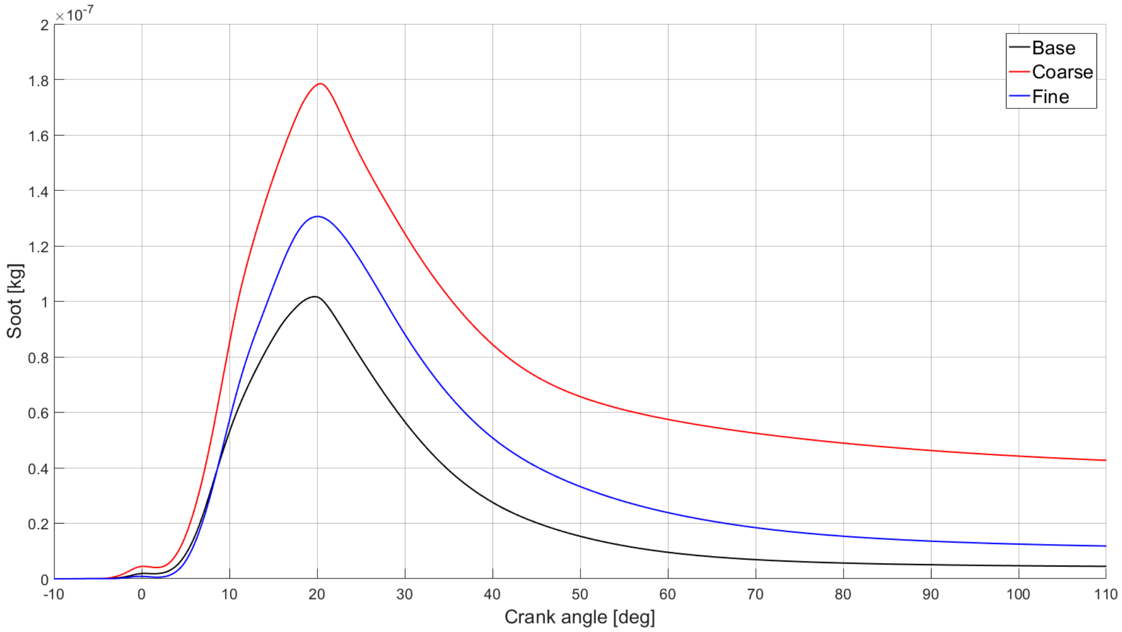

Figure 6-12 Soot emissions for mesh sensitivity analysis at full load

For the coarse mesh, lower penetration of the liquid spray impedes the evaporation, making combustion to occur at locally richer conditions, and more soot is formed early in the process than for the base case. Then, products of the rich premixed combustion burn out at the near-stoichiometric diffusion flame at the jet periphery (as explained in Section 2.5). As the heat release rates during the mixing-controlled combustion are comparable for both cases (see Figure 6-5), so are the soot oxidation processes, and the final emitted value remains higher for the simulation with the coarse mesh.

For the fine mesh, the initial soot production is lower than for the base case, as fuel is better mixed with air. Then, however, oxidation of produced soot particles is impeded, as the HRR during the mixing-controlled combustion drops faster (see Figure 6-5). As a result, the final value of emitted soot for the simulation with the fine mesh is bigger than for the base case.

Figure 6-13 shows curves representing soot mass within the cylinder for different mesh sizes at part load (o. p. 2000 [rev/min] x 9 [bar]). The trend is the same as at full load (soot emissions increase for both fine and coarse meshes) and explanation given above applies.

Quantitative comparisons between different mesh resolutions for both operating points are provided in Table 6.5 in terms of final emitted values of NOx and soot, as well as of the percentage differences relative to the base case. Also, experimental values are given for reference. Table shows that the mesh size has a bigger impact on the soot emissions than on NOx. Comparing results with experimental values, it is clear that at full load the CFD model provides more accurate results than at part load, as has been already said in Section 5.5.

At full load the fine mesh improves the estimation of NOx emissions, while at part load experimental values of both NOx and soot are better matched while using the coarse mesh.

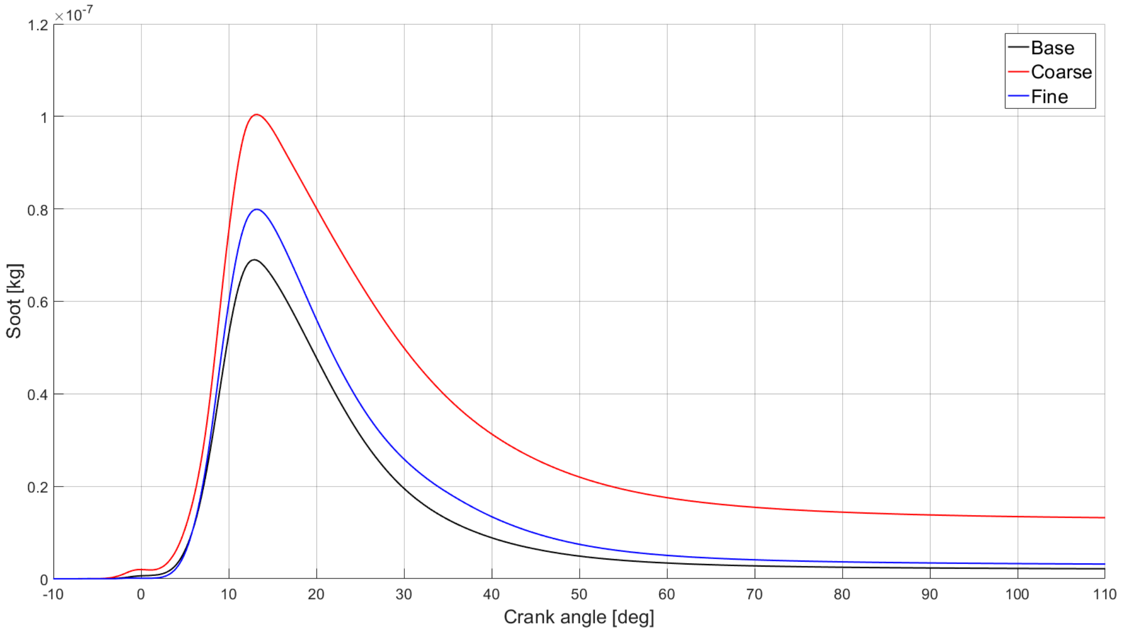

Figure 6-13 Soot emissions for mesh sensitivity analysis at part load

Table 6.5 Comparison of pollutant emissions for different mesh sizes

Mesh	NOx	Soot
	mg	µg
2000 [rev/min] x 18 [bar]		
Experimental	1.505	7.821
Base	2.085	4.483
Coarse	2.018 (-3.21 %)	42.71 (+853 %)
Fine	1.857 (-10.9 %)	11.82 (+164 %)
2000 [rev/min] x 9 [bar]		
Experimental	0.653	12.99
Base	1.189	2.169
Coarse	1.102 (-7.32 %)	13.22 (+509 %)
Fine	1.113 (-6.39 %)	3.189 (+147 %)

6.2 Swirl Ratio Sensitivity Analysis

As has been mentioned in Section 5.4.1, when the intake flow is not calculated, engine CFD simulations use a uniform swirl applied to the in-cylinder region. This approximation introduces an error, which can be significant: the swirl in diesel engines affects the mixing rate of air and fuel, the heat release rate, emissions and the overall engine performance (for explanation see Section 2.1.1). Thus, the swirl ratio (SR) sensitivity analysis is done in order to understand its effects on computational results, and usefulness for fine-tuning of the CFD model.

CONVERGE uses SR and the swirl profile (see Section 5.4.1) to set the components of the velocity in the cylinder region. SR is the ratio of the angular velocity of the flow to the angular velocity of the crankshaft:

$$\mathrm{SR} = \frac{\Omega_{\mathrm{flow}}}{\Omega_{\mathrm{crankshaft}}} \tag{6.1}$$

For both analyzed operating points of the engine, 5 levels of the initial SR are investigated (see Table 6.6): base, ±25 %, and ±50 %.

Table 6.6 Swirl ratios used for the sensitivity analysis

SR Level	2000 [rev/min] x 18 [bar]	2000 [rev/min] x 9 [bar]
Base	-1.48	-1.46
-50 %	-0.74	-0.73
-25 %	-1.11	-1.10
+25 %	-1.85	-1.83
+50 %	-2.22	-2.19

6.2.1 Influence on Injection Process

Liquid and vapor penetrations for simulations at full load (o. p. 2000 [rev/min] x 18 [bar]) are shown in Figure 6-14 and Figure 6-15, respectively.

Only a minor effect of the swirl ratio on the liquid length is visible. All curves follow the same line until about 0.5 CAD, when combustion takes place (see Figure 6-19 for the heat release rate). The quasi-steady liquid length (from about 3 CAD) is the highest for the minimum swirl ratio case, and the lowest for the maximum swirl ratio case, although difference is small. This matches the analysis given in [47], which states that the increased spray deflection (it was observed that with increase in swirl, the spray deflection increases due to increase in cross air swirl velocity) is responsible for the reduction in the spray tip chord distance.

There is no significant effect of SR on the vapor penetration, as can be seen from Figure 6-15.

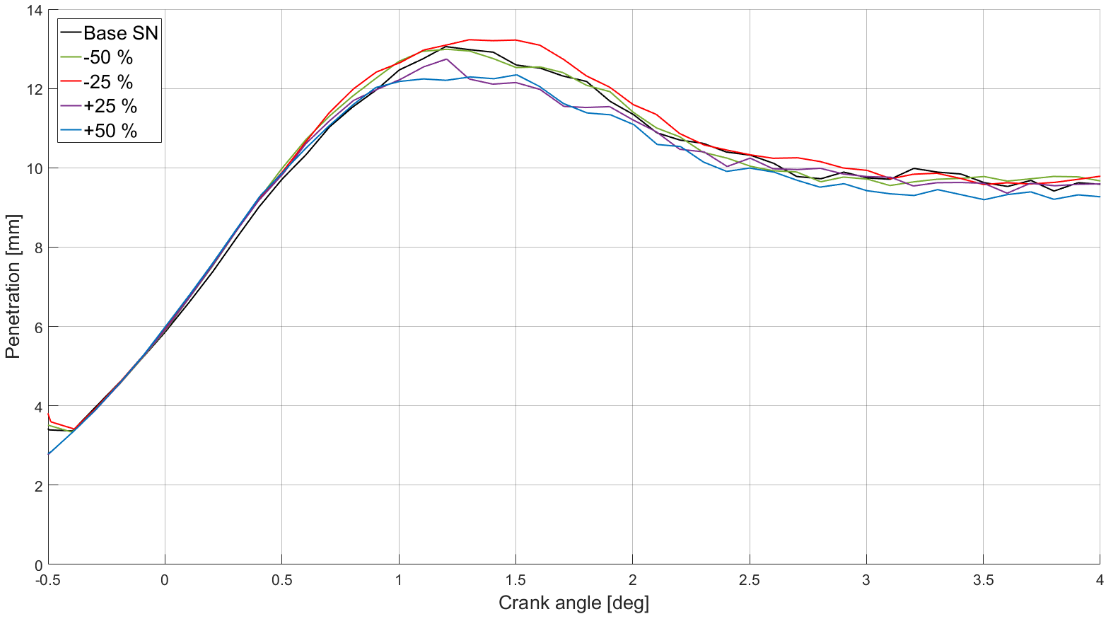

Figure 6-14 Liquid penetrations for different swirl ratios at full load

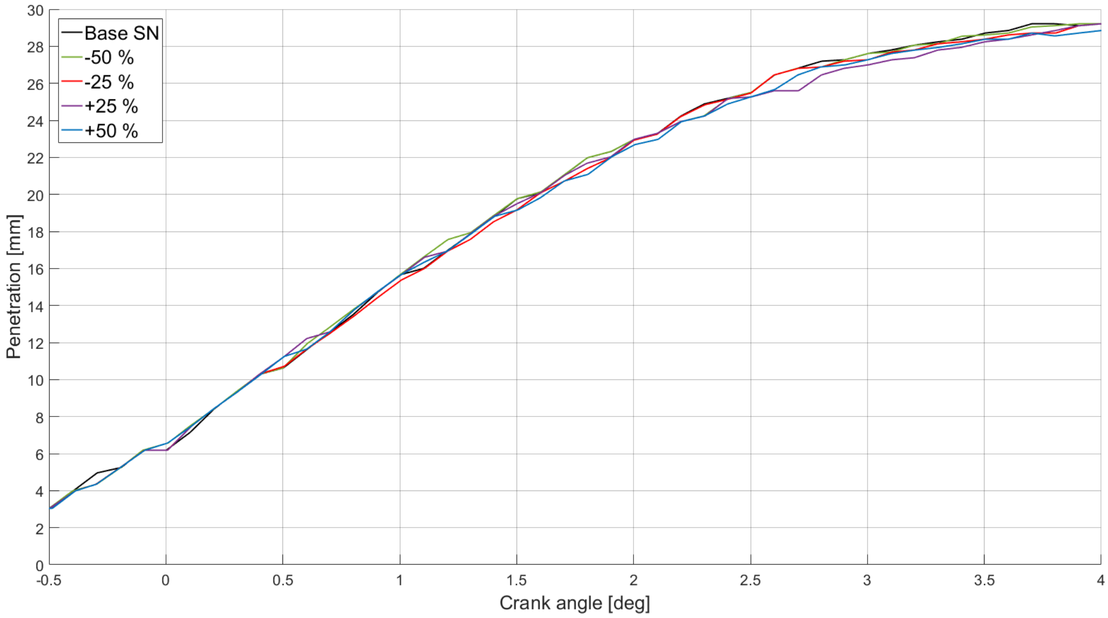

Figure 6-15 Vapor penetrations for different swirl ratios at full load

Figure 6-16 shows the shape of the spray and its deflection for different swirl ratios.

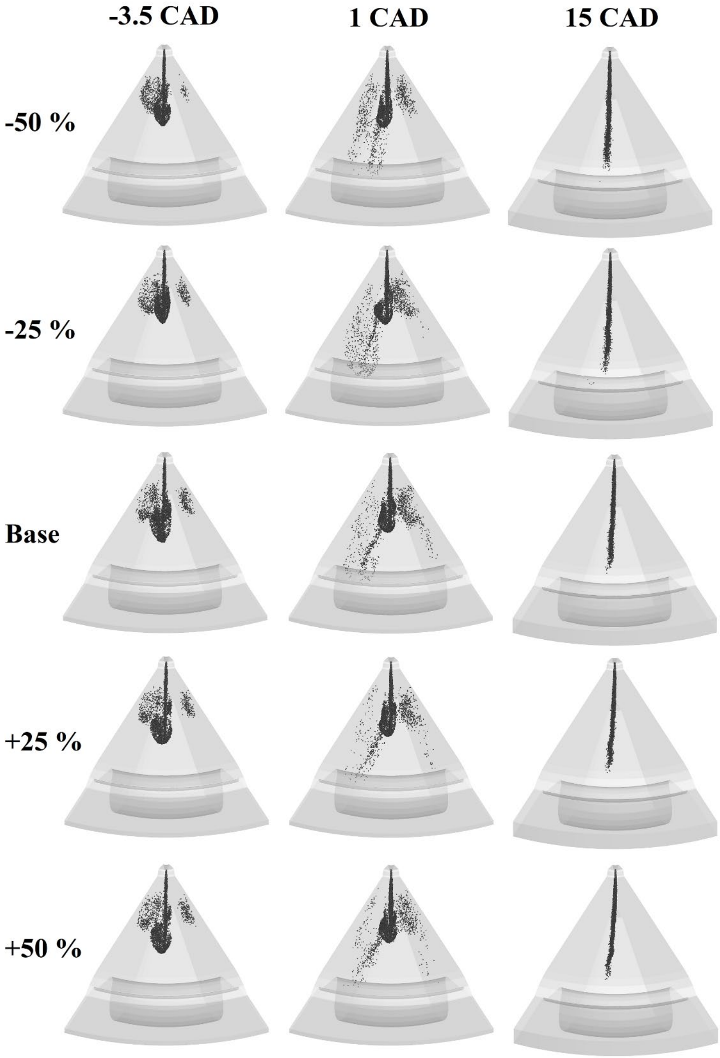

Figure 6-16 Spray shape for different swirl ratios at full load

The first timing (-3.5 CAD) is during the second pilot injection, the second timing (1 CAD) is at the early stage of the main injection, and the final timing (15 CAD) is during the steady-state part of the main injection, when the liquid spray is at the quasi-steady state length.

At all timings, the increasing deflection of the liquid spray with the increasing swirl ratio is visible. It can be best appreciated when comparing pictures of -50 % and +50 % SR values at 15 CAD. Also, when comparing the same two pictures, the liquid spray length decreased for +50 % swirl ratio value. This matches results shown in Figure 6-14, and analysis given in [47] which states that with increase in swirl, the spray deflection increases, and the reduction in the spray tip chord distance happens.

At -3.5 CAD and 1 CAD another trend can be spotted: increasing the swirl ratio, a cloud of remaining parcels of the previous injection is pushed by the charge motion to the left, thus overlapping with the cloud of newly injected parcels (in these simulations, as the sector of the cylinder is used, mass leaving through the left face in Figure 6-16 enters from the right side). Overlaps can create fuel rich zones that would significantly impact the air utilization process [11].

Liquid and vapor penetrations for simulations at part load (o. p. 2000 [rev/min] x 9 [bar]) are shown in Figure 6-17 and Figure 6-18, respectively.

Figure 6-17 shows that, same as at full load, the swirl ratio has a small effect on the liquid penetration. All curves seem to converge at the same quasi-steady liquid length of about 10 mm from 2.5 CAD.

Vapor penetration, as can be seen from Figure 6-18, is also only marginally affected by the change in the swirl ratio, as in the case of simulations at full load. However, this time there is a visible difference between 0.5 CAD and 2 CAD; vapor for simulations with the higher SR penetrates further. From 2.5 CAD, all simulations show the same vapor penetration.

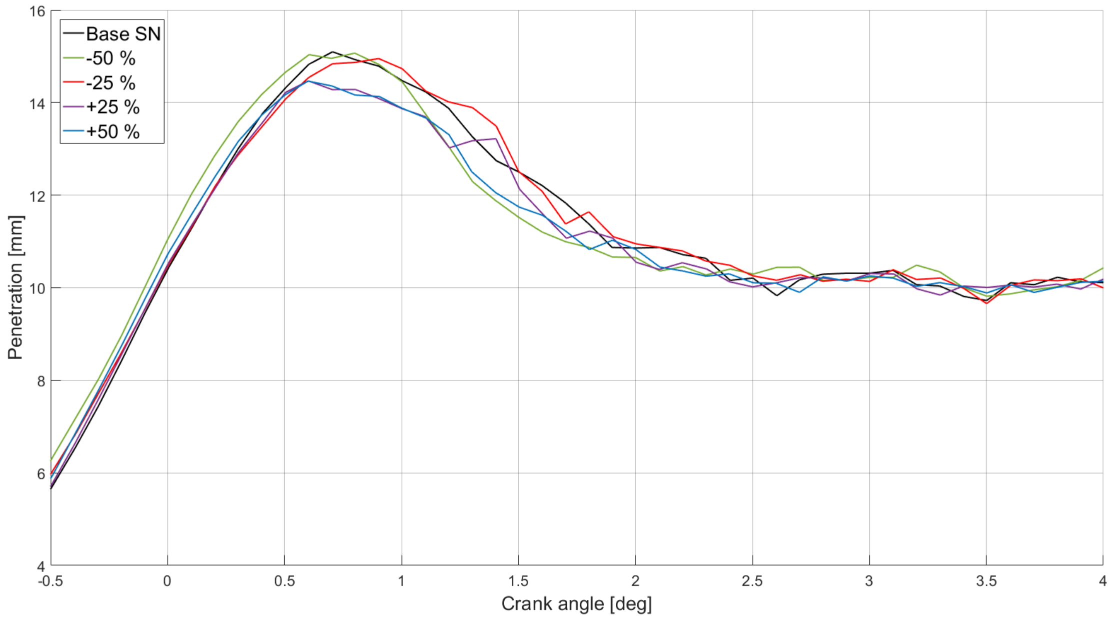

Figure 6-17 Comparison of liquid penetrations for different swirl ratios at part load

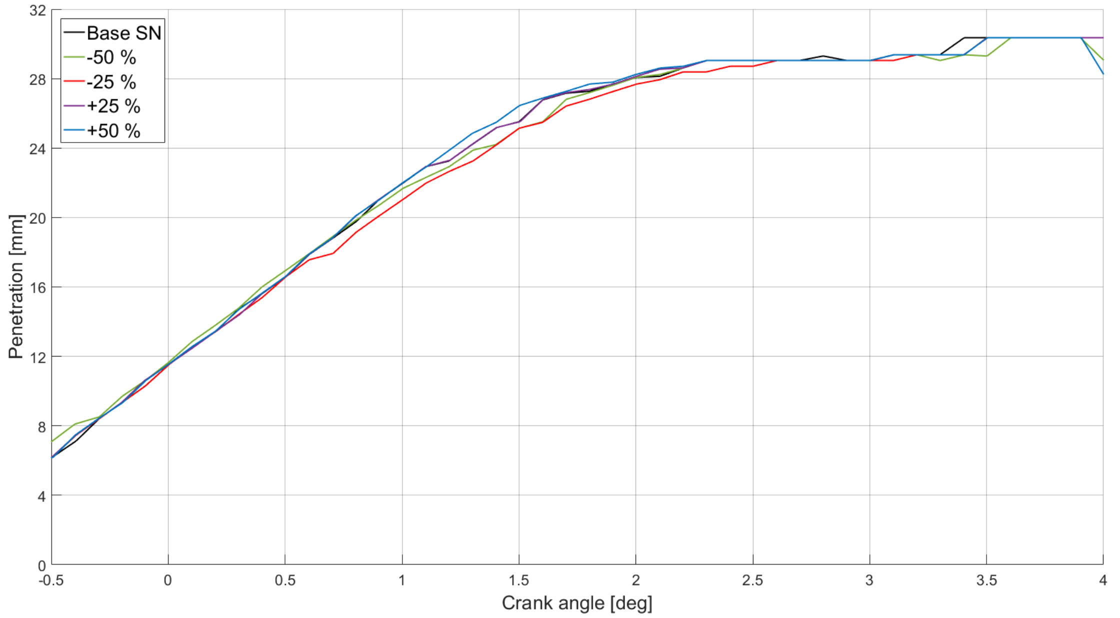

Figure 6-18 Comparison of vapor penetrations for different swirl ratios at part load

6.2.2 Influence on Combustion Process

In-cylinder pressure and heat release rate at full load (o. p. 2000 [rev/min] x 18 [bar]) for different swirl ratios are shown in Figure 6-19.

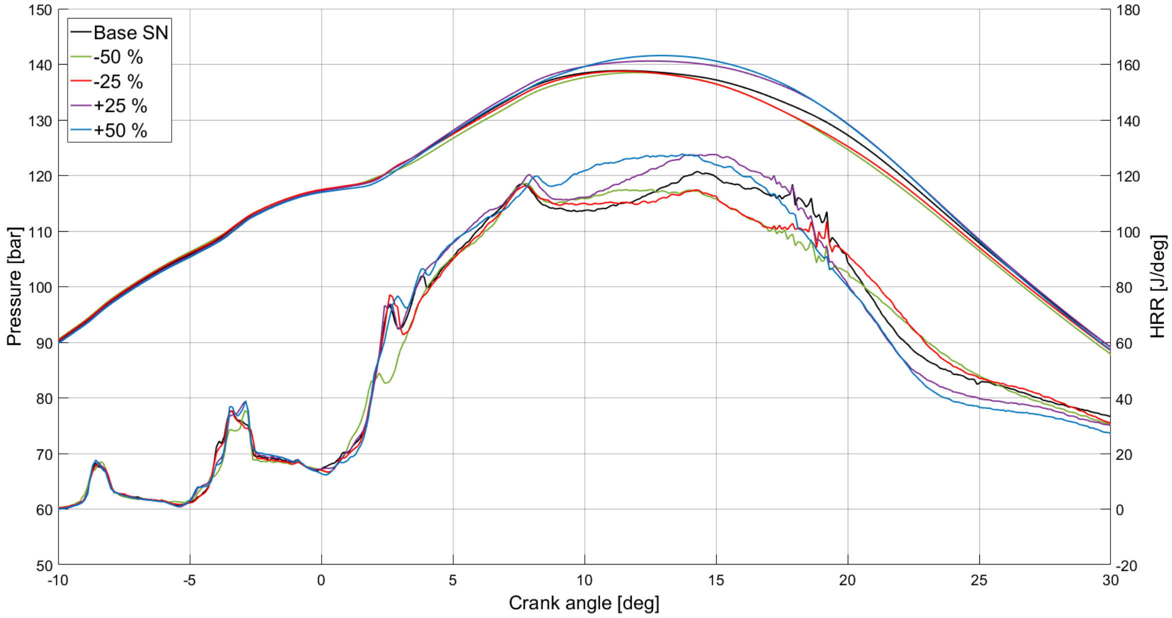

Figure 6-19 In-cylinder pressure and HRR for different swirl ratios at full load

Increasing the swirl ratio, the heat release rate during the premixed and the mixing-controlled combustion phases increases, and the overall combustion duration is shortened (see also Figure 6-26; the heat release rate from 25 CAD remains higher for cases with lower SR, which is especially visible for the -50 % SR case). The HRR curve for the +50 % SR case starts dropping from about 14 CAD (during late mixing-controlled combustion phase) and quickly falls under all other curves. It indicates that for this case more fuel has burned up to now than for other cases. Finally, -50 %

SR case seems to be the most impacted in the premixed combustion phase, while other cases show smaller differences.

Changes in the swirl rate change the fuel evaporation and air-fuel mixing processes [2]. Increasing the swirl ratio, turbulent kinetic energy is increased (see Figure 6-20; an important timing is about 0 CAD, when autoignition of the main portion of the charge happens), aiding the rates of mass transfer and mixing. Thus, more mixture is available at the start of combustion, producing more intensive premixed burn. Furthermore, increased turbulence helps to complete molecular level air-fuel mixing faster, so the mixing-controlled burning is also more intensive.

Lastly, it can be seen from Figure 6-19 that the effect of the swirl ratio on the heat released during the burning of pilots is relatively small; it may be related with a small mass of fuel injected during these injection events.

Quantitative comparisons between simulations with different SR at full load are provided in Table 6.7 in terms of combustion progress parameters, i.e., peak firing pressure, crank angle location for the peak firing pressure, MFB50, and MFB10-MFB90.

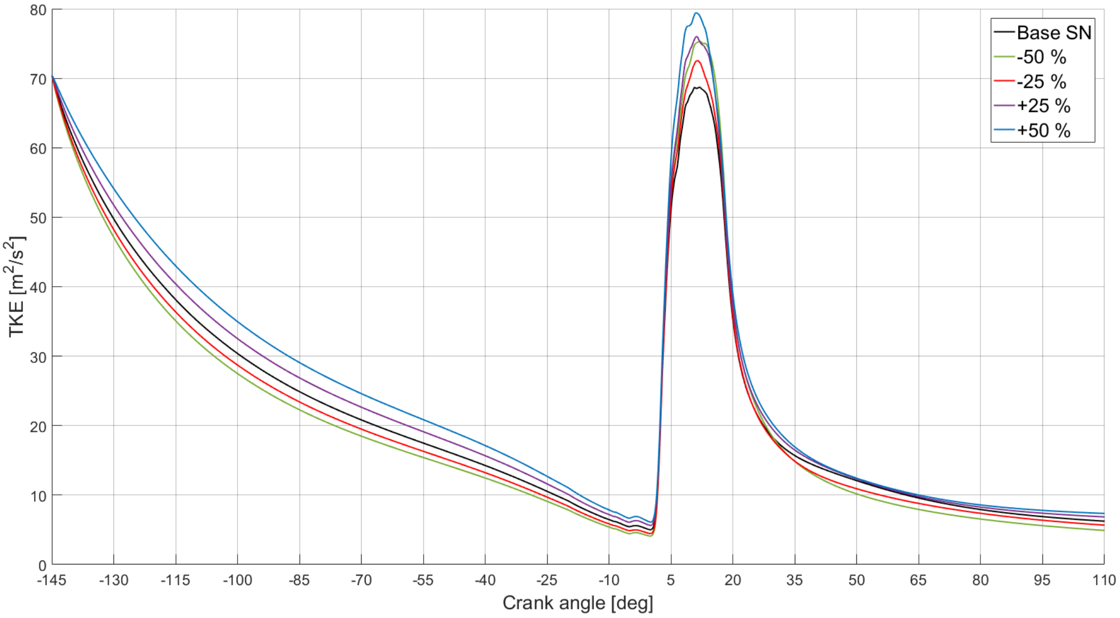

Figure 6-20 Turbulent kinetic energy for different swirl ratios at full load

Table 6.7 Comparison of combustion progress for different swirl ratios at full load

Swirl Ratio	Peak Firing Pressure	CA at Peak Firing Pressure	MFB50	MFB10-MFB90
	bar	deg	deg	deg
Base	138.9	11.4	15.3	28.5
-50 %	138.5 (-0.29 %)	11.9 (+4.39 %)	15.5 (+1.31 %)	31.3 (+9.82 %)
-25 %	138.8 (-0.07 %)	11.4 (–)	15.5 (+1.31 %)	30.0 (+5.26 %)
+25 %	140.6 (+1.22 %)	12.5 (+9.65 %)	14.8 (-3.27 %)	28.1 (-1.40 %)
+50 %	141.6 (+1.94 %)	12.9 (+13.2 %)	14.6 (-4.58 %)	29.1 (+2.11 %)

From Table 6.7 it is clear that at full load the analyzed CFD model is more sensitive to increased swirl ratio, except for the combustion duration (MFB10-MFB90) which is impacted more by a decrease in SR. Also, for all cases with changed SR (except for the -25 % case), when compared to the base case, the peak firing pressure is achieved later.

In conclusion, increasing the swirl ratio at full load, the peak firing pressure increases, combustion process mid-point is achieved faster, and combustion takes less time to complete (except for the +50 % case; it may indicate a not optimal swirl for a given engine).

In-cylinder pressure and heat release rate at part load (o. p. 2000 [rev/min] x 9 [bar]) for different swirl ratios are shown in Figure 6-21. Change of the swirl ratio at part load has smaller effect on combustion than at full load. There are relatively smaller differences in pressure curves, and curves of heat release rate are more closely matched. The swirl ratio has a more visible effect on the premixed phase of combustion (from 0 CAD to 5 CAD in Figure 6-21) in the case with -50 % SR; the same trend was spotted at full load.

Differently from the results at full load, the case with -50 % SR has the highest heat release rate during middle part mixing-controlled combustion (from 10 CAD to 10 CAD).

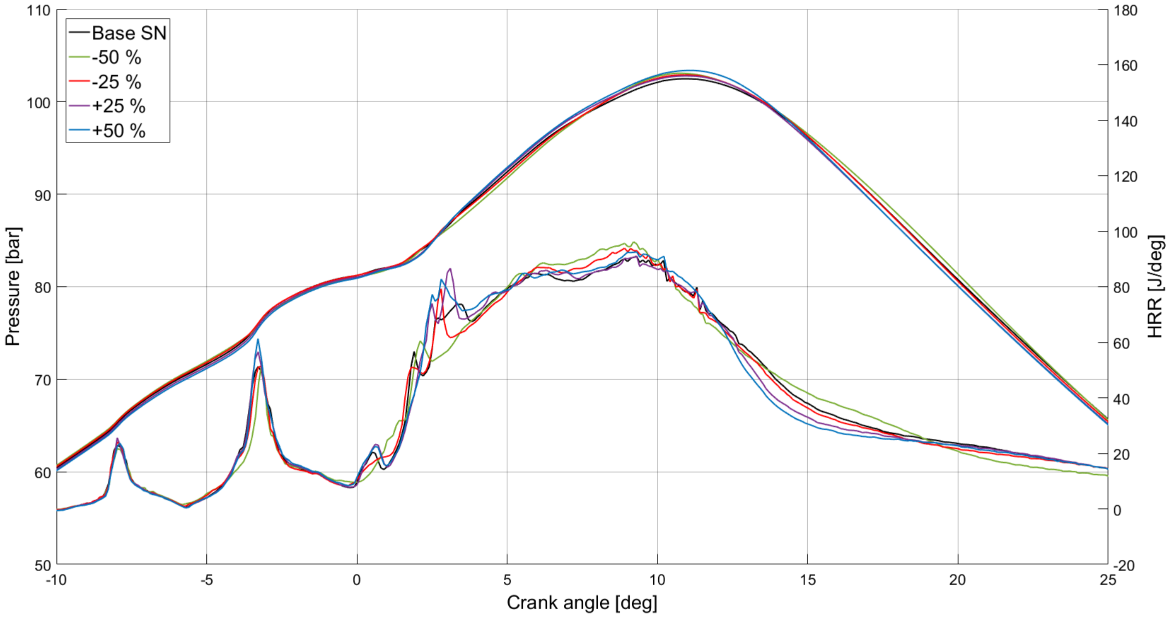

Figure 6-21 In-cylinder pressure and HRR for different swirl ratios at part load

Quantitative comparisons between simulations with different SR at part load are provided in Table 6.8 in terms of combustion progress parameters

Table 6.8 Comparison of combustion progress for different swirl ratios at part load

Swirl Ratio	Peak Firing Pressure	CA at Peak Firing Pressure	MFB50	MFB10-MFB90
	bar	deg	deg	deg
Base	102.5	10.9	9.88	22.7
-50 %	103.1 (+0.59 %)	10.7 (-1.83 %)	9.86 (-0.20 %)	22.7 (–)
-25 %	102.9 (+0.39 %)	10.9 (–)	9.83 (-0.51 %)	23.2 (+2.20 %)
+25 %	102.8 (+0.29 %)	10.9 (–)	9.76 (-1.21 %)	23.6 (+3.96 %)
+50 %	103.4 (+0.88 %)	11.1 (+1.83 %)	9.64 (-2.43 %)	23.6 (+3.96 %)

Table 6.8 shows that at part load the CFD model is less sensitive to variations in the swirl ratio than at full load. Also, as before, the CFD model is more sensitive to increased swirl ratio, especially when MFB50 timing and combustion duration parameters are considered.

However, at part load there is no clear distinction regarding effects of the SR on the combustion: both increase and decrease in the SR provide increase in the peak pressure and reduction of the MFB50 timing (at full load, only increased swirl ratios provide higher peak pressure and reduced MFB50 timing).

6.2.3 Influence on Pollutant Emissions

Figure 6-22 shows curves representing NOx mass within the cylinder for different swirl ratios at full load (o. p. 2000 [rev/min] x 18 [bar]).

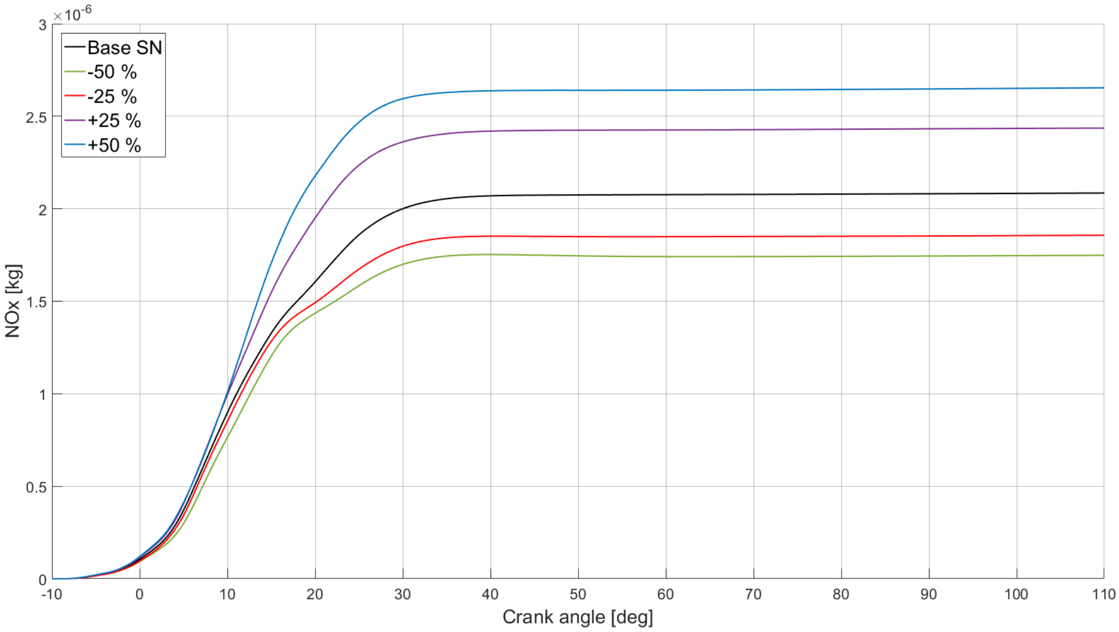

Figure 6-22 NOx emissions for different swirl ratios at full load

Increasing the swirl ratio, NOx emissions are also increased. As explained in Section 6.2.2, increased swirl promotes evaporation of the fuel and air-fuel mixing process, making both premixed and mixing-controlled combustion phases more intense. Thus, the mean in-cylinder temperature is higher (as shown in Figure 6-23; from 0 CAD to 30 CAD there is a visible difference between temperatures of cases with higher and lower swirl ratios), resulting in increased overall NOx production rates (although NOx emissions in diesel engines are strongly dependent on local temperatures and local equivalence ratios during combustion [12], the mean temperature is able to represent the overall situation).

NOx production rates for both -50 % and -25 % cases start to fall down significantly (if compared to cases with increased SR) from about 17 CAD. At that timing, the HRR curves of cases with decreased SR are below those of other cases, while the expansion stroke happens. Thus, the produced heat is not enough to stop the freezing of chemical reactions producing NOx. Finally, from 40 CAD the production of NOx has stopped for all cases, and mean in-cylinder temperatures dropped well below 2000 K (see Figure 6-23).

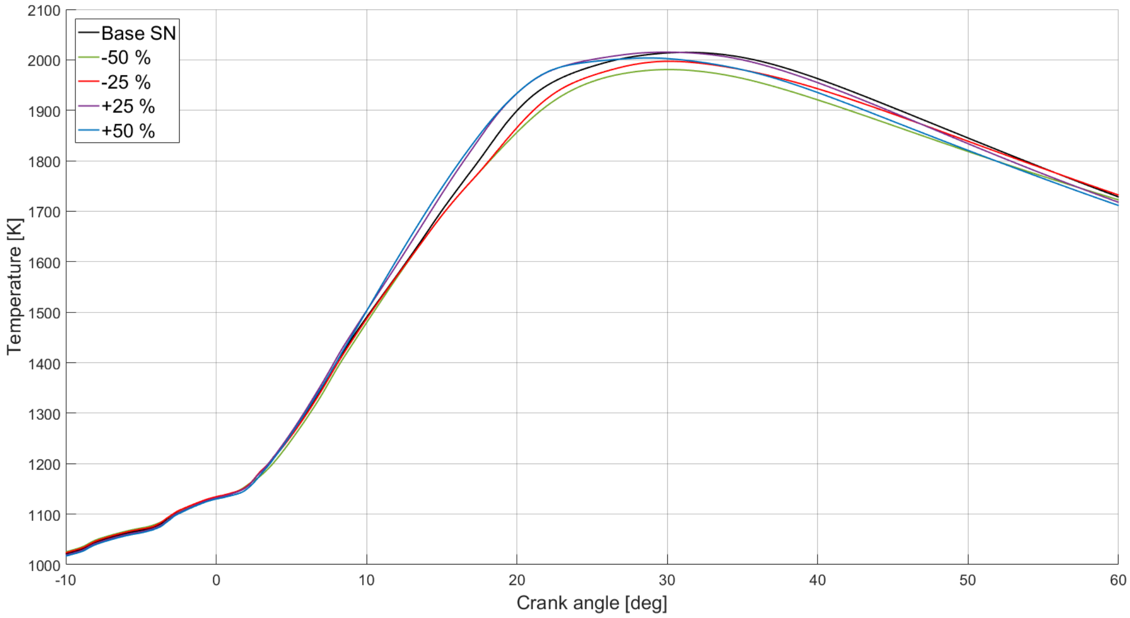

Figure 6-23 Mean in-cylinder temperature for different swirl ratios at full load

NOx emissions curves at half load (o. p. 2000 [rpm] x 9 [bar]) for different swirl ratios are shown in Figure 6-24.

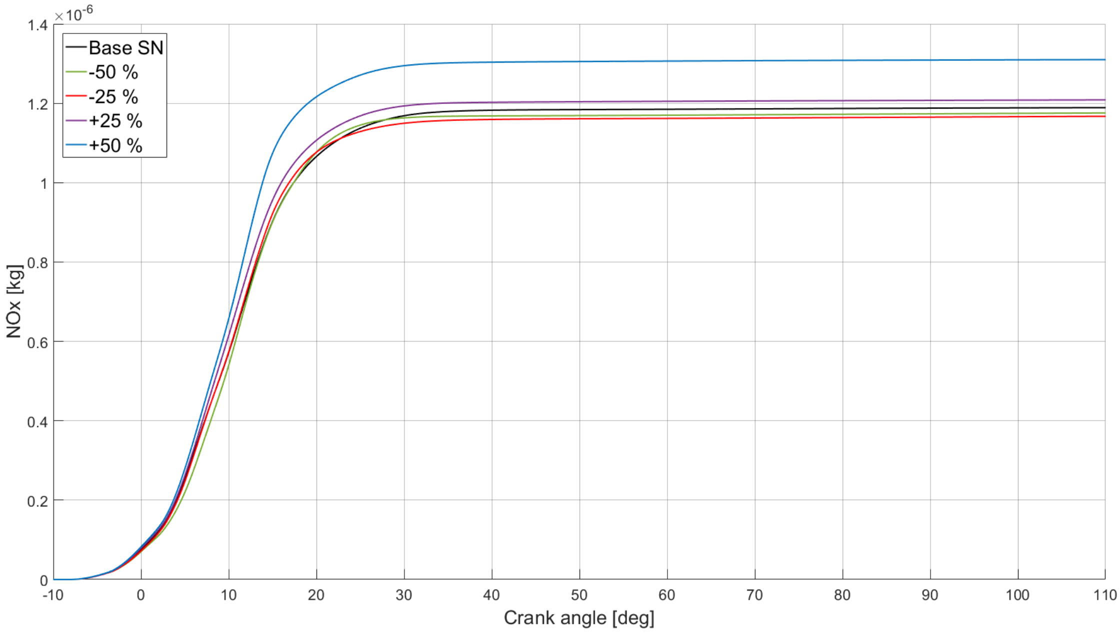

Figure 6-24 NOx emissions for different swirl ratios at part load

At part load conditions, increasing the swirl ratio increases NOx emissions, same as at full load. However, the effect is smaller than at full load, and only emissions in the case with +50 % SR has a more distinct increase. The heat release rate during the late part of mixing-controlled combustion (from 10 CAD to 20 CAD in Figure 6-21) is higher for the -50 % SR case than for the -25 % SR case, meaning the final value of NOx is lower for the latter.

Figure 6-25 shows curves representing soot mass within the cylinder for different swirl ratios at full load (o. p. 2000 [rev/min] x 18 [bar]).

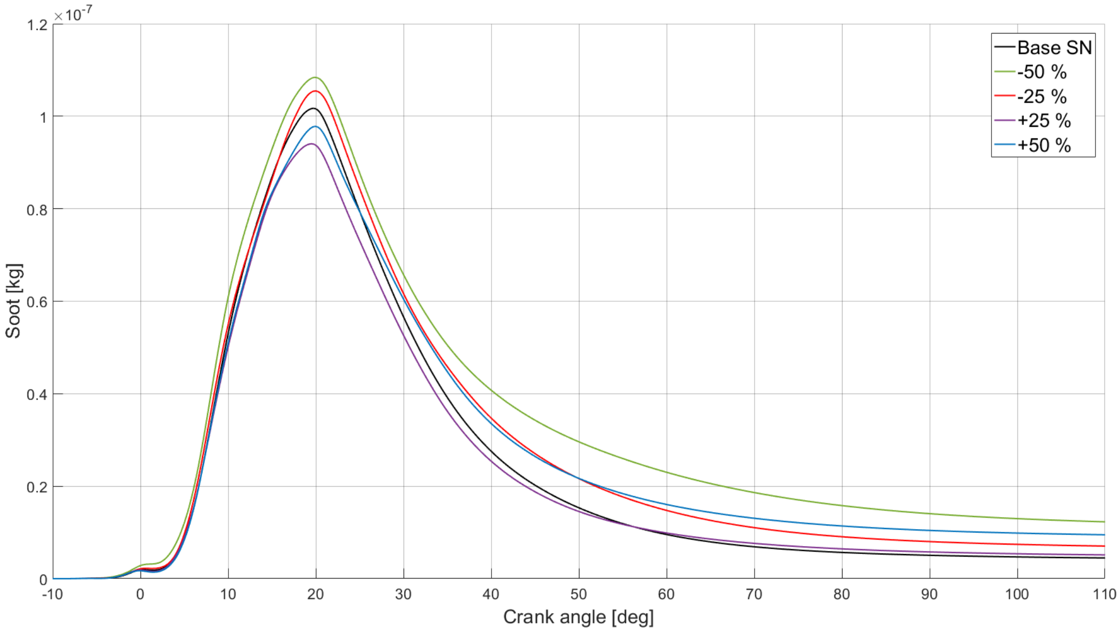

Figure 6-25 Soot emissions for different swirl ratios at full load

Increasing the swirl ratio, soot emissions are increased for all analyzed cases. This seems to contradict the theory (see Section 2.5.1), which states that improved mixing should reduce formation of soot. Indeed, up to about 25 CAD, simulations with increased SR show reduced soot levels (as higher mixing is achieved, thus providing locally leaner combustion), while these with reduced SR – increased. However, in later stages the soot oxidation process seems to slow-down more for simulations with higher SR, producing higher final values of emitted soot.

Increase in soot emissions with increased swirl was also noted in [48], [49], and [12]: in the first case it was concluded that soot forms actively as a result of the increase in the fuel vapor concentration at the center of the combustion chamber in the case of too high swirl [48], while in the second case authors thought that due to high swirl the volume available for air-fuel mixing and soot oxidation is reduced (due to the negative effect of deviation of the spray towards the center of the chamber) and the soot increases [49]. In [12] it was found out that increased swirl improves the soot emissions only up to a certain swirl value. Then, high swirl rates confine the spray, with possible spray overlapping, producing a large deflection that reduces air entrainment and increase the in-cylinder heat transfer, resulting in lower mean gas temperatures. These factors affect soot oxidation, increasing soot emissions [12]. Finally, all researches conclude that the optimal swirl ratio exists for a given engine, which enables to achieve the lowest soot emissions.

Indeed, when comparing soot production and oxidation for the base case to the +50 % case, it seems from Figure 6-25 that for the latter the decrease of the soot mass is slower from 20 CAD to 50 CAD, resulting in the higher soot mass at EVO. This may be an outcome of the HRR being lower for the +50 % case in the same CA period (see Figure 6-28), and consequently lower mean in-cylinder temperature from 27 CAD onwards (see Figure 6-23).

Figure 6-26 shows curves representing soot mass within the cylinder for different swirl ratios at part load (o. p. 2000 [rev/min] x 9 [bar]). The situation is the same as at full load: both increase and decrease in SR result in increase of soot emissions. However, the differences are smaller than at full load, indicating lower sensitivity of soot emissions on the swirl ratio at part load.

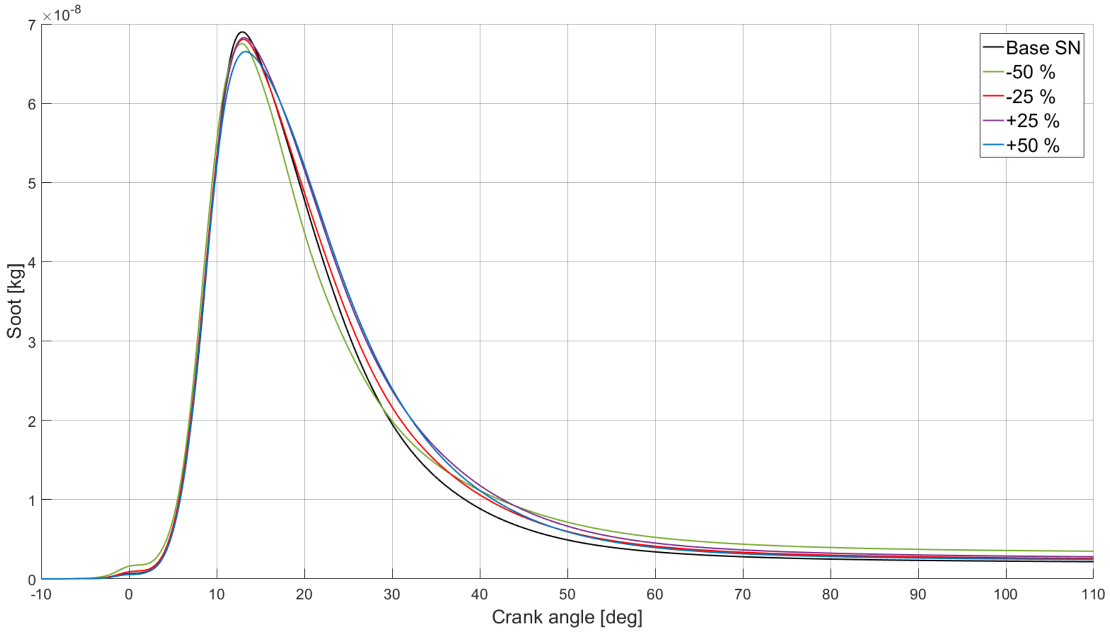

Figure 6-26 Soot emissions for different swirl ratios at part load

Quantitative comparisons for both operating points with different swirl ratios are provided in Table 6.9 in terms of final emitted values of NOx and soot, as well as of the percentage difference relative to the base case. Also, experimental values are given for reference.

Table 6.9 Comparison of pollutant emissions for different swirl ratios

Swirl Ratio	NOx	Soot
	mg	µg
2000 [rev/min] x 18 [bar]		
Experimental	1.505	7.821
Base	2.085	4.483
-50 %	1.748 (-16.2 %)	12.30 (+174 %)
-25 %	1.857 (-10.9 %)	7.053 (+57.3 %)
+25 %	2.436 (+16.8 %)	5.142 (+14.7 %)
+50 %	2.654 (+27.3 %)	9.498 (+112 %)
2000 [rev/min] x 9 [bar]		
Experimental	0.653	12.99
Base	1.189	2.169
-50 %	1.176 (-1.09 %)	3.487 (+60.8 %)
-25 %	1.167 (-1.85 %)	2.573 (+18.6 %)
+25 %	1.209 (+1.68 %)	2.790 (+28.6 %)
+50 %	1.310 (+10.2 %)	2.449 (+12.9 %)

At both full and part load conditions, the CFD model shows bigger sensitivity for soot emissions than for NOx emissions. Also, the model seems to be more affected by changes in SR at full load (both in terms of NOx and soot emissions), except of the +25 % case for soot emissions.

As has been mentioned before, for simulations done in the present work, soot emissions increase with both increased and decreased SR, while NOx emissions are increased only for increased swirl ratios.

6.2.4 Fine-Tuning of CFD Model

After the SR sensitivity analysis has been presented in previous sections, the experimental curves of the in-cylinder pressure and the heat release rate at full load can be compared with cases analyzed; Figure 6-27 and Figure 6-28 show these comparisons, respectively.

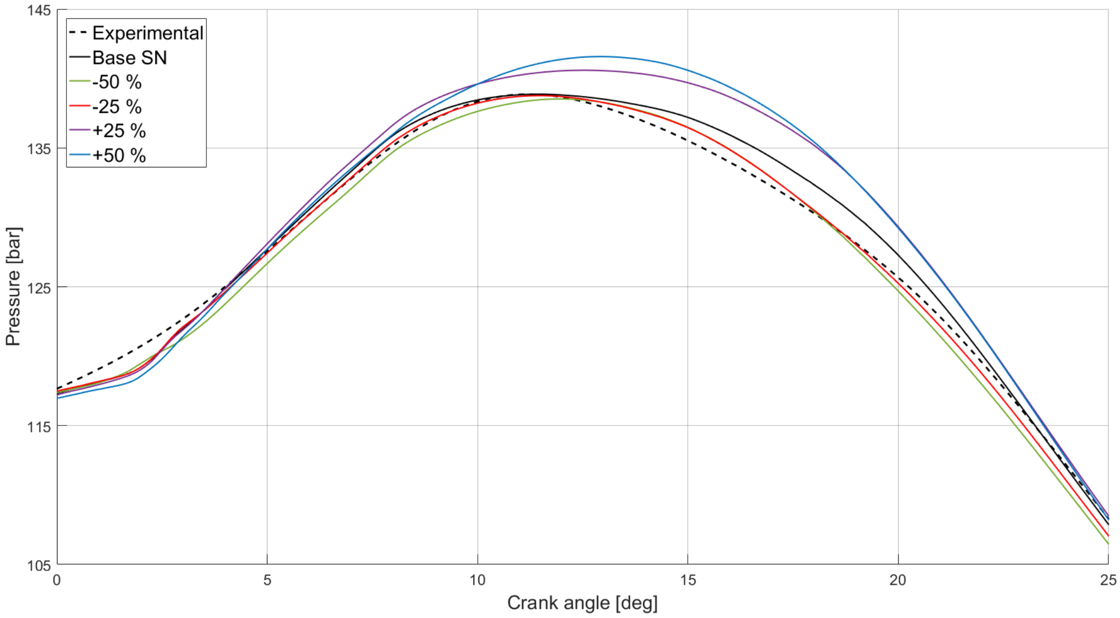

Figure 6-27 Pressure at full load for fine-tuning using different swirl ratios

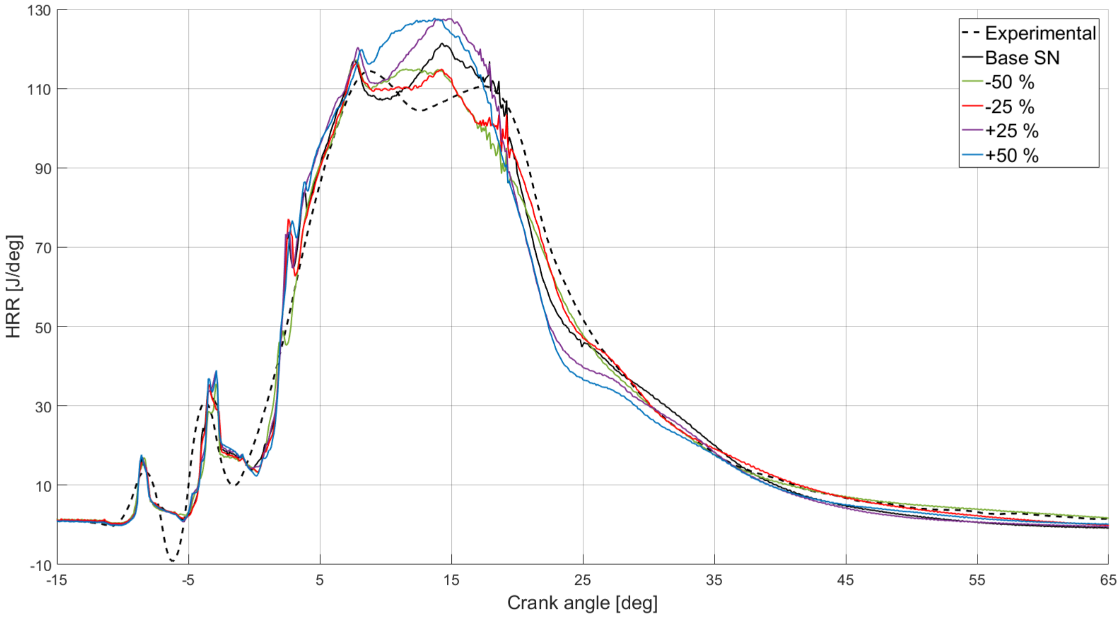

Figure 6-28 HRR at full load for fine-tuning using different swirl ratios

As can be seen from Figure 6-27, the -25 % SR case matches the experimental curve the best; from 5 CAD to 20 CAD it approximates the experimental line better than the base case. Also, the experimental heat release rate curve is followed better by the -25 % SR case, especially from about 15 CAD onwards, as shown in Figure 6-28. Finally, the data presented in Table 6.9 indicates that the -25 % SR case gives more accurate estimation for NOx emissions (compared to the base case), and the best overall estimate for soot emissions.

Figure 6-29 and Figure 6-30 show a comparison between experimental and simulated curves of the in-cylinder pressure and the heat release rate at part load.

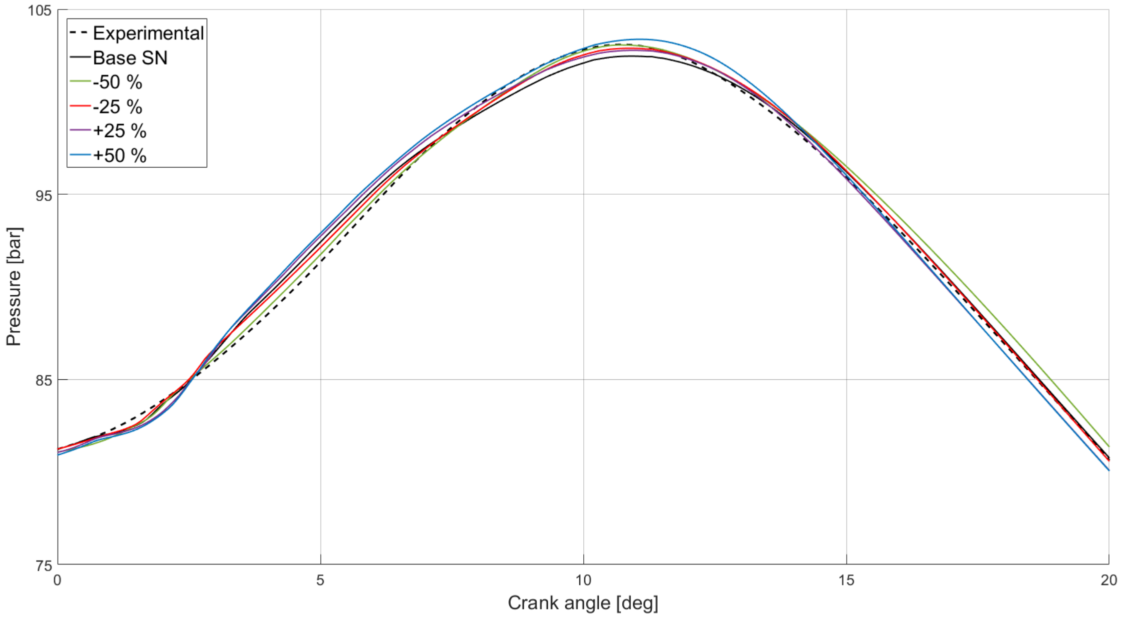

Figure 6-29 Pressure at part load for fine-tuning using different swirl ratios

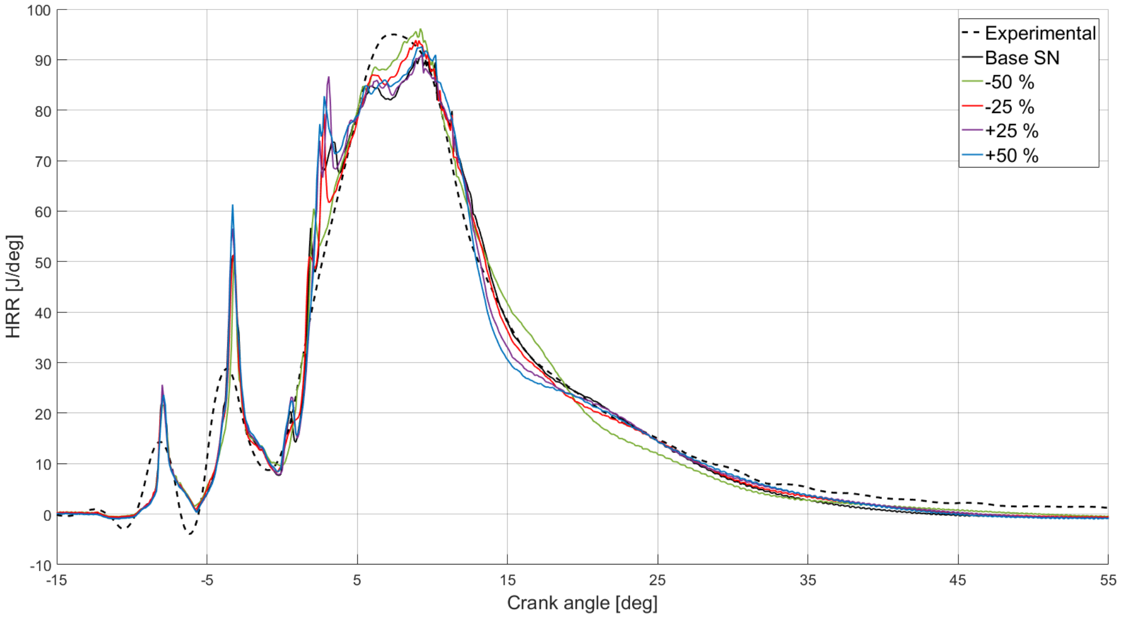

Figure 6-30 HRR at part load for fine-tuning using different swirl ratios

Figures show that decreasing SR helps to better match both experimental pressure and heat release rate curves. However, differently from the situation at full load (where the best improvement is with -25 % SR), both cases with decreased SR show improvements in different CA intervals: the -50 % SR case seems to better approximate the experimental data from 3 CAD to 13 CAD, while the -25 % SR case show improvement from 13 CAD onwards. In addition, data in Table 6.9 presents bigger improvement in the estimation of NOx emissions for the -25 % SR case, while the -50 % SR gives a more accurate prediction of soot emissions.

In conclusion, decrease in SR by 25 % shows bigger improvement in the simulation results at full load. To provide continuity in selecting parameters for CFD simulations, the -25 % SR case is selected as the most representative also at part load.

6.3 Turbulent Schmidt Number Sensitivity Analysis

The turbulent Schmidt number ($\mathrm{Sc_t}$ or simply Sc) is a dimensionless number defined as the ratio between the rates of turbulent transport of momentum and turbulent transport of mass:

$$\mathrm{Sc} = \frac{\nu_t}{\mathrm{D_t}}, \tag{6.1}$$

where ν_t is the turbulent viscosity, and $\mathrm{D_t}$ is the turbulent mass diffusion coefficient.

If it is assumed that the turbulence level is constant for any value of Sc, also ν_t is constant. Thus, in CFD simulations, change in the Schmidt number means change in the turbulent mass diffusion coefficient $\mathrm{D_t}$, which impacts diffusion terms for transport equations of species and passives. As a result, increasing Sc, species diffusion decreases; it can significantly alter the mixing process between the fuel and air.

For diesel sprays in general, Schmidt number values found in the literature are between 0.6 and 0.8 [50], while for modern injection systems Schmidt number of 0.5 was found to be the most accurate [39]. In real injection conditions, Sc has a significant influence on spray characteristics, especially in the near nozzle field, where primary and secondary atomization take place [39].

For simulations done up to now, the Schmidt number of 0.5 was used (considering the results provided in [39]), as already mentioned in Section 5.4.2. However, taking into account the explanation given above, changes in Sc can impact the air-fuel mixing process, thus modifying the combustion process and pollutant emissions. A sensitivity analysis is done to understand impact of Sc on diesel simulations: values of 0.6, 0.7, and 0.8 are selected to be tested.

Finally, as reduction by 25 % in the swirl ratio was found to match better the experimental data (see Section 6.2.4), it is selected as the base case for the Schmidt number sensitivity analysis.

6.3.1 Influence on Combustion Process

Figure 6-31 shows in-cylinder pressure and heat release rate curves for different Schmidt numbers at full load (o. p. 2000 [rev/min] x 18 [bar]).

Increasing the Schmidt number, HRR during the premixed and early mixing-controlled phases of combustion (from 0 CAD to 8 CAD) is reduced, resulting in lower pressure rise and lower peak firing pressure. As has been explained at the beginning of Section 6.3, increasing Sc, the air-fuel mixing process becomes less intense, resulting in less mixture within the flammability limits available at the point of autoignition (around 0.5 CAD), followed by lower premixed burn.

At certain period during the mixing-controlled combustion (from about 15 CAD to 20 CAD), simulations with increased Sc show higher HRR than those with lower Sc; it may be due to more fuel available for combustion (in cases with lower Sc, more fuel is consumed early in the process). However, differences in HRR at this period are small, and all curves merge from about 20 CAD.

From about 35 CAD onwards, HRR for simulations with increased Sc is higher than for those with lower Sc, as can be seen in Figure 6-32. This indicates a slower combustion process in the case of decreased Schmidt number, as expected considering slower air-fuel mixing process.

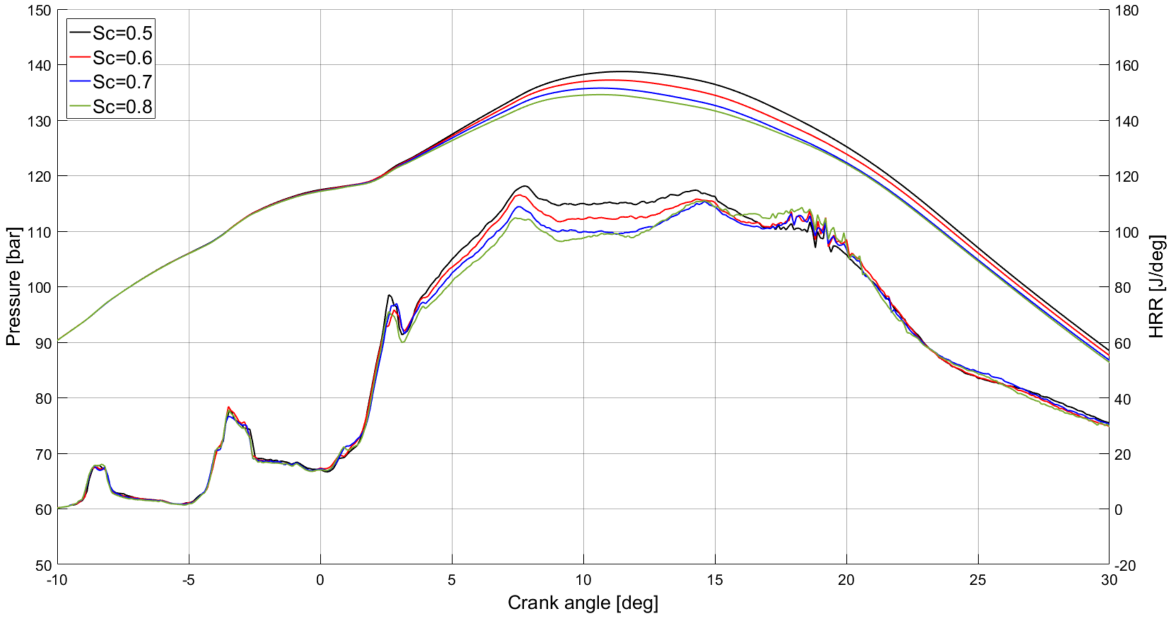

Figure 6-31 In-cylinder pressure and HRR for different Schmidt numbers at full load

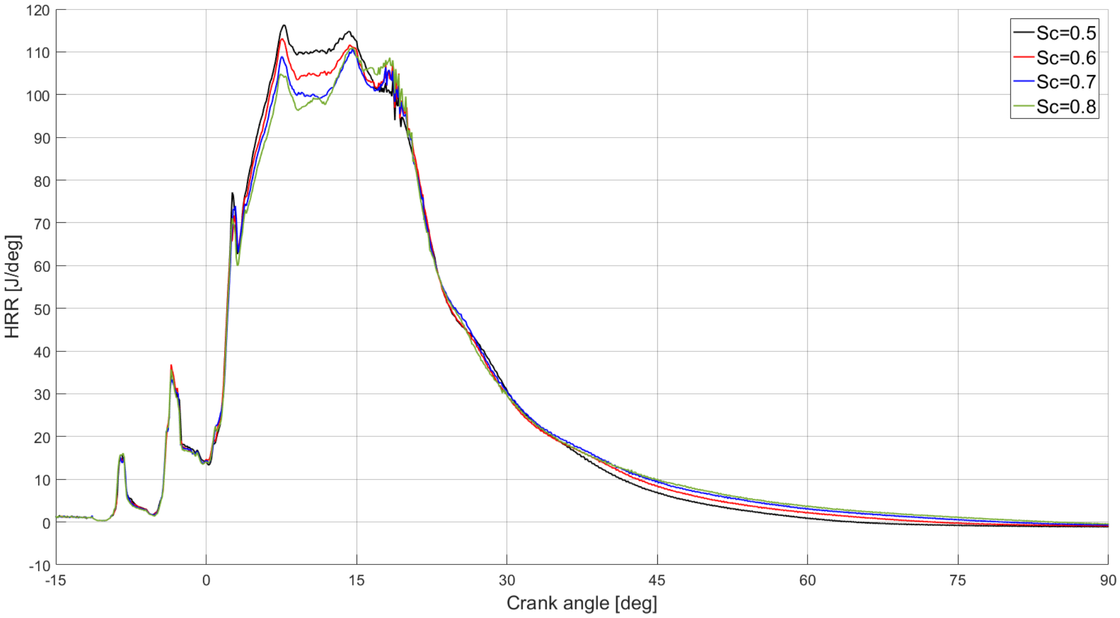

Figure 6-32 HRR for different Schmidt numbers at full load

Quantitative comparisons between simulations with different Sc at full load are provided in Table 6.10 in terms of combustion progress parameters, i.e., peak firing pressure, crank angle location for the peak firing pressure, MFB50, and MFB10-MFB90.

Table 6.10 Comparison of combustion progress for different Schmidt numbers at full load

Schmidt Number	Peak Firing Pressure	CA at Peak Firing Pressure	MFB50	MFB10-MFB90
	bar	deg	deg	deg
0.5 (base)	138.8	11.4	15.5	30.0
0.6	137.2 (-1.15 %)	11.0 (-3.51 %)	15.9 (+2.58 %)	32.3 (+7.67 %)
0.7	135.8 (-2.16 %)	10.7 (-6.14 %)	16.2 (+4.52 %)	34.4 (+14.7 %)
0.8	134.6 (-3.03 %)	10.7 (-6.14 %)	16.4 (+5.81 %)	35.8 (+19.3 %)

Increasing the Schmidt number, peak firing pressure is reduced, and it is achieved earlier. Also, the combustion process slows down, as 50 % of mass fraction burned is achieved later, and overall combustion duration (MFB10-MFB90) increases. Finally, it can be seen that the CFD model is the most sensitive in terms of the combustion duration when changing Sc.

Figure 6-33 shows in-cylinder pressure and heat release rate curves for different Schmidt numbers at part load (o. p. 2000 [rev/min] x 9 [bar]).

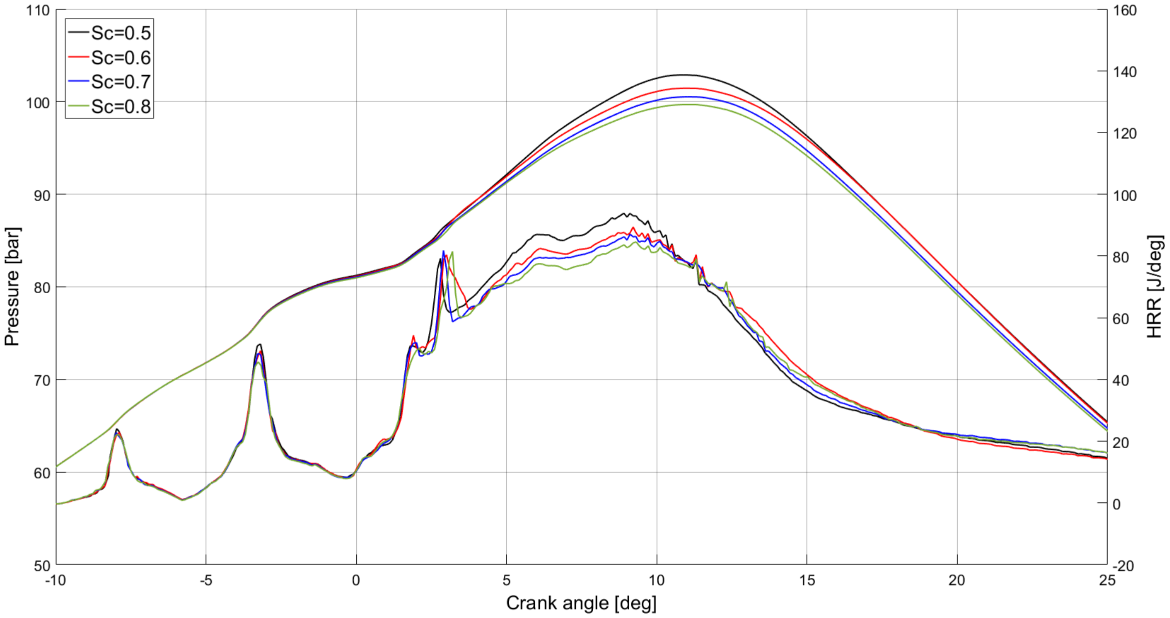

Figure 6-33 In-cylinder pressure and HRR for different Schmidt numbers at part load

Increasing the Schmidt number at part load, HRR during the premixed and early mixing-controlled phases of combustion (from 0 CAD to 7 CAD) is reduced, resulting in lower pressure rise and lower peak firing pressure. This result matches the trend obtained at full load.

HRR rate for cases with higher Sc remains lower until about 11 CAD; from then onwards simulations with increased Sc show higher HRR until the end of heat release (see Figure 6-34). The only exception is the case with Sc=0.6, which provides the highest HRR from 11 CAD to 19 CAD, and the lowest from 19 CAD to 27 CAD.

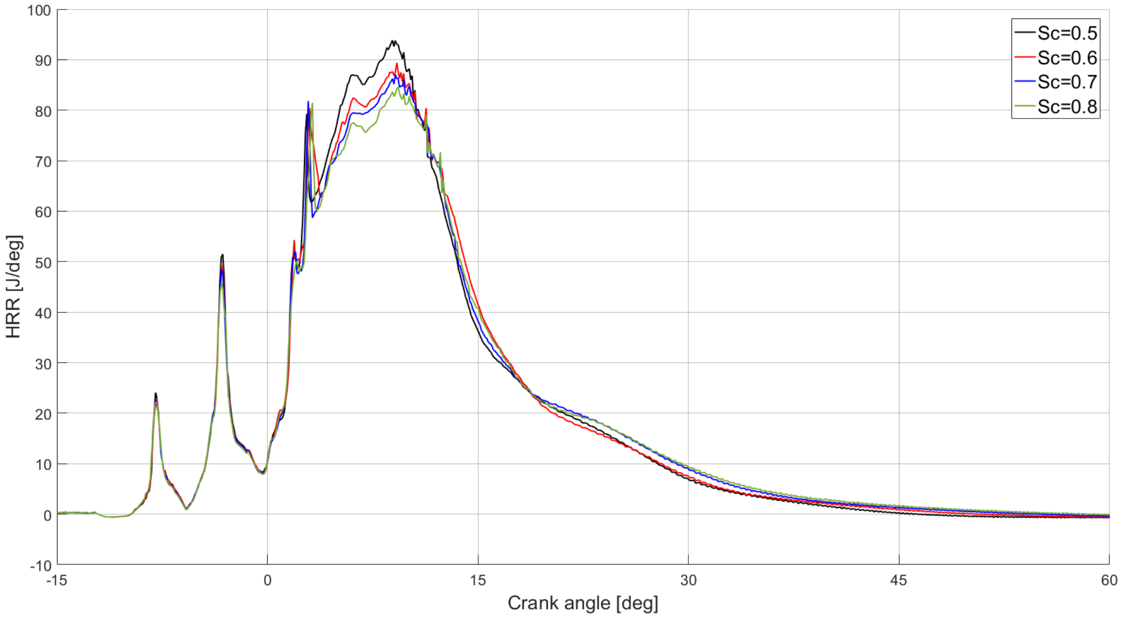

Figure 6-34 HRR for different Schmidt numbers at part load

Quantitative comparisons between simulations with different Sc at part load are provided in Table 6.11 in terms of combustion progress parameters.

Table 6.11 Comparison of combustion progress for different Schmidt numbers at part load

Schmidt Number	Peak Firing Pressure	CA at Peak Firing Pressure	MFB50	MFB10-MFB90
	bar	deg	deg	deg
0.5 (base)	102.9	10.9	9.83	23.2
0.6	101.4 (-1.46 %)	11.0 (+0.92 %)	10.2 (+3.76 %)	24.0 (+3.45 %)
0.7	100.5 (-2.33 %)	11.1 (+1.83 %)	10.3 (+4.78 %)	25.5 (+9.91 %)
0.8	99.7 (-3.11 %)	11.0 (+0.92 %)	10.5 (+6.82 %)	26.5 (+14.2 %)

Increasing the Schmidt number at part load, peak firing pressure is reduced. However, in opposite to situation at full load, the peak pressure is not achieved earlier with increasing Sc. Instead, the timing is retarded, and also shows lower sensitivity to changed Sc than at full load.

Remaining parameters follow the same trend as at full load: the combustion process slows down, as 50 % of mass fraction burned is achieved later, and overall combustion duration (MFB10-MFB90) increases. The CFD model is again the most sensitive in terms of the combustion duration.

6.3.2 Influence on Pollutant Emissions

Figure 6-35 shows curves representing NOx mass within the cylinder for different Schmidt numbers at full load (o. p. 2000 [rev/min] x 18 [bar]).

Increase in the Sc at full load results in reduced NOx emissions. Increasing Sc, the heat release rate during premixed and early mixing-controlled combustion phases is reduced, resulting in lower peak in-cylinder pressure and temperature. Thus, the production of thermal NOx is impeded, as has been explained in Section 2.5.

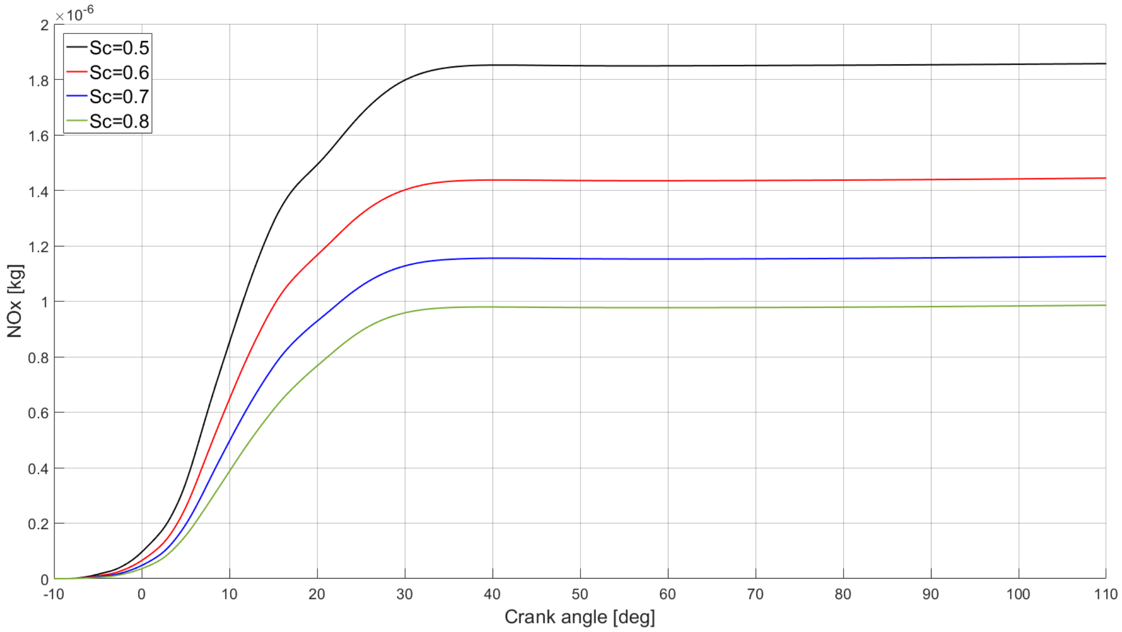

Figure 6-35 NOx emissions for different Schmidt numbers at full load

Similar results are obtained at part load (o. p. 2000 [rev/min] x 9 [bar]), as shown in Figure 6-36. As before, increased Sc results in lowered NOx emissions.

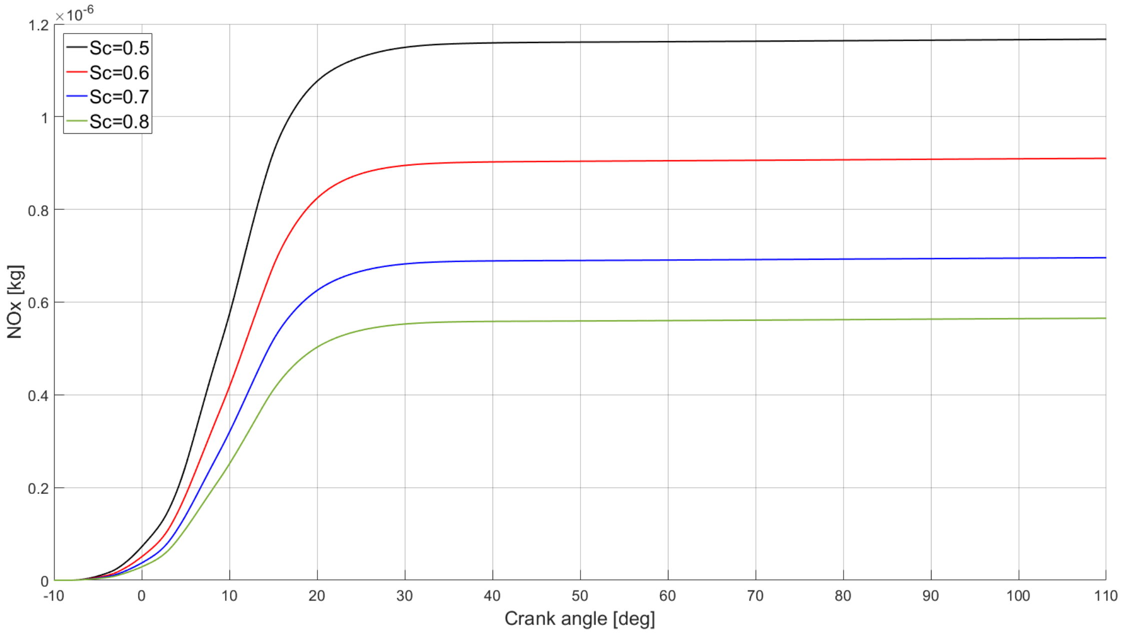

Figure 6-36 NOx emissions for different Schmidt numbers at part load

Figure 6-37 shows curves representing soot mass within the cylinder for different Schmidt numbers at full load (o. p. 2000 [rev/min] x 18 [bar]).

Soot emissions are increased when increasing the Schmidt number at full load. As diffusion rate of species is decreasing with increasing Sc, the air-fuel mixing process is slowed down, and the mixture at the point of autoignition is richer. Thus, the initial soot formation increases, as explained in Section 2.5. Due to increased combustion duration (see Table 6.9), oxidation of soot continues longer in the case of higher Sc (note that the slope of soot mass curve in Figure 6-37 vanishes at about 90 CAD for Sc=0.5, while it remains to the end of simulation for Sc=0.8). However, the final values of soot mass remain higher for simulations with lower Sc.

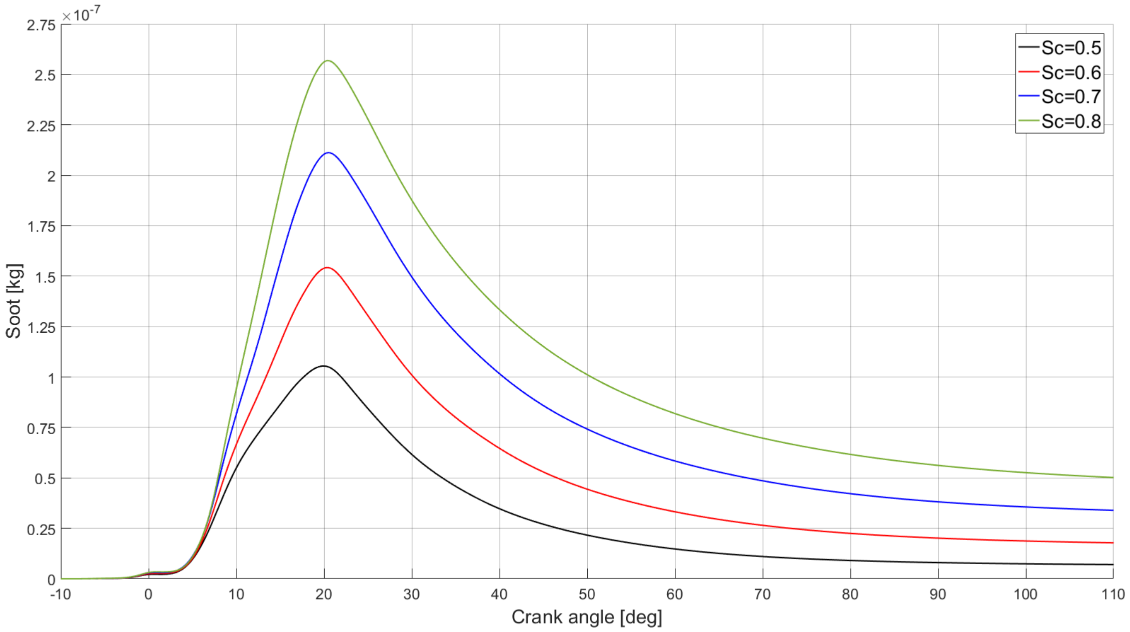

Figure 6-37 Soot emissions for different Schmidt numbers at full load

Similar results are obtained at part load (o. p. 2000 [rev/min] x 9 [bar]), as shown in Figure 6-38. Increased Sc results in higher soot emissions.

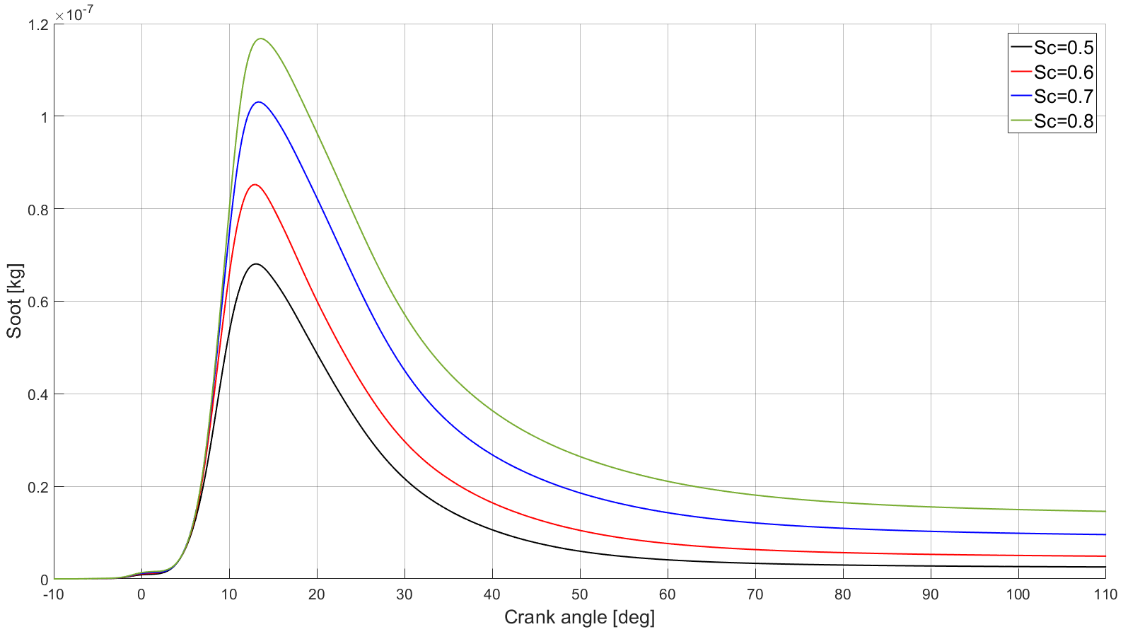

Figure 6-38 Soot emissions for different Schmidt numbers at part load

Quantitative comparison of pollutant emissions results for simulations with different Schmidt numbers at both operating points are given in Table 6.12. Comparison is made in terms of final emitted values of NOx and soot, as well as of the percentage difference relative to the base case.

Table 6.12 Comparison of pollutant emissions for different Schmidt numbers

Schmidt Number	NOx	Soot
	mg	µg
2000 [rev/min] x 18 [bar]		
0.5 (base)	1.857	7.053
0.6	1.444 (-22.2 %)	17.83 (+153 %)
0.7	1.162 (-37.4 %)	33.94 (+381 %)
0.8	0.986 (-46.9 %)	50.21 (+612 %)
2000 [rev/min] x 9 [bar]		
0.5 (base)	1.167	2.573
0.6	0.910 (-22.0 %)	4.906 (+90.7 %)
0.7	0.696 (-40.4 %)	9.576 (+272 %)
0.8	0.565 (-51.6 %)	14.59 (+467 %)

Results given in Table 6.12 indicate that increasing Sc at both operating points, NOx emissions are reduced, while soot – increased. The CFD model is more sensitive to variation of the Schmidt number in terms of soot emissions. Also, the sensitivity is higher for simulations at full load when soot emissions are considered.

In terms of NOx emissions, simulations at part load demonstrate higher sensitivity to variation of the Schmidt number, however differences are smaller than for soot emissions.

6.3.3 Fine-Tuning of CFD Model

Taking into consideration the analysis done in previous sections, the Schmidt number can be used as a variable for CFD model calibration in the CONVERGE CFD software.

Increasing Schmidt number, the heat release rate during premixed and early mixing-controlled combustion phases is reduced, and the overall combustion duration increases. Thus, the in-cylinder pressure rise is slower, resulting in the lower peak firing pressure. As a result, simulated NOx emissions are reduced, while soot emissions increase.

The behavior of CFD computation described above can be useful when trying to match an experimental in-cylinder pressure curve, or emitted values of NOx and soot.

7 Conclusions

In the present thesis, work has been carried out on the combustion process of the conventional diesel engine using the CONVERGE CFD software. This work is part of the activity started at the Energy Department of Politecnico di Torino to investigate applicability of HVO to a production engine. Thus, the aim was to develop a reliable CFD model and analyze its sensitivity to several parameters in order to provide a base point for further research in the future. Following conclusions can be made:

1. The CFD model was developed and validated against two operating points of the engine. It was observed that the model behaved better in terms of the in-cylinder pressure and pollutant emissions prediction at full load conditions (18 bar BMEP) than at part load conditions (9 bar BMEP) for a given engine speed of 2000 rev/min.
2. Sensitivity of the CFD model to the mesh size was done. In terms of computational cost, the fine mesh required 19 days to complete, which is 20 times more than the time required by the coarse mesh. However, it was understood that the mesh size significantly impacts the spray modeling, thus having an effect on the combustion and pollutant formation processes. A fine mesh is required to resolve the spray with sufficient accuracy.
3. Analysis of the CFD model sensitivity to the swirl ratio (SR) showed a limited effect on the spray (for swirl ratios analyzed), while both combustion and pollutant emissions were more impacted at full load conditions. Also, the estimated soot emissions were found out to be more sensitive to SR than the NOx emissions.
4. It was concluded that the swirl ratio sensitivity analysis can be used to fine-tune the CFD model, especially when the intake stroke is not simulated and a fixed SR is applied at IVC. For the developed CFD model, reduction of SR by 25 % helped to achieve more accurate estimations of the in-cylinder pressure and pollutant emissions.
5. Schmidt number sensitivity analysis revealed that this number impacts the air-fuel mixing process by modifying the turbulent mass diffusivity. With decreasing Schmidt number, the premixed phase of combustion is enhanced, resulting in higher peak firing pressure, increased NOx emissions, and reduced emitted quantity of soot.
6. Schmidt number can be used for fine-tuning of the CFD model in order to achieve better matching between experimental and numerical in-cylinder pressure data and predicted pollutant emissions.

For the future work on this activity, it can be suggested to validate the developed CFD model against more operating points. Also, correctness of initial conditions applied in the present work could be improved by making a CFD simulation of the intake process for the given engine. This way the charge motion and turbulence within the cylinder could be better estimated. Finally, HVO can be applied to the developed CFD model. This would enable to perform a deep analysis on the HVO combustion process, how it differs from the conventional diesel combustion, and what is its impact on pollutant emissions. This work would help to understand if modern diesel production engines could be run with HVO without extensive research and development activities.

References

1. Aatola, H., Larmi, M., Sarjovaara, T., Mikkonen, S., “Hydrotreated Vegetable Oil (HVO) as a Renewable Diesel Fuel: Trade-off between NOx, Particulate Emission, and Fuel Consumption of a Heavy Duty Engine”, SAE 2008-01-2500, 2008.
2. Heywood, J. B., *Internal Combustion Engine Fundamentals*, McGraw-Hill, New York, 1988.
3. Lumley, J. L., *Engines. An Introduction*, Cambridge University Press, Cambridge, 1999.
4. Wilson, N. D., Watkins, A. J., Dopson, C., “Asymmetric Valve Strategies and Their Effect on Combustion”, SAE 930821, 1993.
5. Catania, A. E., Spessa, E., “Speed Dependence of Turbulence Properties in a High-Squish Automotive Engine Combustion System”, SAE 960268, 1996.
6. Baumgarten, C., *Mixture Formation in Internal Combustion Engines*, Springer, Berlin, 2006.
7. Lefebvre, A. H., McDonell, V. G., *Atomization and Sprays*, CRC Press, Boca Raton, 2017.
8. Reif, K., *Diesel Engine Management. Systems and Components*, Springer, Berlin, 2014.
9. Dec, J. E., “A Conceptual Model of DI Diesel Combustion Based on Laser-Sheet Imaging”, SAE 970873, 1997.
10. Dec, J. E., Espey, C., “Ignition and Early Soot Formation in a DI Diesel Engine Using Multiple 2-D Imaging Diagnostics”, SAE 950456, 1995.
11. Rao, K. K., Winterbone, D. E., Clough, E., “Influence of Swirl on High Pressure Injection in Hydra Diesel Engine”, SAE 930978, 1993.
12. Benajes, J., Molina, S., Garcia, J. M., Riesco, J. M., “The effect of swirl on combustion and exhaust emissions in heavy-duty diesel engines”, Proceedings of the Institution of Mechanical Engineers Part D Journal of Automobile Engineering 218(10), pp. 1141-1148, 2004.
13. Arcoumanis, C., Cho, S. T., Gavaises, M., Yi, H. S., “Spray and Combustion Development in a Four-Valve Optical DI Diesel Engine”, SAE 2000-01-1183, 2000.
14. Ferziger, J. H., Peric, M., *Computational Methods for Fluid Dynamics*, Springer, Berlin, 2002.
15. Merker, G. P., Schwarz, C., Teichmann, R., *Combustion Engines Development. Mixture Formation, Combustion, Emissions and Simulation*, Springer, Berlin, 2012.
16. Anderson, J. D., *Computational Fluid Dynamics. The Basics with Applications*, McGraw-Hill, New York, 1995.
17. Hoffmann, K. A., Chiang, S. T., *Computational Fluid Dynamics. Volume I*, Engineering Education System, Wichita, 2000.
18. Tannehill, J. C., Anderson, D. A., Pletcher, R. H., *Computational Fluid Mechanics and Heat Transfer*, Taylor & Francis, Washington, 1997.
19. Wesseling, P., *Principles of Computational Fluid Dynamics*, Springer, Berlin, 2001.
20. Moukalled, F., Mangani, L., Darwish, M., *The Finite Volume Method in Computational Fluid Dynamics*, Springer International Publishing, Switzerland, 2016.
21. Wilcox, D. C., *Turbulence Modeling for CFD*, DCW Industries, La Canada, California, 1994.
22. *RNG k-epsilon model*, accessed July 2019, <https://www.cfd-online.com/Wiki/RNG_k-epsilon_model>
23. Yakhot, V., Thangam, S., Gatski, T. B., Orszag, S. A., Speziale, S. G., “Development of turbulence models for shear flows by a double expansion technique”, Physics of Fluids A: Fluid Dynamics 4(7), 1992.
24. *CONVERGE Manual v2.4*, Convergent Science, 2017.
25. *Company Profile*, accessed July 2019, <https://convergecfd.com/about/company-profile>

26. Issa, R. I., "Solution of the Implicitly Discretised Fluid Flow Equations by Operator-Splitting", Journal of Computational Physics 62, pp. 40-65, 1986.
27. *CONVERGE UDF Manual v2.4*, Convergent Science, 2018.
28. Senecal, P. K. et al., "Multi-Dimensional Modeling of Direct-Injection Diesel Spray Liquid Length and Flame Lift-off Length using CFD and Parallel Detailed Chemistry", SAE 2003-01-1043, 2003.
29. Turns, S. R., *An Introduction to Combustion: Concepts and Applications*, McGraw-Hill, New York, 2012.
30. Reitz, R. D., "Modeling Atomization Processes in High-Pressure Vaporizing Sprays", Atomisation and Spray Technology 3, pp. 309-337, 1987.
31. Beale, J. C., Reitz, R. D., "Modeling Spray Atomization with the Kelvin-Helmholtz / Rayleigh-Taylor Hybrid Model", Atomization and Sprays 9(6), pp. 623-650, 1999.
32. Ren, Y., Li, X., "Assessment and validation of liquid breakup models for high-pressure dense diesel sprays", Frontiers in Energy 10(2), pp. 164-175, 2016.
33. Reitz, R. D., Bracco, F. V., "Mechanisms of Breakup of Round Liquid Jets", *Encyclopedia of Fluid Mechanics*, Gulf Publishing Company, Houston, 1986.
34. Kong, S. C., Han, Z., Reitz, R. D., "The Development and Application of a Diesel Ignition and Combustion Model for Multidimensional Engine Simulation", SAE 950278, 1995.
35. Patterson, M. A., Reitz, R. D., "Modeling the Effects of Fuel Spray Characteristics on Diesel Engine Combustion and Emission", SAE 980131, 1998.
36. Schmidt, D. P., Rutland, C. J., "A New Droplet Collision Algorithm", Journal of Computational Physics 164(1), pp. 62-80, 2000.
37. Post, S. L., Abraham, J., "Modeling the Outcome of Drop-Drop Collisions in Diesel Sprays", International Journal of Multiphase Flow 28(6), pp. 997-1019, 2002.
38. Brunt, M. F. J., Platts, K. C., "Calculation of Heat Release in Direct Injection Diesel Engines", SAE 1999-01-0187, 1999.
39. Salvador, F. J., Ruiz, S., Gimeno, J., De la Morena, J., "Estimation of a suitable Schmidt number range in diesel sprays at high injection pressure", International Journal of Thermal Sciences 50, pp. 1790-1798, 2011.
40. Furuhama, S., Suzuki, H., "Temperature Distribution of Piston Rings and Piston in High Speed Diesel Engine", Bulletin of JSME Volume 22, Issue 174, pp. 1788-1795, 1979.
41. Alkidas, A. C., Cole, R. M., "Thermal Loading of the Cylinder Head of a Divided - Chamber Diesel Engine", SAE 831325, 1983.
42. Enomoto, Y., Nagano, H., Hagihara, Y., Koyama, T., "Thermal load in D.I. diesel engine under EGR operation – measurements of steady state temperature of combustion chamber wall surface and intake gas temperature", JSAE Review 18(3), pp. 225-231, 1997.
43. Rutland, C. J., Eckhause, J., Hampson, G., Hessel, R., Kong, S., Patterson, M., Pierpont, D., Sweetland, P., Tow, T., Reitz, R. D., "Toward Predictive Modeling of Diesel Engine Intake Flow, Combustion and Emissions", SAE 941897, 1994.
44. *Turbulence length scale*, accessed September 2019, <https://www.cfd-online.com/Wiki/Turbulent_length_scale>
45. Siebers, D. L., "Scaling Liquid-Phase Fuel Penetration in Diesel Sprays Based on Mixing-Limited Vaporization", SAE 1999-01-0528, 1999
46. Senecal, P. K., Pomraning, E., Richards, K. J., Som, S., "Grid-Convergent Spray Models for Internal Combustion Engine Computational Fluid Dynamics Simulations", Journal of Energy Resources Technology, 136(1), 2013.

47. Mehta, P. S., Tamma, B., “Effect of Swirl and Fuel Injection Characteristics on Premixed Phase of Diesel Combustion”, SAE 980534, 1998.
48. Ogawa, H., Matsui, Y., Kimura, S., Kawashima, J., “Three-Dimensional Computation of the Effects of the Swirl Ratio in Direct-Injection Diesel Engines on NOx and Soot Emissions”, SAE 961125, 1996.
49. De Risi, A., Donateo, T., La Forgia, D., “Effect of Numerical Parameters on the Emissions Trend Predicted by The Kiva 3v Code”, 56° Congresso Nazionale ATI, 2001.
50. Desantes, J. M., Payri, R., Garcia, J. M., Salvador, F. J., “A contribution to the understanding of isothermal diesel spray dynamics”, Fuel 86, pp. 1093–1101, 2007.